

AD-A196 887

DTIC FILE COPY

2

AFOSR-TR- 88 - 0614

A STUDY OF TURBULENCE PRODUCTION USING A NEW PHOTOCHROMIC  
VISUALIZATION TECHNIQUE

by

Approved for public release;  
distribution unlimited.

R. E. Falco and C. C. Chu

AIR FORCE OFFICE OF SCIENTIFIC RESEARCH  
NOTICE OF TRANSMITTAL OF DTIC  
This technical report has been reviewed and is  
approved for release under AFR 190.12.  
Distribution is unlimited.  
MAIL ROOM  
Distribution

Yearly Report

Prepared from work done under  
AFOSR Contract 87-0047  
ORD No. 41305

Report TSL-88-2

DTIC  
SELECTED  
JUN 29 1988  
S H D

Turbulence Structure Laboratory  
Department of Mechanical Engineering  
Michigan State University  
East Lansing, MI 48824

88 017

# REPORT DOCUMENTATION PAGE

1a. REPORT SECURITY CLASSIFICATION Unclassified		1b. RESTRICTIVE MARKINGS	
2a. SECURITY CLASSIFICATION AUTHORITY		3. DISTRIBUTION / AVAILABILITY OF REPORT  Unlimited	
2b. DECLASSIFICATION / DOWNGRADING SCHEDULE			
4. PERFORMING ORGANIZATION REPORT NUMBER(S)		5. MONITORING ORGANIZATION REPORT NUMBER(S) <b>AFOSR-TR- 88-0614</b>	
6a. NAME OF PERFORMING ORGANIZATION Michigan State University	6b. OFFICE SYMBOL (If applicable)	7a. NAME OF MONITORING ORGANIZATION AFOSR	
6c. ADDRESS (City, State, and ZIP Code) East Lansing, MI 48824		7b. ADDRESS (City, State, and ZIP Code) AFOSR/NA Bolling Air Force Base Washington, DC	
8a. NAME OF FUNDING / SPONSORING ORGANIZATION AFOSR / NA	8b. OFFICE SYMBOL (If applicable) NA	9. PROCUREMENT INSTRUMENT IDENTIFICATION NUMBER AFOSR-87-0047	
8c. ADDRESS (City, State, and ZIP Code) Bolling AFB, D.C. 20332		10. SOURCE OF FUNDING NUMBERS PROGRAM ELEMENT NO. 61102F PROJECT NO. 2307 TASK NO. A2 WORK UNIT ACCESSION NO.	
11. TITLE (Include Security Classification) A Study of Turbulence Production Using a New Photochromic Visualization Technique			
12. PERSONAL AUTHOR(S) R. E. Falco & C. C. Chu			
13a. TYPE OF REPORT Yearly ANNUAL	13b. TIME COVERED FROM 10/1/86 TO 10/1/87	14. DATE OF REPORT (Year, Month, Day) 1988 April 28	15. PAGE COUNT 156
16. SUPPLEMENTARY NOTATION			
17. COSATI CODES FIELD GROUP SUB-GROUP		18. SUBJECT TERMS (Continue on reverse if necessary and identify by block number) Turbulence, Boundary Layer, Flow Visualization	
19. ABSTRACT (Continue on reverse if necessary and identify by block number)  The new technique of Laser Induced Photochemical Anemometry (LIPA) has been developed to enable measurement of the evolution of coherent structures involved in the turbulent production process. Results are reported showing the measurement of the streamwise and transverse vorticity component and the strain rate as well as the Reynolds stresses at large numbers of points in a chosen plane. Calibration depends only on a time and a length scale. Comparison of measurements with the exact solution in a Stokes' layer indicates that the technique's accuracy can be predicted by classical error analysis and that it is comparable or better than that achievable with the best single point probe techniques. The results show the relative importance of streaks, pockets and hairpins that are generated in the vortex ring/wall simulation of the turbulence production process.			
20. DISTRIBUTION / AVAILABILITY OF ABSTRACT <input checked="" type="checkbox"/> UNCLASSIFIED/UNLIMITED <input type="checkbox"/> SAME AS RPT. <input type="checkbox"/> DTIC USERS		21. ABSTRACT SECURITY CLASSIFICATION Unclassified	
22a. NAME OF RESPONSIBLE INDIVIDUAL Dr. Jim McMichael		22b. TELEPHONE (Include Area Code) 202-767-4939	22c. OFFICE SYMBOL AFOSR / NA

## LIST OF SYMBOLS

A	Area
C	Circumference
$C_f$	Skin friction coefficient, $(\nu \partial u / \partial y) / (0.5 U_{cl}^2)$
D	Ring bubble diameter (dye marked region)
$D_o$	Inner diameter of the orifice
G	Shear modulus
K	Flow speed/surface wave speed
$R_\theta$	Reynolds number based on momentum thickness
$T_d$	Average time duration of a single event
$T_b$	Average time between events
$U_r$	Velocity of vortex ring in streamwise direction
$U_w$	Velocity of moving wall
$U_{cl}$	Channel centerline velocity
U	Boundary layer free stream velocity
$U_{TE}$	Convection velocity of Typical eddy
$U_c$	Convection velocity of pocket-like depression
V	Total velocity (vector)
W	Transverse length scale of pocket-like depression
Z	Streaks spacing
d	Normal displacement of compliant surface
s	Displacement
t	Time
x,y,z	Spatial coordinates



Accession For	
NTIS GRA&I	<input checked="" type="checkbox"/>
DTIC TAB	<input type="checkbox"/>
Unannounced	<input type="checkbox"/>
Justification	
By _____	
Distribution/	
Availability Codes	
Dist	Avail and/or Special
A-1	

$u, v, w$	Velocity components in x, y, and z-direction
$u_\tau$	Friction velocity, $\downarrow (\nu \partial u / \partial y)$
$\delta$	Stokes' layer thickness
$\omega$	Vorticity
$\tau$	Shear stress
$\gamma$	Shear strain
$\eta$	$y / 2\downarrow \nu t$
$\nu$	Kinematic viscosity
$\theta$	Momentum thickness
$\partial$	Partial derivative
$\Gamma$	Circulation
$\epsilon$	Grid spacing
$\Delta$	Finite interval
$\lambda$	Wavelength
$()^+$	Non-dimensional by wall layer unit, $\nu / u_\tau$
$t^*$	Non-dimensional time, $t(U_w / D_o)$
$\omega^*$	Non-dimensional vorticity, $\omega(\delta / U_w)$
$(\partial u / \partial y)^*$	Non-dimensional $\partial u / \partial y$ , $(\partial u / \partial y)(\delta / U_w)$
$(\partial v / \partial y)^*$	Non-dimensional $\partial v / \partial y$ , $(\partial v / \partial y)(\delta / U_w)$

## 1. INTRODUCTION

Progress this year has centered around further understanding of the turbulence production process model and ways to quantify the various contributions of streaks, hairpins and rings as the wall interaction takes place. Although state of the art hot-wire anemometry such as Foss' vorticity probe (see Foss 1984) and Wallace's nine-wire probe (see Wallace 1986) have made it possible to acquire one point vorticity measurements; these techniques cannot help us to understand rapidly evolving structures since they all must invoke the Taylor's hypothesis. Recently, Lang's (1985) four-spot LDA technique eliminated the intrusive problem, and, in principle, the need for Taylor's hypothesis and an appreciable mean velocity component. However, this technique still yields single, single component vorticity measurements. For many flow problems, it is desirable to obtain simultaneous multi-point measurements. These include understanding the coherent motions in many turbulent and unsteady flows, and the study of mixing in internal combustion engines. Furthermore, quantitative Lagrangian information cannot be obtained by these techniques. Thus, we cannot determine the lifecycle of the turbulent events. It is therefore necessary to develop a technique which is able to provide the flow field information simultaneously over a region to accelerate progress in understanding turbulence. Laser Induced Photochemical Anemometry (LiPA) is considered a most promising technique to meet our need for the fluid dynamics measurement because it is a visual, non-intrusive, and quantitative technique, which is simple to set up and calibrate.

An important part of the current years effort has been to demonstrate LiPA as a powerful tool in turbulent and unsteady flow problems and use it to extend our

understanding of turbulence production and modification in boundary layers. It is hoped that the information gained will lead to a rational basis for boundary layer control. Thus, this study is a combination of both the technical development of LIPA and its application towards understanding the basic physics of the bursting process in turbulent boundary layer flows.

In section 2 the LIPA technique, a non-intrusive technique, will be discussed. This technique was first developed by Hummel and his co-workers (1967). With the advent of high powered excimer lasers, use of highly efficient photochemicals, and new optical designs, we are able to obtain important fluid quantities such as velocity and vorticity over a two-dimensional domain of a complicated fluid flow. In section 3, we further analysis the dynamics of the vortex ring/wall interaction model of the turbulence production process. Based upon the research which has been carried out by Falco (1974, 1977, 1979, 1980 and 1983), Lovett (1982), and Signor (1982), it has been shown that the turbulence production mechanism near a wall is closely related to the formation and evolution of a localized flow module which is created in the wall region of a turbulent boundary layer as the result of the interactions of vortex-ring-like eddies with the viscous sublayer. This model successfully simulates the turbulence production process and provides all visual features observed in the wall region of a turbulent boundary layer such as pocket (Falco 1979), a pair of low speed streaks (Runstadler et al. 1963, Offen and Kline 1975, Oldaker and Tiederman 1977, Smith 1978, Falco 1980) with the spacing about 100 wall layer units, and hairpin liftup (Falco 1982, Acarlar and Smith 1984). It also reveals the vortical motions associated with the streaky structure. To quantify the fluid quantities in such a complicated three-dimensional unsteady flow, we apply the LIPA technique. We make use of LIPA measurements of vorticity and velocity in a Stokes' layer in order to demonstrate the accuracy of the LIPA technique.

The ability of this technique is revealed by the measurements of vortex ring flows. Measurements of the vortex ring/moving wall interaction in section 4 reveal many details of the vortex ring/moving wall interaction model and shed new light on how production takes place in the bursting process in the boundary layer flows. The first measurements of streamwise vorticity and the evolution of streamwise vorticity and Reynolds stress associated with streaks, hairpins and pockets are presented. These results shows that the streamwise vorticity and Reynolds stress component in cross-stream planes associated with the pocket vortices completely dominates the interaction. Their values in the hairpins are much lower. The streamwise vorticity associated with the stable long streamwise vortices is negligible.

## **2. LASER INDUCED PHOTOCHEMICAL ANEMOMETRY (LIPA)**

### **2.1. Introduction**

Hummel and his co-workers (1967) first exploited the phenomena of photochromism (Brown 1971). Photochromism is attributed to atoms or molecules which are stable or metastable in two states and which possess different molecular or electronic configurations; i.e., having distinguishably different absorption spectra. Certain external excitations can cause the atoms to shift between the two states. Discovering this fact, Popovich and Hummel (1967) and Seely et al. (1975) used a single line of uv radiation to excite an organic liquid in which a certain amount of photochromic chemical had been dissolved. They were able to follow the discolored time line and measure one component of velocity in flows with one predominant direction of motion. Today, with the advent of highly powered uv lasers, advanced optical designs and new chemicals, we are able to extend this technique to more complicated flows.

### 2.1.1. Photochromic chemical, light source and working fluid

The chemical used in this study was Kodak 1,3-Trimethyl-8-nitrospiro[2-H-1-benzopyran-2,2'-indoline]. Fig. 2.1 shows the associated absorption and emission spectrum of this chemical. We excited it at 351nm using pulses of 20ns duration produced by a Tachisto Excimer laser running on XeF with approximately 100 mJ output and repetition rate being adjustable from 0.1 to 100 Hz. The laser beam was 3 x 20 mm at the exit and had a divergence of 6 mrad half angle. The chemical was dissolved in the working fluid, kerosene; we found that when the chemical was excited, it reflected blue light for a certain period of time which depended on the power of the excitation and the concentration of the chemical. Generally speaking, higher laser intensity results in a longer trace length and a darker trace color; higher chemical concentration results in a shorter trace length, a longer trace lifetime and also a darker trace color. For each experiment we controlled the concentration of the chemical to let the fluid be tagged long enough to move appreciably, so that we could obtain the required information. Usually, the concentration of the chemical ranged between 5 to 15 ppm. Since the working fluid had a low electrical conductivity, 5 ppm of anti-static agent, Shell-Sol 71, was added to increase the conductivity of the kerosene to avoid building up an electrostatic charge. The addition of the anti-static agent also increased the polarity of the testing fluid, and thus the equilibrium between the two molecular states was shifted toward the colored side. Therefore, the lifetime of the photochromic traces increased with the concentration of the anti-static agent. In principle, for the velocities of our experiments, we needed to follow the photochromic lines for only a fraction of a second to obtain the required information.

### 2.2. Technical details

In practice, we need only to follow one visual photochromic time line to obtain



one velocity component in the flows with one predominant flow direction, and also to obtain the velocity gradient within the viscous sublayer of a turbulent boundary. However, to measure two components of the velocity in a flow using the visualization, we must tag and follow specific fluid particles. The simplest way to do this is to have two photochromic lines intersect. That intersection defines a point in the flow which we can follow. To measure a spatial gradient, we must simultaneously mark two points in the flow. In addition, we need several points and must use interpolation to measure a spatial gradient in a prescribed direction. Thus, creation of a grid of marked intersecting fluid lines would allow us to simultaneously measure velocities and gradients in the plane on which the grid is generated. Furthermore, by integrating the velocity component along each grid box we are able to obtain instantaneous circulation and vorticity distribution in the plane of the recording media. Accordingly, we catalog the applications into two groups: single tracer technique and grid tracing technique. All the technical details and the applications of these techniques are given below.

### **2.2.1. Optical setup**

#### *2.2.1.1. Single tracer technique*

Liang (1984) applied this technique to study the spatial growth of a Stokes' layer. For some applications, we need only one photochromic line to define the velocity gradient  $\partial u / \partial y$  on the wall in a turbulent boundary layer and the velocity profiles in the unsteady flows with one predominant flow direction. However, due to the rectangular shaped cross-section of the laser beam, it depends on the local flow conditions and the orientation of the laser beam to get the best quality of the photochromic time line. For example, if we would like to obtain the velocity distribution of a two-dimensional boundary layer, the photochromic time line shown in Fig. 2.2 (a) will, of course, result in a higher resolution image than that shown in Fig. 2.2 (b). In other cases, such as

measuring the mean velocity distribution in the spanwise direction of the same flow field, the orientation of the laser beam shown in Fig. 2.3 (a) will result in a better image than that shown in Fig. 2.3 (b), even though the photochromic time line is less dense in color; however, its reduced sensitivity to the local shear force of the flow will keep the photochromic time line itself from smearing.

Fig. 2.4 shows the experimental configuration for one of the laser beam orientations. The convex lens was a fused silica lens, 38.2 mm in diameter, 500 mm in focal length, and with a transmission higher than 90% at 351 nm wavelength. The lens thinned the laser beam from 20 x 7 mm down to 0.056 x 0.160 mm at the focal point. Fig. 2.5 shows the divergence characters of the laser beam after a F-500mm convex lens.

#### *2.2.1.2. Grid tracing technique*

To enable us to measure important fluid quantities over a two-dimensional domain of a fluid flow, we have generalized the technique to uniquely tag specific points in the flow on a specific grid which can be used to obtain two velocity components and the spatial gradients of these components at a large number of points in a flow field.

We sought a method of dividing a laser beam into 'n' beams where 'n' would be 10, using a static device. In doing so, we sought to lose as little light as possible. Thus, a special divider was designed by Prof. Falco, which appears as an oversized blazed reflecting grating; the step size 'a' is approximately 2 mm. The incident laser beam was directed at a shallow angle (15 degrees) to the plane of the grating. Because the facets are so much larger than a wavelength of light, we expected to primarily see specular reflection. The separation of the specularly reflected portions of the beam was

determined by the difference of the angle of incidence and the blaze angle, and the grating step width and spacing as shown in Fig. 2.6. A photo of the actual beam divider is shown in Fig. 2.7. It was fabricated by individually fixing aluminum coated mirrors to a machined base. Apart from diffraction effects, no incident laser energy would be lost. As expected, diffraction effects were exhibited in a far-field case, that is, Fraunhofer diffraction (see Hecht and Zajac). A photo of the output of the beam divider using a Helium Neon laser is shown in Fig. 2.8. We can see the specularly reflected beams and the superimposed diffraction pattern. When experiments were performed with the Excimer laser at 351 nm in the near-field, the diffraction pattern was not observed (Fresnel diffraction). For all experiments using the photochromic grid tracing technique, we have to make sure to locate the test area away from the effect of far-field diffraction.

Fig. 2.9 presents a schematic representation of the optical setup for making a grid in Fig. 2.10 (a). The beam splitter is made by Newport Co. and designed for 351 nm wavelength. Again, the focal length of the convex lens is 500 mm. Note that the orientation of the laser beam is also based upon the same principle mentioned in the previous section. The arrangement of the optical set for different flow measurements will be discussed in Chapter 4.

## **2.3. Algorithms to obtain fluid dynamic quantities**

### **2.3.1. Single tracer technique**

The technique to measure the velocity component by a single incident beam path is to measure the displacement between two tracers along the mean flow direction and to divide this distance by the time interval between the two tracers. (The time interval is the reciprocal value of the laser pulsing rate.) Fig. 2.11 shows one example of

wall shear stress measurement in the turbulent channel flow where  $t_1$  and  $t_2$  represent two instantaneous photochromic tracers in the near wall region. We choose  $y_0$  within the sublayer and measure the distance between  $t_1$  and  $t_2$  which is  $\Delta s$ ; we know the time interval  $\Delta t$  between two tracers, then the velocity  $V$  will be  $\Delta s/\Delta t$  at  $y_0$ ; furthermore, the velocity gradient at the wall can be approximated as  $V/y_0$ . This procedure can be used to calculate the displacement, velocity, and the velocity gradient.

### 2.3.2. Grid tracing technique

The two photos in Fig. 2.10 show the grid generated by the optical configuration shown in Fig. 2.9, which are 0.4 seconds apart, taken by a still camera with a motor drive. The mesh size is the order of 1 mm. From the distortion of the grid in Fig. 2.10 (b) in comparison to the one in Fig. 2.10 (a), (one laser pulse, two photos with  $\Delta t$  apart) we can calculate all the kinematic quantities of the flow in the plane of the film. Note that, in practice, we would not use a second image which has distorted as much as Fig. 2.10 (b); this is only used to illustrate the procedure.

For convenience, we choose any one 'grid box' in Fig. 2.10 (a) which, if the mesh size is small enough, can be thought as of as a textbook 'fluid particle' in a flow at time  $t = 0$ . This fluid particle is shown using solid lines in Fig. 2.12 (a). As this particle moves with the flow, it may undergo several motions such as translation, rotation, and deformation. The dashed lines in Fig. 2.12 (a) show the same fluid particle after a short time interval,  $\Delta t$ . Because we know the history of this specific fluid particle, we can compute the velocity of each corner by taking the time derivative of displacement  $\Delta s$  associated with each point, that is,  $\Delta s/\Delta t$ . The deduction procedures are shown in Fig. 2.12 (b). Note that  $V$  is designated as the velocity at point 1 which is then positioned at the midpoint between point 1' and point 1". Fig. 2.13 shows the velocity vectors deduced from Fig. 2.13. Actually, a fluid particle moving in a general three-dimensional flow

field may have motions about all three coordinate axes; however, we limit the discussion to the projection of this motion onto the plane of the photos which is parallel to the initial plane of the grid.

To obtain velocity gradients, vorticity, and strain rates from the velocities, we must differentiate across the distance of a grid box. Thus, for a given flow, the grid mesh must be small enough to resolve the smallest scales of motion.

An alternative method can be used if we are interested in the vorticity. Using the definition of the circulation  $\Gamma$ ,

$$\Gamma = \int_C \mathbf{V} \cdot d\mathbf{s} \quad (1)$$

and Gauss' theorem to relate the surface integral to an area integral,

$$\Gamma = \iint_A \boldsymbol{\omega} \cdot d\mathbf{A} \quad (2)$$

we can obtain the vorticity component normal to the film plane,  $\omega_z$ , from a grid box of arbitrary shape, with circumference  $C$  and area  $A$ . The velocity component  $\mathbf{V} \cdot d\mathbf{s}$  in Eq.(1) is estimated by forming the average of the corner velocity components (see Fig. 2.13). The dividing of  $\Gamma$  in eq.(2) by the area of the grid box results in the average vorticity at the centroid of this fluid particle. This approach has the advantages of avoiding a second differentiation (i.e. the differentiation of  $\mathbf{V}$  with respect to  $x$  or  $y$ ) of the experimental data.

Thus, by following the distortions of a single grid box we can obtain the velocities, circulation, vorticity and even the Reynolds stress and strain rates, if desired, over that small area. By doing this for the other grid mesh points, we can obtain the important fluid dynamic quantities at many locations over a two-dimensional field in a fluid flow simultaneously.

#### 2.4. Calibration and error analysis

The calibration of this technique depends only on a time and a length scale. In principle, we need only to have a known length scale on the film and the time interval between two films, so we are able to calculate displacement, velocity, and etc.

As far as the designated accuracy of the grid tracing technique is concerned, let us consider the grid box in Fig. 2.10 (a). Let us assume that the grid mesh is spaced  $\epsilon$  and that a worse case line movement between images is  $1/2$  the mesh width. After time  $\Delta t$ , standard analysis (see Taylor 1972 as well as Falco and Chu 1987) shows that the uncertainty in estimating the vorticity  $z$  is

$$\delta\omega_z = (1/\Delta t)(\delta\epsilon/\epsilon)$$

to first order in  $\epsilon$ . The details of this analysis are shown in Appendix A. As an example of the designed accuracy of our experiments, if we produce  $100\ \mu\text{m}$  lines on a grid of mesh of  $1\ \text{mm}$ , and our error in reading the center of the lines is  $10\%$ , we obtain  $\delta\epsilon/\epsilon = 0.01$ . For  $\Delta t = 0.01\ \text{sec}$ , the uncertainty in the measurement is  $1/\text{sec}$ . This is better than has been possible with a hot-wire probe, and is comparable with the most sophisticated four-spot laser doppler measurements (see Lang 1985).

## 2.5. Summary and comments

1. A non-intrusive, visual, and quantitative technique has been developed, by which we are able to measure the instantaneous fluid dynamic quantities such as velocity, vorticity, and circulation over a two-dimensional domain of a fluid flow.

2. The vorticity obtained by the photochromic grid tracing technique is the average vorticity of a small area instead of the true vorticity at one point because vorticity is a point function. All the measured vorticity mentioned in section 4 will represent the average vorticity of each small grid box. The direction of the average

vorticity is normal to the image plane.

3. The calibration depends only on a time and a length scale.

4. Analytically, the designed accuracy is better than that with hot-wire probes, and is comparable with the most sophisticated four-spot LDA measurement.

5. The algorithms of obtaining fluid dynamic quantities involves the linear approximation. Thus, the distortion of the photochromic time line cannot be too much; usually we keep the edges of each grid box as straight as possible.

6. The ability and accuracy of this technique and the possible human errors will be tested and discussed in following sections through the all applications in this study.

7. Further discussion and comments and improvements will be in section 4 & 5.

### **3. NEW UNDERSTANDING OF THE INTERACTION ASSOCIATED WITH TURBULENCE PRODUCTION: A VORTEX RING/MOVING WALL INTERACTION MODEL OF THE TURBULENCE PRODUCTION MECHANISM NEAR A WALL**

#### **3.1. Introduction**

There is a need to construct both experimental and numerical simulations of the turbulence production process near walls, because of the difficulty of isolating mechanisms when experiments are conducted in the boundary flows. A good simulation must embody the essential features of the production process. Several investigators (Kline et al. 1967, Corino and Brodkey 1969, Offen and Kline 1975, Falco 1978, 1979, 1980, Smith 1978) have presented some possible mechanisms which are responsible for the production process in the near wall region of boundary layer flows. In this section we present a moderately extensive review of the important structural features associated with the wall region events as well as the new boundary layer observations observed in Turbulence Structure Laboratory, Michigan State University (Falco, Lovett, and Signor), that helps complete the picture of structural feature interactions. Then we present the vortex ring/moving wall simulation experiments that model all of the important properties.

##### **3.1.1. A review of the important structural features associated with the wall region events in boundary layer flows**

Turbulent boundary layer structure that should be modeled includes the long streaks (Runstadler et al. 1963), the pockets (Falco 1980a, 1980b), the hairpins (Falco 1982, Acarlar and Smith 1984), the Typical eddies (Falco 1977, 1983), and coherent regions of streamwise vorticity and/or streamwise vortices. Basically, these structural



features have been shown to be associated with the production process, but the formation of the structures and the interactions are not completely understood. A number of investigators have studied the formation of low speed streaks. Oldaker and Tiederman (1977) observed that a pair of low speed streaks formed as a result of the response to what appeared to be a sequence of local high speed outer region eddies interacting with the wall and aligned along a streamwise direction. The path left by the outer region disturbances clearly formed a high speed streak. Falco (1980a) observed the formation of low speed streaks in pairs by a similar mechanism. Although low speed streaks are often observed to exist singly, care must be taken when interpreting low speed streak formation, because once formed the low speed streaks can persist for very long times (Smith and Metzler 1983), and the undisturbed passive dye marked region will simply convect into the observation zone.

Since the mid fifties, it has been suggested that long counter rotating streamwise vortices exist in the wall region and that pairs of these vortices produce a gathering of wall layer dye between them that we see as the low speed streaks. A high speed streak would be the result of high speed fluid being induced towards the wall between a pair of these streamwise vortices rotating the other way. A number of authors have suggested causes for these streamwise vortices. Currently, the most popular suggestion is that they are the 'legs' of hairpin vortices that are also observed in the wall region. However, as Acarlar and Smith (1984) have pointed out, it is very hard to understand how the hairpin legs could extend upstream as far as would be necessary to produce streaks of length  $x^+ = O(1000)$ . Thus, there is still no experimental evidence supporting the various rational physical hypotheses describing the formation of long streaks.

Another feature of the wall region structure is the frequent rearrangement of

marker that moves it away from a local region, leaving a scoured 'pocket' of low marker concentration. Fig. 3.1 shows two pockets as seen in a layer of smoke marked sublayer fluid. Pockets are footprints of outer region motions that interact with the wall. Falco (1980a) showed that they start out as a movement of wall layer fluid away from a location as a high speed outer region eddy (a typical eddy, discussed below) nears the wall. The interaction results in the footprint opening up into a developed pocket shape. Fluid is seen to lift-up from the downstream end of the pocket, and take on the characteristics of a hairpin vortex (Falco 1982).

Vortex lines are constantly being bent in turbulent boundary layers. Although flow visualization of a passive contaminant cannot be used to observe vorticity directly, dye marked features in the wall region that appear to be hairpin vortices have been observed by Falco (1982) and Smith et al. (1983). We have observed hairpins appearing to form over individual streaks. The streak is seen to become lumpy, and one of the lumps grows and a hairpin emerges from it. Acarlar and Smith (1984) have also observed hairpins growing over simulated streaks, and, it appears, in a turbulent boundary layer.

The microscale coherent motions observed across a turbulent boundary layer, which are similar to laminar vortex rings embedded in a shear flow, are called Typical eddies. They have been studied by Falco (1974, 1977, 1982, 1983), who showed that they contribute significantly to the Reynolds stress in the outer part of the boundary layer, and that they are the excitation eddies that create the pockets. Experiments using two mutually orthogonal sheets of laser light enabled Falco (1980b) to determine, as far as the smoke marking allows, that the coherent feature was a ring, as opposed to a portion of a hairpin vortex, as suggested by Head and Bandyopadhyay (1981).

Both types of hairpin creation mechanisms described above can produce

hairpins that can pinch-off and form new vortex rings. Falco (1983) showed visual evidence of a hairpin lifting from the downstream end of a pocket, contorting and pinching off to form a new vortex ring-like typical eddy. This pinch-off mechanism has also been clearly shown to occur in the calculations of Moin et al. (1986) mentioned above.

Many investigators have noted the presence of streamwise vortices in the wall region. Almost without exception, the vortices have been of short extent (Praturi and Brodkey 1978, Falco 1980b, Smith 1982). A number of investigators have suggested that streamwise vortices of much greater extent exist in the wall region essentially laying just above the wall in pairs, which are responsible for the creation of both low and high speed streaks. This evidence is of a statistical nature, usually from correlation measurements. However, no one has ever observed them, and recent calculations of turbulent channel flow using the full Navier-Stokes equations (Kim 1986) have shown that the eddies which have streamwise vorticity are not elongated in the streamwise direction.

### **3.1.2. New boundary layer observations in the Turbulence Structure Laboratory, Michigan State University**

The major discovery is that as a typical eddy convects over the wall, it causes an interaction that results in the formation of a pair of long streaks. If the typical eddy is convecting towards the wall, when it gets close enough, it will create a pocket, and have one of four types of interactions defined below. The creation of the long streaks occurs even when the typical eddies are quite distant from the wall, well into the log region.

Observations mentioned above have indicated that hairpin vortices can form as a result of pocket evolution and as a result of lumping instability of existing low speed streaks. They also found that there were occurrences where neither of these

mechanisms appeared to be the cause. They also identified another mechanism that can result in the formation of hairpin vortices. When a typical eddy is moving away from the wall at a shallow angle and when it is moving relatively slowly, say  $U_c/U < 0.4$ , it will create a pair of long very stable streaks that trail behind a hairpin vortex that lifts up slowly. The eddy can be as far from the wall as indicated above, and thus, will convect appreciably downstream before the hairpin will be noticed. It may convect out of the field of view, leaving the observer with the impression that the formation of the hairpin did not involve the coherent motion.

Thus, only one coherent motion, interacting with the wall, is necessary to create both the long streaks and the pockets; since the remaining structures found in the wall region are related to these two structures. The visual results suggested that the typical eddy be responsible for the onset of the turbulent production process.

### **3.2. Vortex Ring/Moving Wall Interaction Model**

#### **3.2.1. Vortex ring/moving wall simulation of the turbulence production process**

Accordingly, we can simulate the interaction of a typical eddy with the wall region of a turbulent boundary layer by creating a vortex ring and having it convect towards or away from a moving wall. Fig. 3.2 shows the basic idea behind the simulation. The vortex ring can be aimed at or away from the wall at shallow angles. Both the wall and the ring move in the same direction. The Reynolds numbers based upon the initial ring velocity and diameter of the dyed ring bubble,  $D$ , ranges between 600 and 2000. When created away from walls, these rings remain stable to azimuthal instabilities over durations longer than those used in the interaction experiments. By performing a Galilean transformation on the simulation, we recover the essential aspects of the typical eddy wall region interaction in a turbulent boundary layer flow.

For convenience, we have used an impulsively started moving belt. It has the advantages of being an exact solution of the Navier-Stokes equations (Stokes' first problem), and therefore is well defined. Furthermore, the velocity profile is approximately linear in the wall region which is similar to the mean velocity profile of the viscous sublayer of a turbulent boundary layer. It is relatively easy to match the friction velocity in these simulations with those found in low Reynolds number turbulent boundary layers.

### **3.2.2. Experimental details**

#### **3.2.2.1. *Experimental apparatus***

Experimental simulations were performed in a water tank which is 40.5 cm deep by 32.4 cm wide by 243.8 cm long. Fig. 3.3 shows the side view and end view of the experimental apparatus which includes a vortex ring generating device, a moving belt and driving arrangement, a synchronizing timer, and visualization recording devices.

##### **3.2.2.1.1 *Vortex ring generating device***

The vortex ring generating device includes a constant head reservoir from which fluid, which could be dyed, passes through a solenoid valve whose opening time could be varied, and an orifice of prescribed size (see Fig. 3.3 items 1,2,3). The constant head reservoir (item No. 1) is filled with a mixture of 10 ppm Fluorescent Sodium Salt Sigma No. F-6377, green dye and water solution. As the solenoid valve (No. 2) opens, a slug of dyed fluid is released from the orifice (3) by the pressure head, and rolls up into a vortex ring. Three different inner diameters of the orifice have been used; 2.54 cm, 1.27 cm, and 0.95 cm. The size and speed of the vortex ring generated depends upon both the height of the dye reservoir and the opening duration time of the solenoid valve for a fixed orifice. The details have been presented in Liang (1984).

#### 3.2.2.1.2 Moving belt and driving device

The wall upon which the vortex ring interacted is a moving belt (4) made of transparent plastic which has a smooth surface. Two ends of the belt are joined together to form a loop, which circulates around two rollers (5) as shown in Fig. 3.3. The width of the belt is 17.8 cm; and the distance between the two rollers is 152.4 cm. The test section is at 76.2cm downstream from one of the rollers, giving us a Stokes' layer for this distance (if the belt is run longer in time, the leading edge effects begin to enter into the problem). This width/length ratio is sufficient to prevent the disturbances generated in the corners from reaching the center of the belt at the test section. Therefore, the wall layer flow on the moving belt could be considered one-dimensional. One of the rollers is driven by a 1/4 HP DC motor (6). The speed of the belt is adjustable within the range of 2.5 cm/sec. to 22.9 cm/sec. The belt reaches a constant speed very soon (within a second) after power is turned on. This short acceleration period allows us to consider the belt to be impulsively started. As the belt moves, a Stokes' layer builds up on the belt. A mixture of red food coloring and water is used to mark the wall layer for visualization. The belt is covered with dye before each run during a 'dye run' using a dye injector near the leading roller of the belt, shown in Fig. 3.3 (7). The fluid is allowed to come to complete rest before each 'data run'.

#### 3.2.2.1.3 Control system

The opening duration time of the solenoid valve, and the time delay between the onset of the belt movement and release of the vortex ring are controlled by a 115 VAC/60 Hz timer designed in the laboratory. Since the thickness of the Stokes' layer,  $\delta$ , is a function of the square root of the belt run time, that is,  $\delta = 4.0 \sqrt{vt}$ , by carefully adjusting the time delay, we can adjust  $\delta/D$  as desired.

#### 3.2.2.2. Visualization and recording

#### *3.2.2.2.1 Two-view visualization*

The primary visual data consisted of simultaneous plan and side view time resolved images which were collected using a standard video camera, a VCR, and a monitor, and are shown in the end view of Fig. 3.3. The side view was often illuminated by a laser sheet emitted from an 8 W Coherent CR-8 Supergraphite Argon Ion Laser. The visual data were analyzed on a high resolution monitor with a superimposed calibrated scale, using the slow motion capabilities of the recorder.

A 35mm Photo-Sonic movie camera and a 16mm Redlake high speed movie camera were also used to record high resolution images of the interactions on Kodak ASA 400 color negative film and Kodak Ektachrome 7250 film respectively. The data acquisition system is the same as that shown in Fig. 3.3

#### *3.2.2.2.2 Three-view visualization*

A simultaneous three-view data acquisition system was designed in order to resolve the vortical structure associated with the vortex ring/moving wall interaction in the plane which is perpendicular to the mean flow direction Fig. 3.4 shows the scheme of the three-view visualization system; note that only the end view was illuminated by the laser sheet. The image of the laser illuminated end view was sent to the top view collecting mirror through a front coating flat mirror. This is shown in both views of the set-up in Fig. 3.4.

### **3.3. Results of vortex ring/moving wall interactions based on two-view flow visualizations**

We will describe the model in terms of the velocity ratios and spatial relationships of the simulation. Later in the discussion, we will invoke the Galilean transformation to relate the findings to the turbulent boundary layer case.

### 3.3.1. Evolutions of the model

#### 3.3.1.1. Fast rings ( $U_r/U_w > 0.45$ ) moving towards the wall with a shallow angle ( 3, 6, and 9 degree)

Interactions which result from these rings have been described by Liang et al. (1983). They result in the formation of a pocket, and varying degrees of lift-up of wall layer fluid. The interactions have been divided into four types. Fig. 3.5 shows sketches of the four types of interactions. Type I results in a minor rearrangement of the wall layer fluid; followed by the ring moving away from the wall essentially undisturbed. Type II (same as described for boundary layer interactions) results in a well defined lift-up of wall layer fluid, which takes on a hairpin configuration. This fluid does not get ingested into the ring, and the ring moves away from the wall as a perturbed but stable ring. The hairpin has been observed to pinch-off or just move back down towards the wall and lose its identity. Type III results in a lifted hairpin of wall layer fluid which gets ingested into the ring, resulting in a chaotic breakdown of both the lifted hairpin and the vortex ring, as the vortex ring is moving away from the wall. Type IV also initiates a hairpin vortex, but in this case the hairpin vortex is ingested into the ring on a much shorter timescale, and the ring and lifted wall layer fluid both breakdown while the ring is very close to the wall.

Liang et al. used vortex rings with  $D^+ > 250$  and  $\delta^+$  between 20 and 50, and they observed only the above four types of interactions. Current experiments indicate that if  $D^+ < 150$  and  $\delta^+$  is between 20 and 50, we can also obtain the four types of interactions noted above, but, in addition, we found that long streaks also formed. In these cases, a hairpin grew out of the open end of the pocket, its legs stretched and a pair of streamwise streaks formed along the hairpin legs (see Fig. 3.6). The streaks grew to several hundred wall units. This observation is in contrast to the suggestions of a



number of investigators that a lifted hairpin vortex would induce a single streak to form between its legs.

*3.3.1.2. Slow rings ( $U_r/U_w < 0.35$ ) moving towards the wall at a shallow angle (3, 6, and 9 degree)*

These initial conditions result in a pair of long low speed streaks,  $x^+ = O(1000)$ , a pocket, and hairpins which induce themselves and portions of the streaks to lift-up. Fig. 3.7 shows six photos of this happening prior to the onset of a Type III interaction. We can see the formation of the pair of low speed streaks, followed by the formation of the pocket, and the associated hairpin lift-up, then partial ingestion of the pocket hairpin. The ring later breaks up. The streaks that form under these conditions become wavy and slowly breakdown resulting in additional lift-up and transport. Hairpins have been observed to form over these streaks (see Fig. 3.8). The initial conditions are two-dimensional. The moving belt is started from rest, so that the layer approximates a Stokes' layer. These streaks have obviously not formed as the result of the pre-existence of streamwise vortices, but spanwise vorticity has been distorted to give a streamwise component, and it is clear from the Navier Stokes equations that new streamwise vorticity has also been generated at the wall.

*3.3.1.3. Fast rings ( $U_r/U_w > 0.45$ ) moving away from the wall at a shallow angle (less than 3 degrees)*

These initial conditions result in a hairpin vortex which is linked to the distributed streamwise vorticity that has formed a pair of long, very stable, low speed streaks. A pocket is not observed. The evolution of the hairpin in this case has been observed to lead to the pinch-off of this hairpin, forming a vortex ring, and another hairpin. Fig. 3.9 shows four photos of the evolution leading to the creation of a new vortex ring. The long stable streaks which form come closer and closer together,

indicating that the streamwise vorticity which caused them, and which is of opposite sign, is being stretched and brought very close together. Diffusion is accelerated, and the vorticity is redistributed into a vortex ring and a hairpin loop. Fig. 3.10 shows long stable streaks and a long stretched hairpin which does not pinch-off over the distance available due to size limitations of the experimental facility--more than 2500 wall layer units. There are two initial conditions that may cause this kind of long stretched streamwise vorticity to evolve into a hairpin: 1)  $\delta/D$  is very small; 2) the ring is far away from the wall. Further study concerning the effects of ring to wall distance is needed.

#### *3.3.1.4. Far-field effect (fast ring, $U_r/U_w > 0.6$ , moves away from the wall at a shallow angle)*

The far field effect could happen even though the edge of the lower lobe of the vortex ring is around  $120 y^+$  above the wall. A long stretched hairpin was observed to form which had the same shape as that shown in Fig. 3.10, however, the spacing between the two legs became narrower as the distance between the ring and the wall became larger.

#### *3.3.1.5. Slow rings ( $U_r/U_w < 0.45$ ) moving away from the wall at a shallow angle (less than 3 degree)*

These initial conditions result in a hairpin from which a pair of long stable low speed streaks emerge. A pocket is also not observed. The phenomenon of hairpin pinch-off, for this case, appears to depend upon  $\delta/D$ . If  $\delta/D < 0.15$  we get pinch-off, but only a part of the fluid involved in the hairpin is observed to pinch-off and form the ring. If  $\delta/D$  is greater, and the ring moves away from the wall without ingesting any wall layer fluid (Type I or II), the lifted hairpin appears to do very little. Fig. 3.11 shows four photos of the evolution for  $\delta/D > 0.15$ . In this case a pocket does not form, and it appears that the hairpin has been generated by the initial vortex ring/wall interaction,

and that a pair of streamwise vortices--which could be called its legs--trail behind, creating the streak pair. Pinch-off does not occur. Fig. 3.12 shows four photos of the interaction for  $\delta/D < 0.15$ . In this case pinch-off of a portion of the lifted hairpin does occur creating a new small vortex ring.

#### 3.3.1.6. *Summary of interactions*

A summary of the vortex ring/wall interactions which result in streak formation and evolution is shown as a function of the parameters  $U_r/U_w$ ,  $\delta/D$ , and ring angle in Fig. 3.13 and 3.14. Fig. 3.13 shows the dependence of the formations and evolutions of streaks on  $\delta/D$  and  $U_r/U_w$  for  $D^+ > 250$  and a 3 degree incidence angle. The indicated boundaries are between different evolutions and are approximate; additional data are necessary to precisely locate their positions. The available information suggests that the streak development is essentially not dependent upon  $\delta/D$ . Furthermore, the long streaks are only observed to form for speed ratios less than approximately 0.35. Fig. 3.14 shows the dependence of the formations and evolutions of streaks on  $\delta/D$  and  $U_r/U_w$  for rings moving away from the wall at 2.5 degrees.  $\delta/D$  now plays a much more important role, and long streaks are generated over the entire speed ratio range studied.

### 3.3.2. **Scaling associated with the vortex ring/moving wall interactions**

From our perspective of a turbulence production model, the streak spacing, streak length and wavelength of the streak instability are quantities of interest.

#### 3.3.2.1. *Streak spacing*

Fig. 3.15 shows the dependence of the non-dimensional streak spacing on the size of the non-dimensional vortex ring, for an incidence angle of 3 degrees and  $U_r/U_w$

$= 0.31$ . The thickness of the wall layer (in wall units) is shown next to each data point. The streak spacing,  $Z^+$ , is within 10% of the ring diameter for wall layer thicknesses between 20 and 50 wall units. Results shows that decreasing  $U_r/U_w$  will decrease the average streak spacing relative to the ring size for fixed incidence angles. Furthermore, increasing the incidence angle of the vortex ring will increase the average streak spacing for a given ring size and speed ratio. Fig. 3.16 shows the dependence of the streak spacing on the speed ratio and angle.

### 3.3.2.2. *Streak length*

Measurements show that streak lengths greater than  $x^+ = 500$  were obtained for many of the interactions in ranges where the streaks are stable ( for rings with  $D^+ = 100$ , streaks as long as  $x^+ = 1000$  were found ).

### 3.3.2.3. *Wavelength associated with wavy streak instability*

Fig. 3.17 shows the non-dimensionalized streamwise wavelength that sets in as a function of  $\delta^+$  for different  $U_r/U_w$ . The wavelength is the same order as the ring diameter. It decreases as the ring/wall speed ratio.

## 3.3.3. **Stability considerations**

### 3.3.3.1. *Vortex ring stability*

Some additional data has been obtained, which confirms and extends the results of Liang (1984), showing that the boundary between stable ring wall interactions (Types I and II), and unstable interactions (Types III and IV) depends upon  $\delta/D$ . Fig. 3.18 shows a stability map of the interactions for 3 degree rings. We can see that for low ring/wall speed ratios, the ring stability depends primarily upon the relative thickness of the wall layer and the size of the ring; for thicker wall layers or smaller rings, the

interactions are more stable. Furthermore, the shallower the incidence angle the more stable the interaction.

#### 3.3.3.2. *Stability of the streaks*

Fig. 3.19 shows the dependence of the time onto instability (i.e. the time from the formation of the streaks to the first observation of the wavy instability) of the streaks which exhibited wavy instability on the wall layer thickness (both quantities are non-dimensionalized by wall layer variables) for 3 degree incidence rings. We can see that for each convection velocity ratio, there is a value of  $\delta^+$  above which the time to instability becomes much longer.

#### 3.3.3.3. *Comparison between ring and streak stability*

Both the rings and the streaks are more stable when the wall layer is thicker. Fig. 3.18 shows a comparison of the stability boundaries of a three degree ring moving towards the wall, with the stability boundary of streaks formed by those same rings. The streak stability boundary has generally the same shape; stable rings will, in general, correspond to stable streaks, except for a small range of  $\delta/D$ . The ring stability curves and the streak stability boundary curves for different size rings collapse when plotted this way.

The streak formation boundaries in this figure represent the boundaries between conditions that will enable a pair of long streaks to form. For  $\delta/D$  below the boundaries, we have a very unstable situation in which the fluid in the region around the eddy seems to rearrange itself into the beginnings of a streak, but the streak pair is not stable, and immediately breaks up. For  $\delta/D$  values above the boundaries, a pair of long streamwise streaks form. However, once formed, the streaks are susceptible to breakdown by the wavy or lumpy instabilities noted above, where the time to instability

is a function of angle, convection velocity, and the instantaneous wall layer thickness (for example, see Fig. 3.19).

### **3.4. Results of the vortex ring/moving wall interactions based on three-view visualization**

By accessing the laser illuminated end view we were able to realize the streamwise vortical structure associated with the vortex ring/moving wall interaction. We will discuss the interactions which were observed the most in the turbulent layer, that is, the interactions in which a pair of long streaks were observed as being either stable or unstable.

#### **3.4.1. Slow rings ( $U_r/U_w < 0.35$ ) moving towards the wall with a shallow angle (3 degree)**

The conditions of the case discussed here are shown as point 'A' in Fig. 3.18. These initial condition result in a main hairpin, a pair of low streaks  $x^+ = O(1000)$ , a pocket, and hairpins induce themselves and portions of the streaks to lift-up. By sending the laser sheet to different locations we were able to resolve the vortical structure at different parts of the interaction.

The main hairpin was observed to form first; the sign of the hairpin vortex is shown in Fig. 3.20. Evidently, it was a vortex loop; the core is about  $5-10y^+$  and the distance between two legs was about  $50-60 z^+$  in the spanwise direction. This hairpin vortex was the wall layer fluid induced and lifted up by the lower lobe of the vortex ring. After the hairpin vortex was lifted up from the wall, it was stretched and diffused. The visual evidence showed that this hairpin vortex lasted about  $50 t^+$ . Even though we still can visual the organized dye marker associated with the lifted hairpin at the later stage of the vortex ring/moving wall interaction, however, the laser illuminated end view suggested that there was not much vortical motion in this hairpin vortex.

Fig. 3.21 shows the evolution of the vortex pair which was observed to be associated with the streaky structure. There are  $10 t^+$  between photos. As this vortex pair induced itself up, it was getting bigger and bigger and its size could be about  $25-30 z^+$  extending about  $200-300 x^+$  in the near wall region ( $y^+ < 10$ ). The three-view visualization showed that even before the streamwise vorticity,  $x$ , rolled into vortices, the top view had already shown the wall layer dye marker being gather together to form streaks (see Fig. 3.21 (b)). After the vortex pair was observed to form, it induced itself up and broke up. This quick lifting and breakup lasted only about  $20 t^+$ . Mainly, the dye marker associated with the observed breakup was from this vortex pair. Only the top view could not tell the difference between the streamwise vortices and the long streaks. Fig. 3.21 (b) shows clearly the evidence of the formation of the secondary hairpin vortices over streaks; especially in the region near the pocket.

Three-view visualization also showed that as the pocket vortex (Falco 1980b) entered into the viewing window (laser illuminated end view), suddenly, the lifted vortex pair was turned inward in the rotating direction of the pocket vortex (Falco 1980b). This inward motion caused the lifted vortex pair to break-up. However, there was no dye marker present in the vortical structure of the pocket vortex. One possible reason for this may be due to the dye marker which had been pushed away to form streaks in the earlier stage of the interaction.

Based upon the results of three-view visualization on vortex ring/moving wall interaction model, we summarize the interaction into one picture. Fig. 3.22 shows a conceptual picture describing the spatial relationship of the formation of visual features observed in the vortex ring/moving wall interaction including the main hairpin vortex, secondary hairpin vortices, long streaks, and pocket; the arrows indicate the flow direction.

### 3.4.2. Fast rings ( $U_r/U_w > 0.6$ ) moving away from the wall with a shallow angle (less than 3 degree)

Fig. 3.23 (a) is a photo showing the laser illuminated end view visualization under the those initial conditions. The observed long streaks were just the legs of the lifted hairpin vortex; they were one unit. The dye marker actually concentrated with the streamwise vortices. The sign of the vorticity shown in Fig. 3.23 (b) is consistent with that associated with the hairpin vortex shown in Fig. 3.20 (b). Fig. 3.24 shows the conceptual picture summarizing the spatial evolution of this type of vortex ring/moving wall interaction.

## 3.5. Implications for turbulent boundary layers

### 3.5.1. Connection between vortex ring/wall layer description and the typical eddy/wall layer interaction

#### 3.5.1.1. Outer region of turbulent boundary layer

To interpret the results of the vortex ring/moving wall interactions in terms of turbulent boundary layer interactions, we must perform a Galilean transformation on the velocity field. Our interpretation of the simulation has been to identify the Stokes' layer with the viscous wall region which extends to  $y^+$  approximately 30-50. The mean velocity at this height is approximately 70 - 80% of  $U$ . Thus,

$$U_{TE}/U = a(1 - U_r/U_w)$$

where 'a' represents the outer region velocity defect which we can not simulate (20-30%). Thus, in thinking about the implications for the turbulent boundary layer, basically high speed ratios in the simulations correspond to low convection velocities of the typical eddies in the boundary layer.

#### 3.5.1.2. Inner region of turbulent boundary layer



As far as the shear condition in the near wall region is concerned, we can estimate the velocity gradient at the wall by using the exact solution of Stokes' layer. The velocity of the moving wall used in the vortex ring/moving wall interactions ranges from 0.076 m/sec to 0.152 m/sec which corresponds to 0.65 to 0.25  $U_T/U_w$  or 0.35 to 0.75  $U_{TE}/U$ , and the belt running time is between 2 and 6 seconds: resulting in the ratio of the friction velocity to the wall velocity,  $u_\tau/U_w$ , is between 5.5% and 3.5%. This range of the friction velocity is very close to what is found in low Reynolds number boundary layer flows. However, due to the unsteady nature of the Stokes' layer, for each fixed velocity of the moving wall, the percentage of  $u_\tau/U_w$  decreases monotonically during each experiment. This variation in  $u_\tau/U_w$  is approximately 1% over the course of any given experiment. This is slightly different from the real situation in the near wall region of turbulent boundary layer where the friction velocity is stochastically stationary.

### 3.5.1.3. Inner/outer region interaction

As a result, we expect the typical eddies that emerge from wall layer fluid (through a pinch-off of lifted hairpin vortices, for example) to have a low convection velocity. Since these are moving away from the wall, they will correspond to fast rings moving away from the wall. These exhibit long streak formation which is stable, and pinch-off, depending upon the thickness of the wall layer. We do see long stable low speed streaks in the boundary layer (Falco 1980), and we have limited evidence of hairpin pinch-off (Falco 1983). On the other hand, typical eddies that are convecting towards the wall will be of relatively high speed, and thus simulated by low speed vortex rings moving towards the wall. These will produce long streaks which go unstable (undergoing either wavy or lumpy instabilities), short streaks which go unstable, and pockets in all cases. Again we see all these events in the turbulent boundary layer. Fig.

3.25 shows a comparison with what were observed by Offen, Kline (1975) and Smith (1978). The similarity is apparent.

The wide range of interactions that can be simulated using the vortex ring/moving wall experiments are not all admitted by the turbulent boundary layer with equal frequency. Some are not admitted at all. The range of the parameters (angle, wall layer thickness, convection velocity) found in the boundary layer are limited, and in all cases they have skewed probability distributions (towards higher values) that are approximately lognormal. When these distributions are used to determine the events that are most probable, we begin to see what to expect.

### **3.5.2. Spacing between streaks**

Fig. 3.26 shows the distribution of  $D^+$  obtained from the diameter of the typical eddies of a turbulent boundary layer at  $Re_\theta \cong 1176$  (Falco 1974), superimposed upon the streak spacing obtained for various size rings. When the simulation outcomes are conditioned by the probabilities of scales found in this boundary layer, we see that the simulation gives a most likely streak spacing of approximately 100 wall units. This is an important quantitative test of the quality of the simulation, for although the average streak spacing is  $Z^+ = 100$ , all observations of streak pairs have also shown their spacing to be approximately this value.

### **3.5.3. The vortical motions associated with the streaky structure**

The three-view visualization realized the vortical motions associated with the streaky structure in the vortex ring/moving wall interaction (see Sec. 4.3.4). We may interpret as follows. When the coherent motion moves towards the wall from the outer region, the pressure gradient at the wall in the spanwise direction will cause the creation of the streamwise vorticity and roll up into vortices later on. The size of the

counter-rotating streamwise vortices observed to be associated with each streak resulted from the vortex ring/moving wall interaction (see Fig. 3.21) is very much different from the familiar sketch of the counter rotating vortices (see Fig. 3.27) in turbulent boundary layers which was hypothesized by many investigators.

Some investigators hypothesized that the lifted hairpin vortices found in the wall region of the turbulent boundary layers were responsible for the formation of the low speed streaks. However, this phenomenon was not observed in the vortex ring/moving wall interaction simulation. The main hairpin is observed to form due to the interaction between the lower lobe of the vortex ring and the wall layer fluid; its strength depends on how close the ring can approach (this is just what was defined as four Types of interaction). This lifted hairpin will not last long enough to form such a long streak which is about  $1000 x^+$ . Because soon after it is lifted, it may either get ingested into the lower lobe of the ring and lose its coherence or stay in the low shear region. However, in the second case the two legs of the hairpin are too far apart (see Sec. 4.3.4.1) as well as too far away from the wall (the tip of the hairpin will reach as far as  $40 y^+$ ), it is not possible to form a streak between the legs; and the laser illuminated end view indicates that even if this lifted hairpin does not get ingested into the vortex ring it will not keep its coherence over  $30 t^+$ . Some interactions (Fig. 3.8 and 3.21 for examples) do result in the formation of the secondary hairpin vortices over streaks, this phenomena is a consequence of the viscous effect between the two vortices of each streamwise vortex pair and is not the initiator of the formation of the streaks. This is also shown clearly in the conceptual picture in Fig. 3.22.

As mentioned in Sec. 4.3.4.2, the fast vortex ring moves away from the wall which corresponds to the vortex ring moving away from the wall with low convection velocity in the turbulent boundary layer. The observed long streaks are just the legs of

the lifted hairpin vortex; they are one unit. The dye marker actually concentrated with the streamwise vortices. Thus, this type of interaction should not be confused with the typically assumed non-vortical structure of streaks.

We have very limited information about distributions of this type for the angles of incidence and/or movement away from the wall, for the convection velocity, and for the instantaneous wall layer thickness, but the evidence indicates that the frequency of occurrence of many of the interactions which we can simulate is quite low in the turbulent boundary layer. Often these interactions are very intense. Thus, the conditions in the boundary layer that exist which keep their probability low are likely to be essential to the maintenance of the measured values of the drag. We need to explore ways to further limit the occurrence of the violent breakups if we are to pursue a rational program of drag reduction (and noise reduction) in the boundary layer. The model allows us to isolate a specific high drag producing event, and carefully study the parameters that it depends upon. We are currently building the sample sizes necessary to more accurately obtain the distributions mentioned above.

#### **3.5.4. Implications for drag modifications**

As we have seen, small changes in the parameters of typical eddy size, incidence angle, convection velocity, and wall layer thickness can alter the evolutions that result when a typical eddy interacts with the wall. Changes in any of these variables which cause a cross over in the boundaries (such as those shown in Fig. 3.18), will result in a change in the drag at the wall.

Consider, for example, the angle of incidence. If we can change the strength of the large scale motions, say, by outer layer manipulators, we can easily change the angle of a typical eddy that is moving towards the wall, and may even be able to change the

direction if it is at a shallow angle, so as to make it move away from the wall. This will affect the stability of both the local eddy wall interaction (interactions of Type I-IV), and the stability of the streaky structure which is created, as well as the formation of new typical eddies via the pinch-off process. Thus, we can affect not only the local drag, but alter the drag downstream by directly interfering with the cyclic production process.

Modifications to the wall that result in small changes in the effective wall region thickness, for example, NASA riblets, will also have an effect on the drag. If increases in wall region thickness above the critical thicknesses can be made (see for example, Fig. 3.18), streaks are more likely to remain stable. Furthermore, the local interactions (Types I-IV) will also tend to be of Type I and II. Thus, the drag can also be reduced.

### 3.6. Summary and Comment

New boundary layer observations in the Turbulence Structure Laboratory, Michigan State University have suggested that long low speed streaks are formed in pairs as the result of the interactions of microscale very coherent vortex ring-like eddies (typical eddies) propagating over the wall. Depending upon the distance from the wall, *the angle of incidence of the eddy with the wall* (both magnitude and sign), the convection velocity of the eddy, and the local thickness of the viscous wall region, different structural features can evolve out of the evolution. The extent of the distance over which a typical eddy could interact with the wall and wall layer flow was a surprise, but means that many coherent microscale eddies that are in the logarithmic region and further out take part in the production process.

The vortex ring/moving wall simulation incorporates all of the evolutions and structural features associated with the turbulence production process. Besides, the results of the three-view visualization present the similar vortical structure associated

with the low speed streaks found in the near wall region of turbulent boundary layers. The vortex ring/moving wall simulation dramatically demonstrates that the pre-existing streamwise vortices are not required to produce streamwise streaks. When the streak spacings obtained in the simulation are conditioned by the probability of occurrence of typical eddy scales found in the boundary layer, we see that the simulation provides the correct streak spacing (approximately 100 wall units). Other possible outcomes of the simulation need to be weighed by the measured probabilities of occurrence of the angles, convection velocities, and length scales of the typical eddies in the turbulent boundary layer to enable us to obtain a picture of the most probable forms of the interactions, and to gain insight into the causes of the interactions which occur with lower probability, that may contribute significantly to the transport. It appears that turbulent boundary layer control leading to drag reduction can be realized by fostering the conditions suggested by the simulations which will increase the probability of having stable interactions.

All the results discussed in this section are from the flow visualization of the vortex ring/moving wall interaction simulations. Flow visualization, however, can only give partial information at best. The three major reasons for this are:

1. flow visualization is strictly valid only in highly energetic motions,
2. flow visualization has characteristics to leave vortical remnants which may lead to incorrect conclusions about the flow kinematics, and
3. the conventional flow visualization techniques are valid for only short time, since once the dye marker has been removed from a given region no information about the kinematics in that region may be obtained.

Thus, in order to verify the conclusion drawn from the flow visualization and to

answer some questions which were not answered through the flow visualization such as the initial conditions in the vortex ring/moving wall interactions: vorticity distribution over the Stokes' layer and vorticity distribution associated with the vortex ring, the velocity distribution associated with the streaky structure, and the streamwise vorticity distribution associated with the streaky structure, it was necessary to make quantitative measurements. The Laser Induced Photochemical Anemometry (LIPA) technique was accessed in this quantification. The results of which are given in the following section.

## 4. QUANTITATIVE REFINEMENT OF THE VORTEX RING/MOVING WALL INTERACTION MODEL

### 4.1. INTRODUCTION

As mentioned in section 3, the vortex ring/moving wall interaction model provided a conceptual picture (shown in Fig. 3.22) describing the spatial information of all visual features observed in the wall region of wall bounded turbulent flows. The flow shown in Fig. 3.22 is completely unsteady and three-dimensional. The best existing probe techniques are not enough in helping us to answer the questions listed in the conclusion of section 3. To the author's knowledge, the photochromic techniques are the unique techniques that enable us to measure nonintrusively the instantaneous fluid dynamic quantities such as velocities, vorticity, circulation, and strain rates over a two-dimensional domain in such a flow field.

We applied both single tracer technique and grid tracing technique to quantify the vortex ring/moving wall interaction model. First, we measured the Stokes' layer flow and also checked the accuracy of the grid tracing technique. Then, we applied those techniques to more complicated measurements associated with the Type II interaction of the vortex ring/moving wall simulation including:

- a) vortex ring flow,
- b) velocity distributions in the wall region, and
- c) streamwise vorticity distribution in the wall region.



## 4.2. STOKES' LAYER MEASUREMENT

### 4.2.1. Introduction

In this section we first discuss the measurement of a Stokes' layer which was approximated by a rapidly started moving belt and was used to simulate the viscous wall layer in the vortex ring/moving wall interaction mentioned in section 3. Although the Stokes' layer flow is the simplest unsteady flow, the measurement is somewhat difficult; so far no measurement has yet been made. Since the Stokes' layer flow is one-dimensional in space (only has diffusion in  $y$ -direction), an exact solution of the Navier-Stokes equations is available. By applying the photochromic grid tracing technique we were able to obtain the instantaneous velocity distribution, velocity gradients, and vorticity distribution across the layer and were also able to test the accuracy of this technique against the exact solutions.

### 4.2.2. Experimental details

Fig. 4.1 presents the schematic representation of the setup of Stokes' layer measurement; the moving belt system is similar to what was used in the water tank. The width of the belt is 17.8 cm, and the distance between the rollers is 152.4 cm with the test position 90 cm downstream of the leading roller. All experimental data were obtained before the leading edge effects reached the test position. Furthermore, the aspect ratio is sufficient to prevent the disturbances generated in the corners from reaching the center of the belt when the data were taken. Therefore, the wall layer flow measured was one-dimensional. The working fluid was deodorized kerosene in which 10 ppm of the photochromic chemical was dissolved. Fig. 4.2 shows the optical set-up for generating the photochromic grid. Because only spanwise vorticity components were

to be measured, the depth of field looking into flow was not crucial. The best orientation for the incident beam is also shown in Fig. 4.2.

Fig. 4.3 shows the flow chart of the control system of the Stokes' layer measurement. Time delay # 1 initiates the excimer laser to generate a photochromic grid as well as calculating time ( $t$ ) involved in the exact solution of Stokes' layer, while time delay # 2 initiates the data acquisition system which includes a 35 mm high speed Photo-Sonic movie camera and background lighting. Usually we start the movie camera 2.5 seconds prior to the data acquisition because the surge time of the camera to its full speed is 1.5 second. The data were recorded on Kodak Tmax ASA 400 film through a micro lens at 200 frames per second. The films were analyzed on a NAC motion film analyzer which is accurate to 0.05 mm.

#### 4.2.3. Results

Fig. 4.4 shows two photos from the result of the Stokes' layer measurement which are 0.05 seconds apart; these photos were taken under conditions with  $U_w = 12.7$  cm/sec and belt running time  $t = 5.25$  seconds; the belt moved from right to left. Fig. 4.5 shows the non-dimensional velocity profile for two belt running speeds; the solid line represents the exact solution. Results of the velocity gradient  $\partial u / \partial y$  obtained from double differentiation and of the spanwise vorticity obtained from circulation approach are shown in Fig. 4.6, where they are compared with the exact solution. Everything is non-dimensional by the similarity variables of the exact solution. In theory, the spanwise vorticity  $\omega_z$  is equal to  $-(\partial u / \partial y)$  in Stokes' layer since  $\partial v / \partial x$  is equal to zero. Because the flow is one-dimensional, incompressible, and does not change with the streamwise coordinate,  $x$ , the continuity equation reduces to  $\partial v / \partial y = 0$ . A check of this across the Stokes' layer is also shown in Fig. 4.6. The mean value of  $(\partial v / \partial y)^*$  across the layer is -0.011 and the standard deviation is 0.095, which corresponds to 1/second.

#### 4.2.4. Discussion and Summary

By applying the photochromic grid tracing technique, we obtained the instantaneous velocity distribution and, for the first time, the vorticity distribution across the Stokes' layer. There is an agreement among the velocity profiles in Fig. 4.5 except in the vicinity of the edge of the Stokes' layer. This may be caused by the free surface effect, the small disturbance from the driving system, and the reading error. The errors involved in the calculation of velocity gradient, the vorticity distribution and the check of continuity equation are of similar magnitude. The absolute value of the error is 2/sec which is consistent with the design error analysis. The deviation of the experimental profile in the near wall region is a consequence of the grid mesh being too large (the largest mesh in vertical direction in Fig. 4.4 is about  $0.15 \delta$ ) to adequately resolve the large value of the gradient  $\partial u / \partial y$ . On the whole, the results are very encouraging, which indicates that by using the exact solutions of Stokes' layer we can estimate the velocity, velocity gradient and spanwise vorticity distribution associated with the undisturbed viscous wall layer for different belt speeds in the vortex ring/moving wall interactions as long as the leading edge effect of the belt does not reach the test position.

The demonstrated accuracy of the photochromic grid tracing technique in Stokes' layer measurement is more than adequate for many fluid dynamic problems. As speed increases 100-fold the accuracy can, in principle, be maintained, since the calibration depends only on a time and a length scale. There is further room for improvement through the use of high resolution image processing. At present, this technique is accurate enough to apply to more complicated flow measurements which will be mentioned in the following sections in the section.

### **4.3. VORTEX RING MEASUREMENT**

#### **4.3.1. Introduction**

The second item to be quantified in the vortex ring/wall interaction is the vortex ring, the source of the excitation. The vortex ring represents a class of flow fields that are of particular importance in turbulent and unsteady flow. Several techniques had been attempted to measure the detailed structure of the vortex ring. The hydrogen bubble technique was attempted by Maxworthy (1972), but the results were inaccurate due to strong axial gradients and associated radial velocities. Hot wire measurements are hampered by probe interference and difficulty of calibration. Recently, numerous investigators such as Sullivan and Widnall (1973), Maxworthy (1977) and Didden (1979) used a two-component laser doppler velocimeter (LDV); although this technique has taken care of the intrusive problem, it is still a single point measurement, and can only be used to get the circulation distribution, not the local vorticity. By using the photochromic grid tracing technique we can obtain instantaneous velocity distribution and vorticity distribution, allowing us to gain deeper understanding of the dynamics of vortex ring flow.

#### **4.3.2. Experimental details**

The experimental set-up used to generate and measure the vortex ring is shown in fig. 4.7. The same ring generating system applied in the water tank was used. The flow chart of the control system for vortex ring measurement is shown in Fig. 4.8. In order to match the Reynolds number of the vortex ring which was used in the vortex ring/moving wall interaction in the water tank, a 19mm inner diameter orifice was used. The kerosene in the reservoir was dyed with chlorophyll to mark the vortex ring

(Fig. 4.9 shows the lower half of ring marked with the dye). This enabled us to easily locate the frames that needed to be analyzed. The flow was axisymmetric, so that we needed only to align our grid through an axis of symmetry and to measure the flow in half of the ring. The measuring window was at four ring bubble diameters downstream of the exit of the orifice.

#### 4.3.3. Results

Fig. 4.9 shows two photos of the result which are 0.07 seconds apart. The instantaneous velocities distributed along two axes of the ring are shown in Fig. 4.10. The instantaneous circulation distribution of the ring is shown in Fig. 4.11, which also shows the results obtained by Sullivan et al. (1973) for different Reynolds numbers along with the Hill's exact solution of a spherical vortex, although there is no solution existing for the experimentally generated rings. Through the circulation approach we obtained the *instantaneous vorticity distribution over a ring*, which is shown in Fig. 4.12.

#### 4.3.4. Discussion and summary

The vorticity distribution obtained from the photochromic technique is the instantaneous vorticity distribution associated with a vortex ring and no use of Taylor's hypothesis is required. To know the time evolution of a vortex ring we must simply generate the photochromic grid at different locations downstream of the orifice or use the moving grid generating system to follow a vortex ring.

Comparing the vorticity and circulation distributions with those obtained by Sullivan et al. (shown in Fig. 4.11 and Fig. 4.12) shows clearly the Reynolds number dependency, even though the ring generating systems are different. Interestingly, the comparison also shows that the circulation distribution associated with the low Reynolds number vortex ring is closer to that of the Hill's spherical vortex.

## **4.4. FLOW VISUALIZATION IN KEROSENE TANK**

### **4.4.1. Introduction**

By using the photochromic grid tracing technique we are able to quantify the Stokes' layer flow and the vortex ring flow separately. These are the two initially independent flow fields. To gain insights into their interaction, in other words, to obtain the optimal spatial and temporal information about interactions such as the strength of the streamwise vorticity associated with the streaky structure and how the streamwise vorticity changes with the time, we must have an overview of the interaction to determine where and when to make the measurements. Thus, flow visualization is needed to make sure that: 1) the same experiments can be repeated in the kerosene tank (required to use photochromic chemical) at the same Reynolds number, and 2) the measurement window is optimal, that is, we will measure most of the events of interest at the chosen position and time.

### **4.4.2. Experimental details**

The experimental apparatus for flow visualization in the kerosene tank had the same arrangement and control system as that used in the water tank (see Fig. 3.3), but the scales and materials were different. The width of the moving belt was 17.8 cm; the inner diameter of the orifice was 1.9 cm and its center was located 3.8 cm above the wall. The incident angle of the vortex ring was set at 3 degrees with respect to the moving belt. The plate which supported the moving belt was Teflon, a kerosene resistant material. The kerosene in the reservoir was dyed with chlorophyll to mark the vortex ring. As far as the dye marker in the wall layer is concerned, we gently injected the chlorophyll dyed kerosene by a syringe to cover some part of the belt before each run and waited long enough to let the injected dye settle.

The primary visual data consisted of plan and side view time resolved images which were collected by using a 35 mm Photo-Sonic movie camera with a micro-lens on Kodak Tri-X 400 ASA film. The side view was illuminated by a 300 watt flood light diffused through a white color filter. The top view was illuminated by two 300 watt flood lights from underneath and the white teflon plate worked as a white color filter. The frame rate of the movie camera was 20 frames/sec.

#### 4.4.3. Results

Fig. 4.13 shows one set of photos with both top view and side view describing the time evolution of vortex ring/moving wall interactions in the conditions of  $U_r/U_w = 0.26$ , 3 degrees of incident angle,  $\delta/D \cong 0.18$  and  $U_w = 15.5$  cm/sec. The non-dimensional ring diameter was 120 wall layer units. These pictures show clearly the same features which were visualized in the Type II interaction in the water tank under the same flow condition. A pair of streaks with spacing 140 wall layer units were observed, which is consistent with that shown in Fig. 3.21. Besides, the hairpin liftup and pocket also were observed. This consistency gave us confidence that no appreciable changes during startup resulted because of the factor of two increase in viscosity. Through the evolution of the interaction we were able to locate the position where the photochromic tracer or grid will be sent.

By sending a single photochromic tracer parallel to the moving wall at  $y^+ \cong 16$  we obtained the visual result of the interaction shown in Fig. 4.14 which is the same as that obtained from the hydrogen bubble technique used by many other researchers, such as Kim et al.(1971) or Smith et al.(1983).

#### 4.4.4. Discussion and summary

The result of the flow visualization of the vortex ring/moving wall simulation in

kerosene tank showed the same features which were observed in the Type II interaction in the water tank. Those visual results also provided the information to locate the optimal position for the velocity measurement. Furthermore, the vortex ring/moving wall interaction model could produce the same visual features which were visualized through the hydrogen bubble technique in the near wall region of wall bounded turbulent flows.



## **4.5. VELOCITY DISTRIBUTION ASSOCIATED WITH THE VORTEX RING/ MOVING WALL INTERACTION**

### **4.5.1. Introduction**

Even though the flow visualization in the vortex ring/moving wall interaction model did show clearly the formation of a pair of streaks, it did not provide information on the characteristics of the streaks except for the spacing between the streaks. If the model is good, the velocity measurement (temporal and spatial information) will show quantitatively the same as that measured and observed in turbulent boundary layers. These measurements will be able to provide insights into how the viscous wall layer responds to the disturbance from the vortex ring during the interaction. Based upon the results obtained from the flow visualization in the kerosene tank, we figured out that if measurements are conducted only in one fixed location, then the location is 25.4 cm (i.e.  $x/D = 8$ ) downstream of the exit of the orifice, where we will be able to monitor the major events of the interaction. In these measurements the photochromic tracer technique was used; it is the only technique available to obtain the velocity distribution precisely and efficiently for this particular flow field. We can generate photochromic tracers either perpendicular (in x-y plane) or parallel to the wall (in x-z plane) and obtain the associated velocity distribution in the mean flow direction.

### **4.5.2. Experimental details**

We repeated the same experiment as we did for flow visualization in the kerosene tank in Sec. 5.4. Fig. 4.15 shows the locations of measurement. Because we could only record one photochromic tracer for each run in the spanwise direction (z-direction), we needed to repeat the same experiment several times to obtain the whole information in the z-direction. The high repeatability of vortex ring/moving wall interaction did provide the reliability to put the measurements together from different

runs ( the variance of the velocities of the vortex ring and the moving belt are less than 5% for different runs). We only measured half of the flow field as shown in Fig. 4.15, because the flow field was symmetric about the center line (see Fig. 4.15 also). A special optical apparatus was designed for this purpose; a movable carriage which was controlled precisely by a threaded rod carried a set of optical components including one 500 mm focal lens and two reflecting mirrors to accurately guide the laser light beam to the measuring positions. Fig. 4.16 shows the details of the optical configuration. The Excimer laser was set to pulse 10 times per second and the 35 mm Photo-Sonic movie camera was also set at 10 frames per second. We synchronized the belt running system and data acquisition system. As the switch was turned on, the belt, camera, background lighting (a 300 watt flood light) and movie camera started simultaneously. The instantaneous time lines which represented the instantaneous velocity distribution in the streamwise direction were recorded on T-MAX 400 ASA film through a micro-lens. The films were processed with Microdol-X at 70 degrees F for 10 minutes and were digitized by a NAC film analyzer. For each frame we could measure the non-dimensional velocity components,  $U(y)/U_w$ , at different  $y$  positions.

#### 4.5.3. Results

We analyzed the data for each measurement point and obtained the spatial and temporal velocity information of the wall layer as follows:

1. Fig. 4.17 (a) through (d) show the time evolution of the non-dimensional streamwise velocity distribution at the measurement points. The dotted lines represent the undisturbed velocity profiles of the Stokes' layer. The visual information corresponding to Fig. 4.17 is shown in Fig. 4.13; the arrows indicate the measured location.

2. Fig. 4.18 (a) through (d) show the time evolution of the constant streamwise

velocity lines in y-z plane. Again, the dotted lines represent the constant velocity levels of the undisturbed Stokes' layer.

#### 4.5.4. Discussion and summary

Fig. 4.17 shows that the wall layer fluids are accelerated, decelerated, and then lifted up. The results shown in Fig. 4.18 indicate that there is a distinct region of high momentum fluids being pumped away from the wall. As the results shown in Fig. 4.18 are compared with those obtained from flow visualization shown in Fig. 4.13, we found that the long streaks observed by the flow visualization in the vortex ring/moving wall interaction simulation (discussed in Sec. 4.3.1.2, 4.4.1 and 5.4) were the high speed region. This phenomenon also confirms what was observed in the three-view flow visualization in Sec. 4.4.1 (see the laser illuminated end view in Fig. 3.21), where a pair of counter-rotating streamwise vortices associated with each streak was observed. The pair of counter-rotating streamwise vortices pumped the high momentum fluids away from the wall. Again, the width of each streak is also about  $30 z^+$  (see the hump in Fig. 4.18 (c)).

As the results shown in Fig. 4.17 and 4.18 were observed from the point of view of the turbulent boundary layer by performing the Galilean transformation (see Fig. 4.19), we see clearly that the vortex ring/moving wall interaction model can simulate the characteristics of the low speed streaks observed in wall bounded turbulent flows. The data shown in Fig. 4.19 represent the velocity defect or gain with respect to the undisturbed wall layer (i.e the layer after performing the Galilean transformation shown in the lower half of Fig. 4.19 (a)) at different  $y^+$ . The characteristics of the low speed streaks found in Fig. 4.18 and 4.19 are listed as follows:

- a) the spacing (distance between the peak of humps)

is about the size of the vortex ring (see Fig. 4.18(c), 4.19(c) and Fig. 3.26); note that the ring bubble diameter in this measurement was 3.18cm (1 1/4 in);

- b) the region and the percentage of the velocity defect is clearly shown; for example, a 30 % of velocity defect is found at  $y^+ = 15$  (Fig. 4.19(c));
- c) the width of each streak (if it is defined as the region in which the velocity defect is over 10 %) is about  $30 z^+$  at  $y^+ = 10$  (Fig. 4.19 (c) and is about  $20 z^+$  at  $y^+ = 10$ ; and
- d) the extent of coherent liftup may reach about  $y^+ = 40$  (see Fig. 4.18 and 4.19).

These results compare well with those obtained from turbulent boundary layer flows. (see Smith & Metzler 1983)

Besides, the results shown in Fig. 4.18 precisely define the spanwise location of the test window for measurement of the streamwise vorticity associated with the streaky structure.

## **4.6. STREAMWISE VORTICITY MEASUREMENT ASSOCIATED WITH THE VORTEX RING MOVING WALL INTERACTION**

### **4.6.1. Introduction**

From the result of the three-view visualization of the vortex ring/moving wall

interaction in water tank, we observed the vortical structure associated with the streaks, which showed that a pair of counter-rotating streamwise vortices accompanied each single streak in the later stage of the streak formation. This phenomenon is similar to what was found by Blackwelder and Eckelmann (1979). The morphological comparison was mentioned in Sec. 4.5.3. Blackwelder and Eckelmann (1979) studied the vortex structures associated with the bursting process as defined by VITA and estimated the streamwise vorticity by using hot-film sensors and flush mounted wall elements. They found that the streamwise vorticity was one order of magnitude less than that of spanwise vorticity and the middle of the vortex structures lay approximately at  $y^+ = 20$ -30. In this section, we quantify the streamwise vorticity associated with the streaky structure in Type II interaction of the vortex ring/moving wall simulation such that we may have further comparison with the information obtained from the turbulent boundary layers. By using the photochromic grid tracing technique we are able to obtain the spatial and temporal information on streamwise vorticity distribution as well as on the Reynolds stress distribution.

#### 4.6.2. Experimental details

The same experiment which was conducted in Sec. 4.4 and in Sec. 4.5 was repeated in this section. The initial conditions of this vortex ring/moving wall interaction result in a Type II interaction: the incident vortex survives and the pair of streaks break up.

The test area, located at the same position which is 25.4 cm downstream of the exit of the orifice. Because the test area of the photochromic grid tracing technique is limited, we adjusted it to cover a single streak and its adjacent area. It covered from 25 to  $80 z^+$  from the center line of the flow and up to  $40 y^+$  from the moving wall. Fig. 4.20 shows the optical configuration and the orientation of the laser beam. In this

experiment we took advantage of the test area being close to the side window of the kerosene tank, so that we could adjust the laser beams in the grid to be almost orthogonal. This kind of optical arrangement will provide better resolution in the direction which is perpendicular to the wall than that of the diamond shape grid box used in vortex ring and Stokes' layer measurements.

The side view of the data acquisition and lighting system is shown in Fig. 4.21 including the Photosonic 35 mm movie camera, one 300 watt projector light bulb, and white color filter. A F1.2 Nikon lens and a 2.0 x QUANTARAY 7 ELEMENT Auto Tele Converter were used to magnify the image; the background lighting was set at 60% of the output through a potentiometer and was concentrated by a convex lens. The repetition rate of the excimer laser was 2.5 Hz, that is, a fresh photochromic grid was generated every 0.4 seconds. The images were recorded at 50 frames/second on Kodak 400 Tmax films and were processed in Microdol-X for 10 minutes at 70 F. The film was digitized through the NAC film analyzer.

#### 4.6.3. Results

Fig. 4.22 (a) and (b) show the results of the streamwise vorticity measurement, the first photo of each set shown in Fig. 4.22 was photographed at 6.8 and 7.6 seconds respectively after belt started, which corresponded to  $t^* = 55.3$  and 61.8 respectively. Those photos are selected from the same sequence of movie in one experiment. Two photos of each set were 0.02 second apart which corresponded to  $0.5 t^+$  apart.

Following the procedures mentioned in section 2, the data were deduced from each set of the photos and the corresponding contour plots of the instantaneous streamwise vorticity distribution were obtained, which are shown in Fig. 4.23.

Fig. 4.24 (a) through (f) represent the instantaneous Reynolds stress

distributions which were also obtained from the same data base as that of Fig. 4.23 (a) through (f).

#### 4.6.4. Discussion and summary

In the early stage (see Fig. 4.23 (a) and (b)) of the formation of streamwise vortices, the maximum value ( $O(1/\text{sec.})$ ) is about the noise level of this technique. Even at this moment the visualization already shows the nicely-formed streaks at the test area (Fig. 4.23 (a)-(d) almost correspond to the vortical structure shown in the end views of Fig. 3.21 (a)-(d)). It means that even though the level of the streamwise vorticity is very low, it is able to gather the dye marker together to form streaks. However, the velocity information (see Fig. 4.17 (d)) shows that the velocity profile in the mean flow direction appears to have a very strong defect in spanwise direction, that is, it has a very big  $\partial u / \partial z$ .

As we follow the time evolution of the streamwise vorticity distribution shown in Fig. 4.23 (a) and (b), a pair of counter-rotating streamwise vortices induced themselves up to about  $y^+ = 20$ , their strength,  $\omega_x^*$  was about 0.19. which is about one order of magnitude less than the spanwise vorticity (the mean spanwise vorticity,  $\omega_z^*$ , in the wall layer was about 1.04). A photo taken 0.02 second before  $t^* = 58.6$  (shown in Fig. 4.25 (a)) indicates that a pair of counter-rotating streamwise vortices formed from the wall and moved upward. The old photochromic dye marker showed a blurry region in the vicinity of the wall. It means that the fluid in this blurry region has relatively higher speed because it comes from the near wall region and has high momentum. If we look at this from the point of view of the turbulent boundary layer, this is just the low momentum fluid ejected from the near wall region; this argument is also supported by the velocity measurement shown in Fig. 4.17 (c) and (d) (sliced view of velocity distribution in x-z plane shows the corresponding low momentum region). As soon as

the edge of the pocket reached the measuring window (it started shortly before  $t^* = 55.3$ , evidence of this came from the result of visualization both in the water tank and in the kerosene tank; see Fig. 3.21 (b)), this pair of streamwise vortices was dominated by the pocket vortex which may come from the bending of existing spanwise vorticity (see the difference between Fig. 4.23 (c) and (d)). The results show that the contribution from  $\partial w/\partial y$  and  $\partial v/\partial z$  are almost equal; it may suggest this bending of an existing vortex line from the spanwise direction to the streamwise direction. The fast outward spreading of the edge of the pocket suggested that there was a strong pressure perturbation from the incident vortex ring and a strong  $\partial w/\partial y$  contributed to  $\omega_x$ .

The maximum  $\omega_z$  associated with the vortex ring used in this interaction was 35/sec and the maximum measured  $\omega_x$  was about 15/sec which corresponded to about 1/2 of the  $\omega_z$  existing in the wall layer. The ratio  $(\omega_x/\omega_z)_{\max}$  is about 0.43.

The total circulation of the strong vortex (the region with positive sign shown in Fig. 4.23) increased dramatically from  $t^* = 58.6$  to  $t^* = 65.1$ , which is shown in Fig. 4.26. The turning of the direction of the pocket vortex (see Falco 1980b) to the streamwise direction (i.e. the streamwise vorticity component will increase) is a possible reason for the increase of the circulation (see Fig. 4.27). And the area of this strong vortex may be caused by the shape of the pocket vortex as well as the viscous diffusion. It separated about  $20 t^+$  between  $t^* = 58.6$  and  $t^* = 65.1$ ; the viscous diffusion can do something within  $20 t^+$ . This also can explain the decreasing of the peak value of the streamwise vorticity  $\omega_x^*$  from 1.47 to 0.83 within  $20 t^+$  (see Fig. 4.23 (d) and (f)).

The vorticity contours also show the strength of the hairpin which was originally the pair of streamwise vortices associated with each single streak. One leg of this hairpin merged with the pocket vortex and the hairpin vortex was as a whole unit induced by the pocket vortex (Fig. 4.28 shows the possible merging process). Fig. 4.23



(c)-(e) shows the time evolution of this emerging. Fig. 4.26 also shows the total circulation of one leg of this hairpin vortex (the region with negative sign shown in Fig. 4.23). The maximum strength of the streamwise vorticity,  $\omega_x^*$ , associated with this lifted hairpin was about 0.62. and the associated instantaneous Reynolds stress  $\overline{vw}/u_\tau u_\tau$  was low compared with that associated with pocket vortex (see Fig. 4.24 (d), Reynolds stress distribution). This means that the Reynolds stress associated with the streaky structure was low and was about 30% of that of the pocket vortex. Thus, we have a detailed breakdown of the contributions of the long streaks and the pockets to streamwise vorticity and the Reynolds stress produced by it.

## 4.7. Summary

### 4.7.1. The photochromic technique - an accurate and powerful technique

Data derived by the photochromic technique has been used throughout this section. Using a photochromic mesh of small enough size, instantaneous fluid dynamic quantities over a two-dimensional field can be measured. The predicted accuracy through the classical error analysis described in section 2 has been confirmed in the Stokes' layer measurement. Using this technique we have quantified the velocity and vorticity distributions of the two originally independent fluid flows (i.e. the Stokes' layer and the vortex ring) of the vortex ring/moving wall interactions. We have also measured both temporal and spatial information pertaining to the velocity distributions and streamwise vorticity distributions associated with the vortex ring/moving wall interaction.

### 4.7.2. Further understanding of turbulence production process through the vortex ring/moving wall interaction model

The visual and photochromic technique derived results of the vortex

ring/moving wall interaction simulation indicate that this model not only demonstrates qualitative agreement with the near wall boundary layer phenomena but also quantitatively captures the correct kinematical magnitudes associated with this phenomena. This was demonstrated in the velocity measurements associated with the vortex ring/moving wall interaction in that the characteristics of the low speed streaks were fully revealed. Furthermore, the model studies show that the streamwise vorticity associated with the streaky structure is about one order of magnitude less than the mean spanwise vorticity. We realized that the pocket vortex plays a very important role through the streamwise vorticity measurements. The pocket vortex is apparently responsible for the instability of the streaks, and it is the major contributor to the Reynolds stress. The secondary hairpin vortices which formed on the low speed streaks are not as important, in terms of both vorticity and Reynolds stress, as the pocket vortex.

## 5. CONCLUSIONS AND FURTHER COMMENT

### 5.1. Conclusions

As addressed in section 1 work this period involved a combination of both the technical development of LIPA technique and its application towards understanding the basic physics of the bursting process in turbulent boundary layer flows. The major findings of this two phase experimental study can be summarized as follows:

1. A major extension of LIPA (Laser Induced Photochemical Anemometry) that enables the instantaneous velocity, velocity gradient, vorticity, and Reynolds stress to be obtained over a two-dimensional domain of a fluid flow has been developed and demonstrated. Calibration depends only upon a time and a length scale. Comparison of measurements with the exact solution in a Stokes' layer indicates that its accuracy can be predicted by classical analysis, and is comparable or better than that achievable with the best single point probe techniques. Furthermore, the LIPA is not restricted to slowly varying flows as are so many flow visualization techniques. Using the LIPA technique we have also quantified both temporal and spatial information pertaining to the velocity distributions and streamwise vorticity distributions associated with the vortex ring/moving wall interaction.

2. The vortex ring/moving wall simulation incorporates all the evolutions and structural features associated with the turbulence production process. It dramatically demonstrates that streamwise vortices are not required to produce streamwise streaks. When the streak spacing obtained in the simulation is conditioned by the probability of occurrence of typical eddy scales found in the boundary layer, we see that the

simulation provides the correct streak spacing (approximately 100 wall layer units). It also appears that turbulent boundary layer control leading to drag reduction can be realized by fostering the conditions suggested by the simulations which will increase the probability of having stable interactions.

3. The visual and LIPA technique derived results of the vortex ring/moving wall interaction simulation indicate that this model not only demonstrates qualitative agreement with the near wall boundary layer phenomena, but also quantitatively captures the correct kinematical magnitudes associated with this phenomena. This was demonstrated in the velocity measurements associated with the vortex ring/moving wall interaction, in that the characteristics of low speed streaks were fully revealed. Furthermore, the model studies show that the streamwise vorticity associated with the streaky structure is about one order of magnitude less than the mean spanwise vorticity. And finally, the model studies also realize that the secondary hairpin vortices formed on the low speed streaks are not as important, in terms of both vorticity and Reynolds stress, as the pocket vortex.

## **5.2. Further comment**

1. The calibration of the LIPA technique depends on only a time and a length scale; there is further room for improvement. In practice, determining the intersecting points of the grid lines is limited by the grain size of the film used, and the distortion of the developing process. Improvements in the grain limitation can be made by using a large format still camera with a shuttering mechanism that will enable a double exposure of the grid to be made on one plate. Image processing techniques have also been demonstrated to increase the accuracy and repeatability of the results.

2. Current limitations of the LIPA technique include the need to work in organic

liquids, which are required to dissolve the chemicals, and available penetration of the laser beam into the liquid. The way to generalize this technique to be used in popular fluid media is ongoing at the Turbulence Structure Laboratory, Michigan State University. This ongoing research includes the study of new chemicals which can be used for water, and the scanning technique which can be used to improve the penetration problem.

3. The 'moving' LIPA technique can be used to obtain the Lagrangian information in many turbulent and unsteady flows. Its future is very promising.

A detailed description of the related simultaneous hot-wire flow visualization work being performed will be described in a later report.

## REFERENCES

- Acarlar, M.S. and Smith, C.R. 1984, "An Experimental Study of Hairpin-type Vortices as a Potential Flow Structure of Turbulent Boundary Layers", Rept. FM-5, Dept. of M.E./Mech., Lehigh Univ.
- Blackwelder, R.F. and Eckelmann, H. 1979, "Streamwise Vortices Associated with the Bursting Phenomenon", J. Fluid Mech. 94, p 577.
- Blackwelder, R.F. and Kaplan, R.E. 1976, "Burst Detection in Turbulent Boundary Layers. J. Fluid Mech. 76, p. 89-101.
- Brown, G.H. ed. 1971, "Photochromism", Wiley-Interscience, New York.
- Didden, N. 1979, "On the Formation of Vortex Rings: Rolling-up and Production of Circulation", J. Applied Math. and Physics (ZAMP), 30, p.101. Eckelmann, H. 1974, "The Structure of the Viscous Sublayer and the Adjacent Wall Region in a Turbulent Channel Flow", J. Fluid Mech. 65, p.439. Emmerling, R. 1973, "The Instantaneous Structure of the Wall Pressure under a Turbulent Boundary Layer Flow", Max-Planck-Institut für Stromungsforschung Bericht Nr. 9. Falco, R.E. 1974, "Some Comments on Turbulent Boundary Layer Structure Inferred From the Movements of a Passive Contaminant", AIAA Paper 74-99.
- Falco, R.E. 1977, "Coherent Motions in the Outer Region of Turbulent Boundary Layers", Phys. Fluids Suppl. II 20, S124-S132.
- Falco, R.E. 1978, "The Role of Outer Flow Coherent Motions in the Production of Turbulence Near a Wall", in "Coherent Structure of Turbulent Boundary Layers", ed. C.R. Smith and D.E. Abbott pp. 448-461.
- Falco, R.E. 1980a, "The Production of Turbulence Near a Wall", AIAA Paper No. 80-1356.
- Falco, R.E. 1980b, "Structural Aspects of Turbulence in Boundary Layer Flows", in "Turbulence in Liquids" ed. Patterson and Zakin, pp. 1-15.
- Falco, R.E. 1980c: Combined Simultaneous Flow Visualization Hot-wire Anemometry for the Study of Turbulent Flows", J. of Fluids Engr. 102, p. 174-183.
- Falco, R.E. 1982, "A Synthesis and Model of Wall Region Turbulence Structure", in "The Structure of Turbulence, Heat and Mass Transfer" ed. by Z. Zoric', pp. 124-135, Hemisphere Press.
- Falco, R.E. 1983, "New Results, a Review and Synthesis of the Mechanism of Turbulence Production in Boundary Layers and its Modification", AIAA Paper No. 83-0377.

- Falco, R.E., Chu, C.C., and Wiggert, D.C., 1983: "Experiments on Compliant Surfaces Using Quantitative Visual Technique," Symposium on Drag Reduction, National Science Academy, Washington D.C.
- Falco, R.E., Chu, C.C. 1987: "Measurement of Fluid Dynamic quantities Using A Photochromic Grid Tracing Technique," Presented in SPIE 31st Annual Meeting. Foss, J.F., Klewicki, C.L., and Disimile, P.L. 1984, NASA CR. 178098. Head, M.R. and Bandyopadhyay, P. 1981, "New Aspects of Turbulent Boundary Layer Structure", J. Fluid Mech. 107, p. 297-337.
- Hecht, E. and Zajac, A. 1974, "Optics", Addison-Wesley, p.357.
- Hill, M.J.M. 1894, Phil. Trans. Roy. Soc. A 185.
- Kim, H.T., Kline, S.J., and Reynolds, W.C. 1971, "The Production of Turbulence Near a Smooth Wall in a Turbulent Boundary Layer", J. Fluid Mech. 50, p.133.
- Kim, J. 1986, "Investigation of Turbulent Shear Flows by Numerical Simulation", Tenth Congress of Applied Mechanics, Austin TX June 16-20.
- Lang, B.L. 1985, "Laser Doppler Velocity and Vorticity Measurements in Turbulent Shear Layers", Ph.D Thesis C.I.T.
- Liang, S. 1984, "Experimental Investigation of Vortex Ring/Moving Wall Interactions", MS Thesis, Dept. Mech. Engr. Michigan State Univ.
- Liang, S., Falco, R.E. and Bartholomew, R.W. 1983, "Vortex Ring/Moving Wall Interactions: Experiments and Numerical Modeling", Bull. Am. Phy. Soc., Series II, 28, p. 1397.
- Lovett, J. 1982, "The Flow Fields Responsible for the Generation of Turbulence Near the Wall in Turbulent Shear Flows", MS. Thesis, Dept. Mech. Engr. Michigan State Univ.
- Mitchell, J.E. and Hanratty, T.J. 1966, "A Study of turbulence at a Wall Using a Electrochemical Wall Shear-Stress Meter", J. Fluid Mech. 26, part 1, p.199-221.
- Moin, P., Leonard, A. and Kim, J. 1986, "Evolution of a Curved Vortex Filament into a Vortex Ring", Phy. Fluids 29, p.955-963
- Offen, G.R., Kline, S.J. 1975, "A Proposed Model of the Bursting Process in Turbulent Boundary Layers", J. Fluid Mech. 70, part 2, p.209-228.
- Oldaker, D.K. and Tiederman, W.G. 1977, "Spatial Structure of the Viscous Sublayer in Drag Reducing Channel Flow", Phy. Fluids 20 (10), p. 133-44.
- Popovich, A.T. and Hummel, R.L. 1967, "Experimental Study of the Viscous Sublayer in Turbulent Pipe Flow", A.I.Ch.E.J. 14, p.21-25 (1967)
- Praturi, A.K. and Brodkey, R.S. 1978, "A Stereoscopic Visual Study of Coherent

Structures in Turbulent Shear Flow", J. Fluid Mech. 89, p. 251-272.

Runstadler, P.W., Kline, S.J. and Reynolds, W.C. 1963, "An Experimental Investigation of the Flow Structure of the Turbulent Boundary Layer", Dept. of Mech. Engr. Rep. MD-8, Stanford Univ.

Schraub, F.A. and Kline, S.J. 1965, "Study of the Structure of the Turbulent Boundary Layer with and without Longitudinal Pressure Gradients", Dept. of Mech. Engr. Rep. MD-12, Stanford Univ.

Seely, L.E., Hummel, R.L. and Smith, J.W., 1975, "Experimental Velocity Profiles in Laminar Flow around Sphere at Intermediate Reynolds Numbers", J. Fluid Mech. 68, p.591-608.

Signor, D. 1982, MS Thesis, Dept. of Mech. Engr., Michigan State Univ.

Smith, C.R. 1982, "Application of High Speed Videography for Study of Complex, Three-dimensional Water Flows", SPIE 348, "High Speed Photography", p. 345-352.

Smith, C.R. 1978 in "Coherent Structure of Turbulent Boundary Layers", ed. C.R. Smith and D.E. Abbott, p.50.

Smith, C.R. and Metzler, S.P. 1983, "The Characteristics of Low-speed Streaks in the Near Wall Region of a Turbulent Boundary Layer", J. Fluid Mech. 129, p. 27. Sullivan, J.P., Widnall, S.E., and Ezekiel, S. 1973, "Study of Vortex Rings Using a Laser Doppler Velocimeter", AIAA J. Vol. 11, No.10, p.1384. Taylor, J.R., 1982, "An Introduction to Error Analysis", Univ. Sci. Books, Calif.

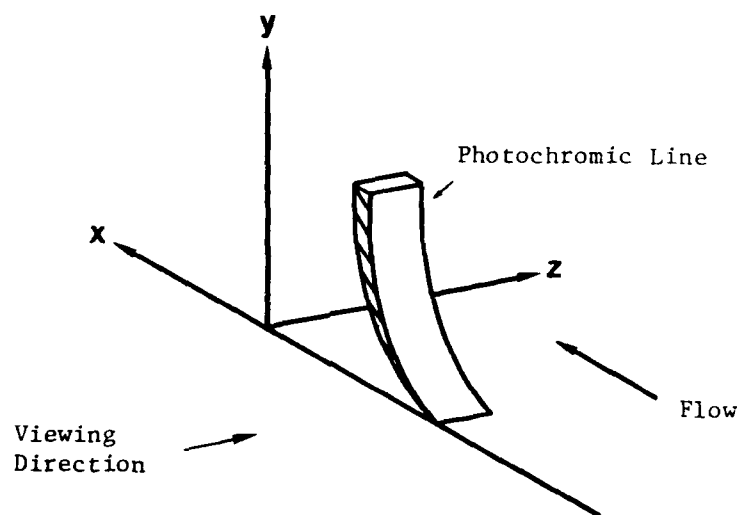
Thomas, A.S.W., Bull, M.K. 1983, "On the Role of Wall-Pressure Fluctuations in Deterministic Motions in the Turbulent Boundary Layer", J. Fluid Mech. 128, p.283.

Wallace, J.M. 1986, Experiments in Fluids, Vol. 4, p.61.

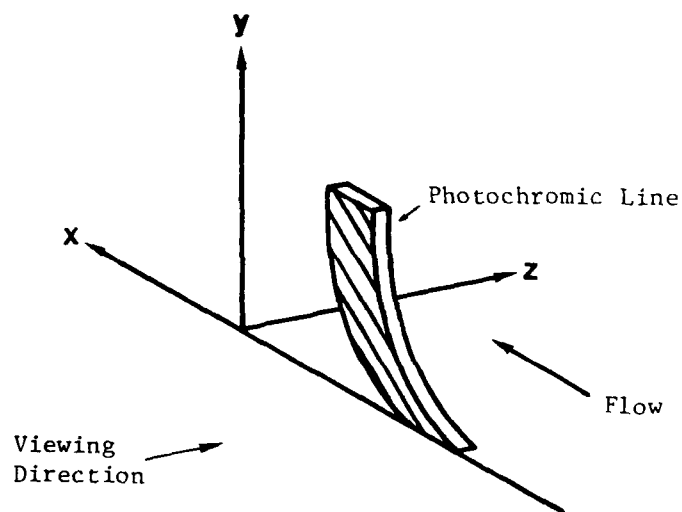
Yoda, H. 1981, "Effects of Dilute Polymer Additives on the Turbulence Structure Near a Wall", MS Thesis, Dept. of Mech. Engr., Michigan State Univ.







**a**



**b**

Fig. 2.2 A schematic of the stretching of the photochromic line in shear flow.

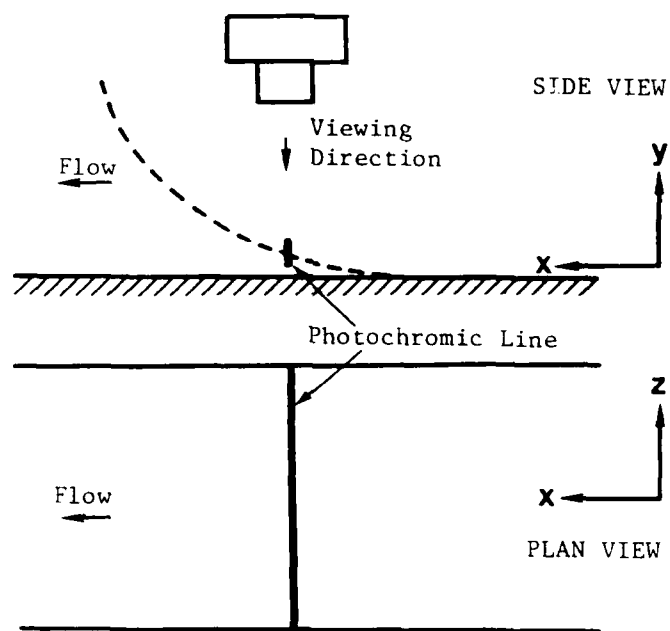
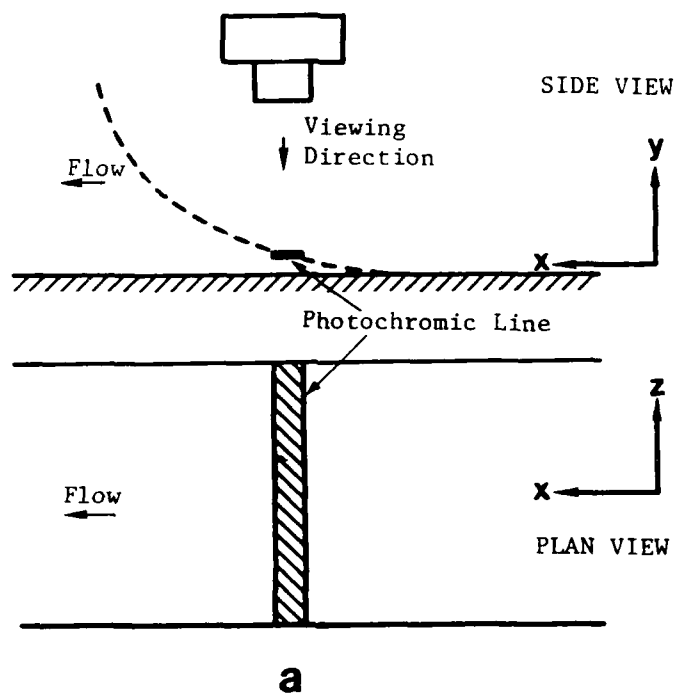


Fig. 2.3 The dependence of the quality of photochromic line on its orientation in shear flow.

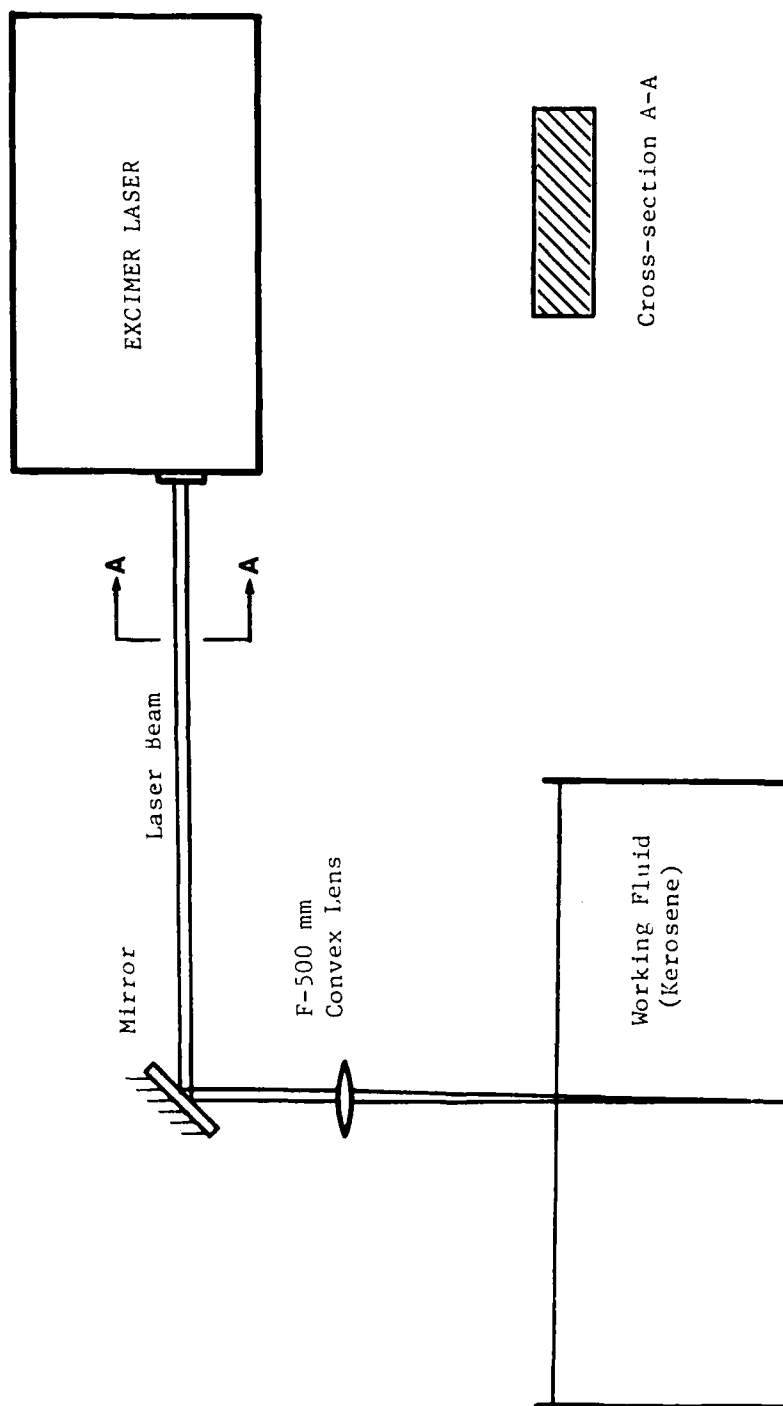


Fig. 2.4 A schematic of experimental configuration for one of the laser beam orientations.

351NM WAVELENGTH, 500 MM CONVEX LENS  
 INPUT BEAM DIAMETER:  $\square$  - 20 mm,  $\nabla$  - 7 mm.

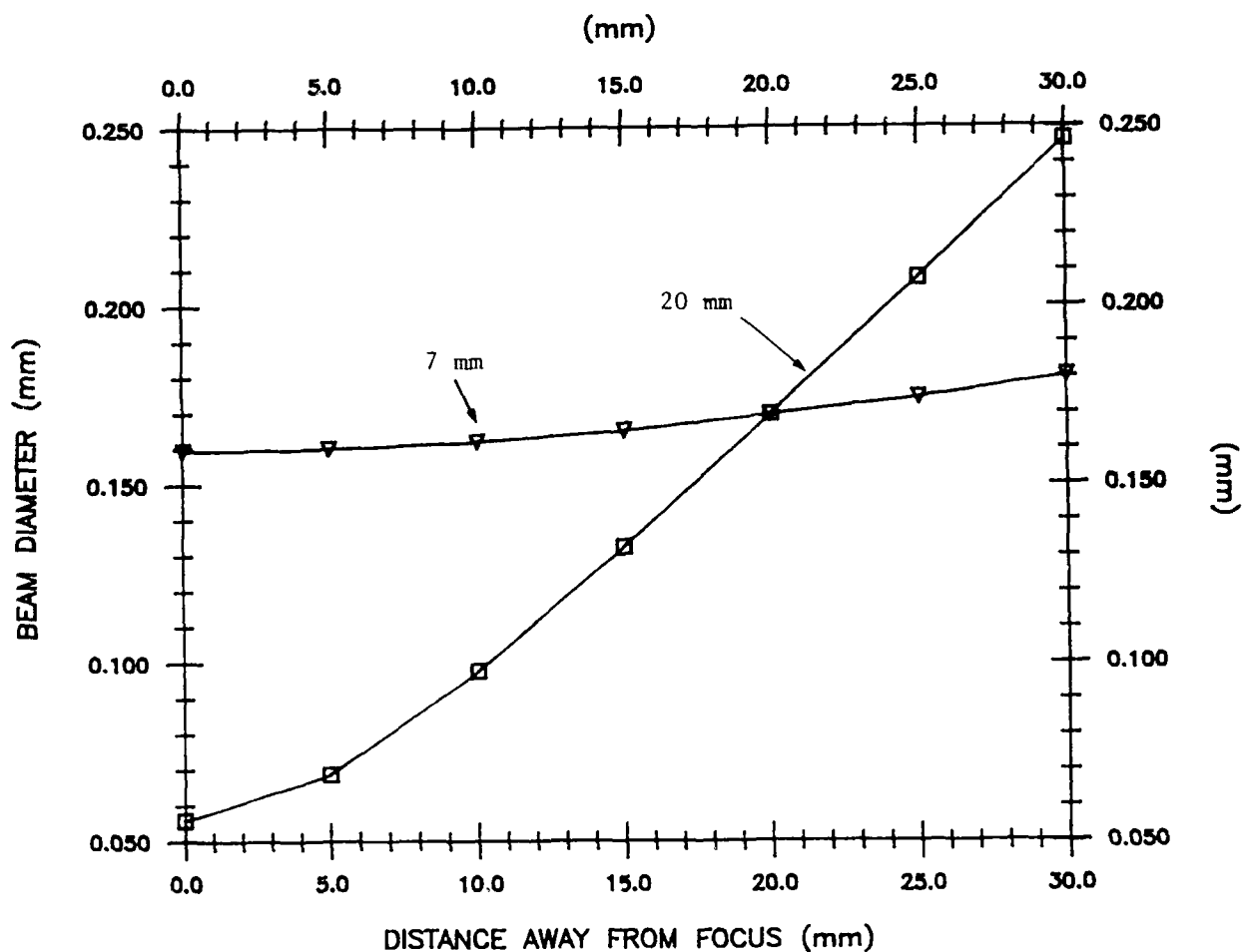


Fig. 2.5 The divergence characters of the laser beam after a F-500mm convex lens.

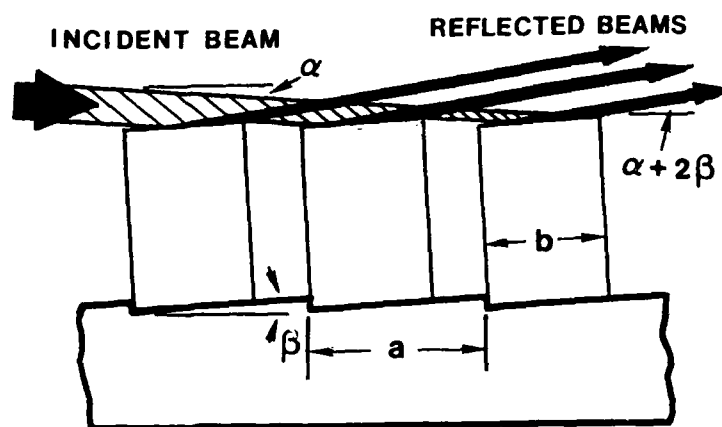


Fig. 2.6 The specular reflection from the beam divider.

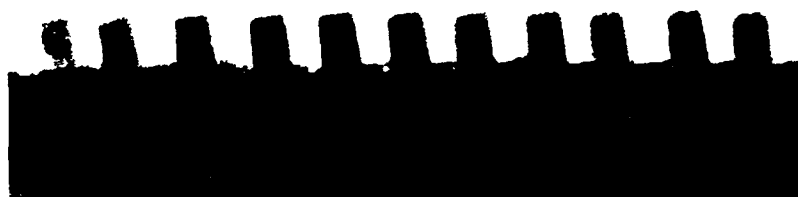


Fig. 2.7 A photo of the beam divider.



Fig. 2.8 A photo of the output of the divider showing the Fraunhofer diffraction.



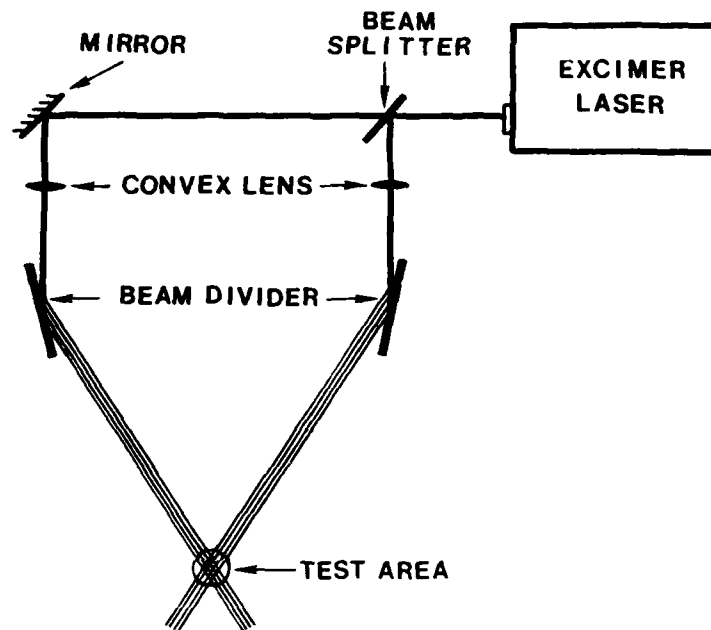
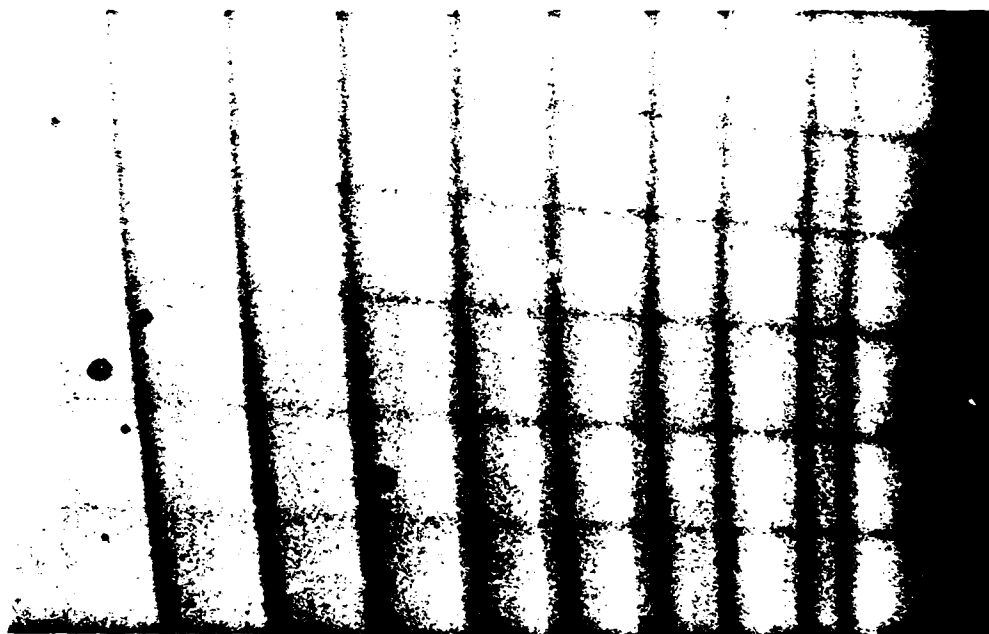
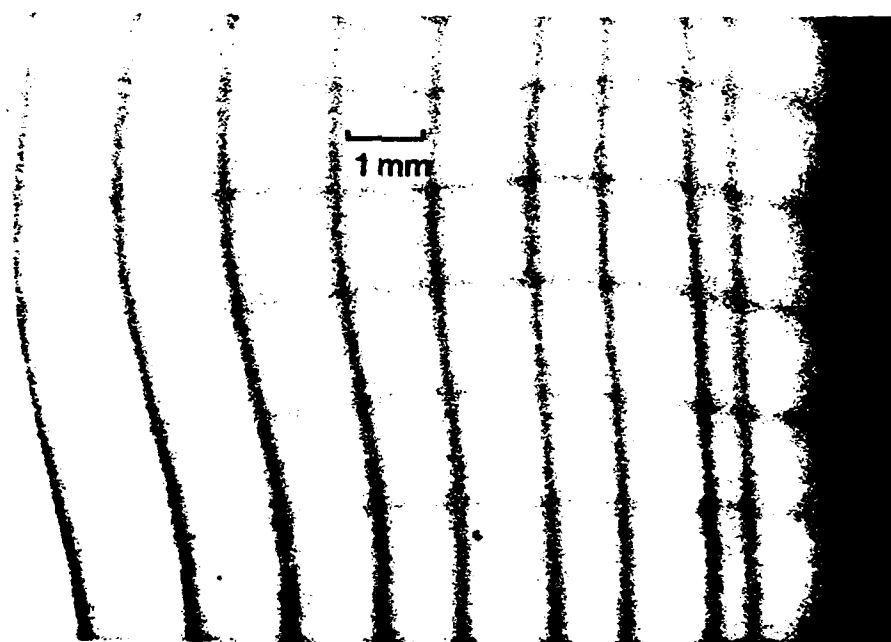


Fig. 2.9 A sketch of the optical configuration for generating a grid in Fig. 2.10 (a).

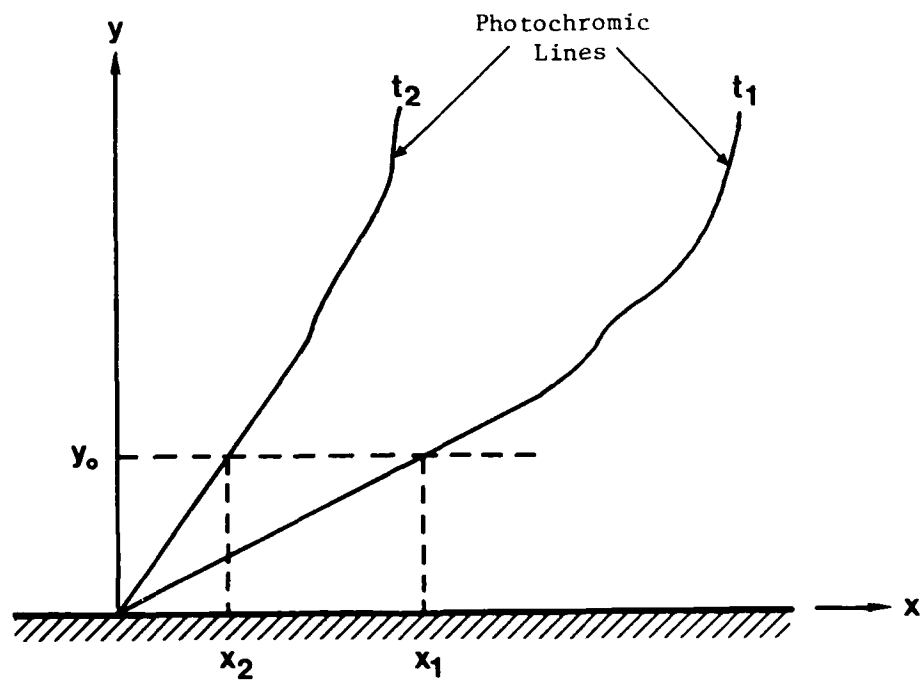


( a )



( b )

Fig. 2.10 A demonstration of the grid; a) shortly after the laser pulse, b) 0.4 seconds later.



$$u = \frac{x_1 - x_2}{t_1 - t_2}$$

$$\tau_w = \mu \left. \frac{\partial u}{\partial y} \right|_w \approx \mu \frac{u}{y_0}$$

Fig. 2.11 Algorithm to obtain the wall shear stress using photochromic technique.

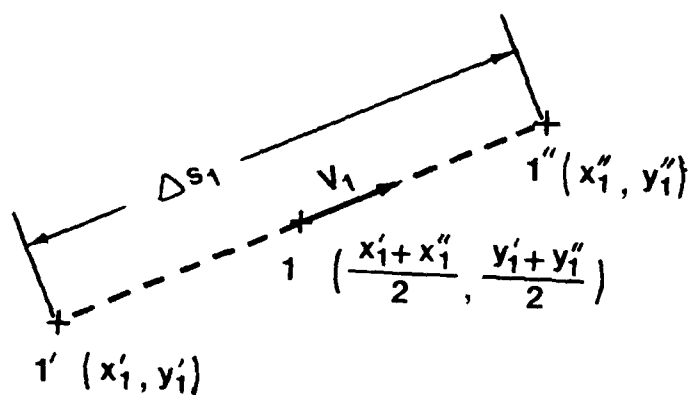
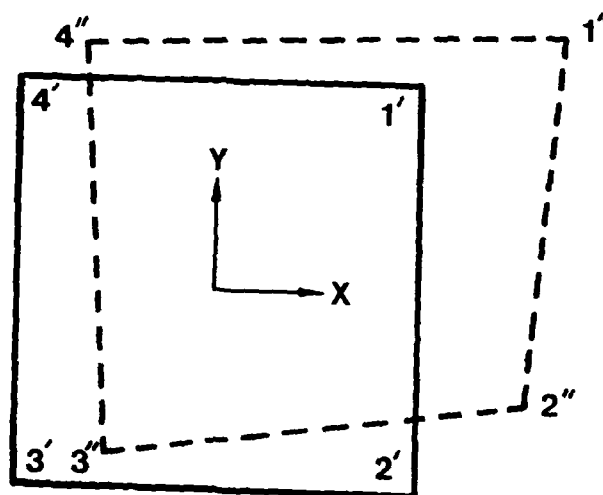


Fig. 2.12 Procedure for conversion of the displacement of a grid box to velocities.

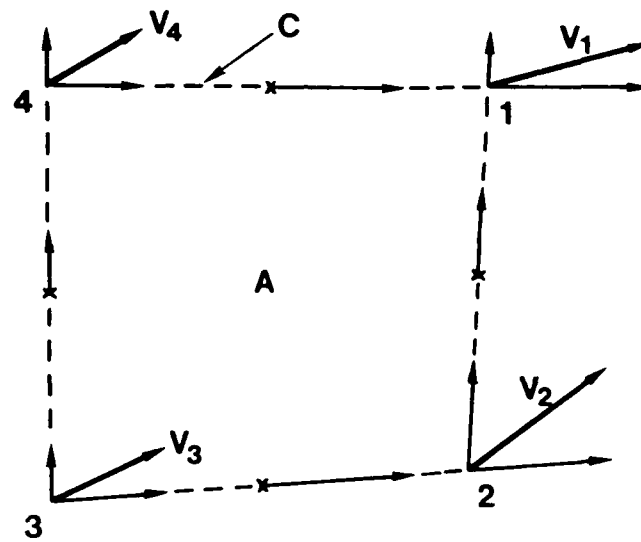


Fig. 2.13 Decomposition of the velocities used to calculate the circulation around a grid box.

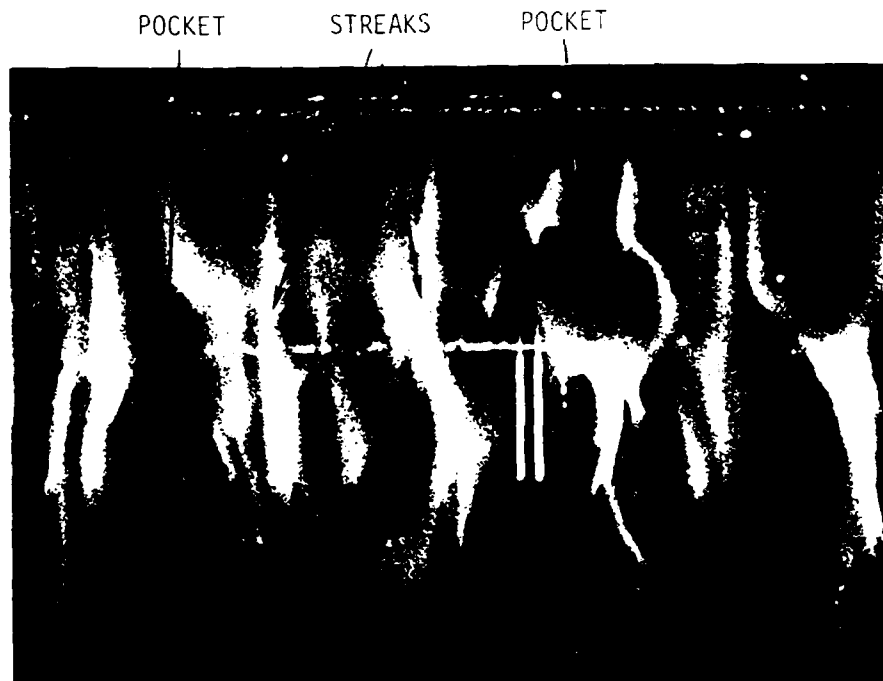


Fig. 3.1 Two pockets and a pair of streaks as seen in wall slit visualization of a turbulent boundary layer using smoke as the contaminant in air, the slit is at the top of the photo and the flow is from top to bottom. (Falco 1981)

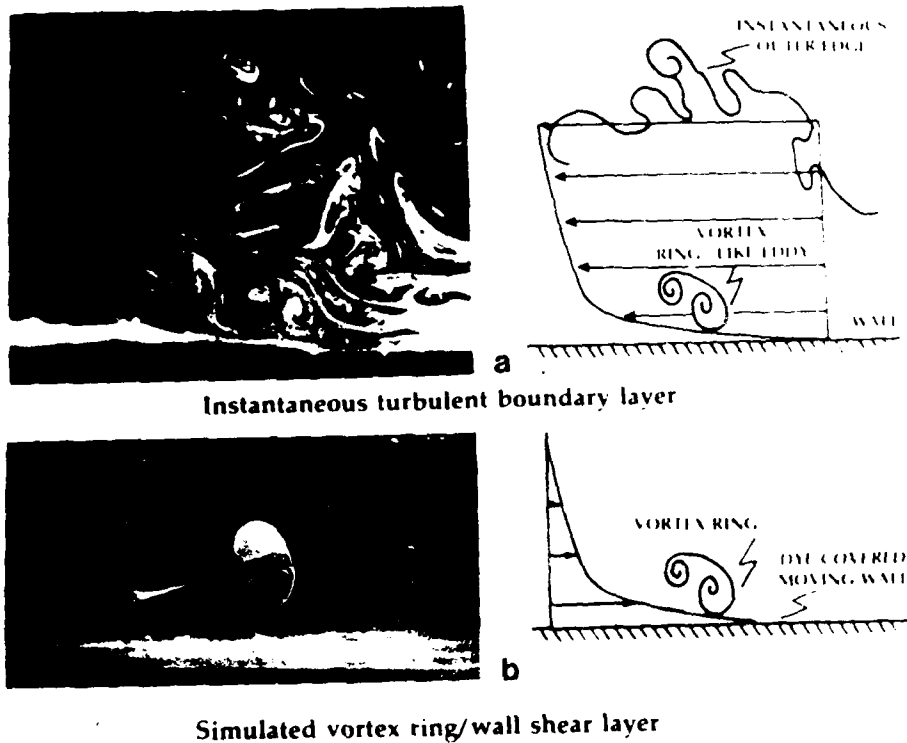


Fig. 3.2 The basic idea behind the simulation. Performing a Galilean transformation on the vortex ring/moving wall interaction makes in a model of the turbulent boundary production process; (a) instantaneous turbulent boundary layer; (b) simulated vortex ring/wall shear layer.

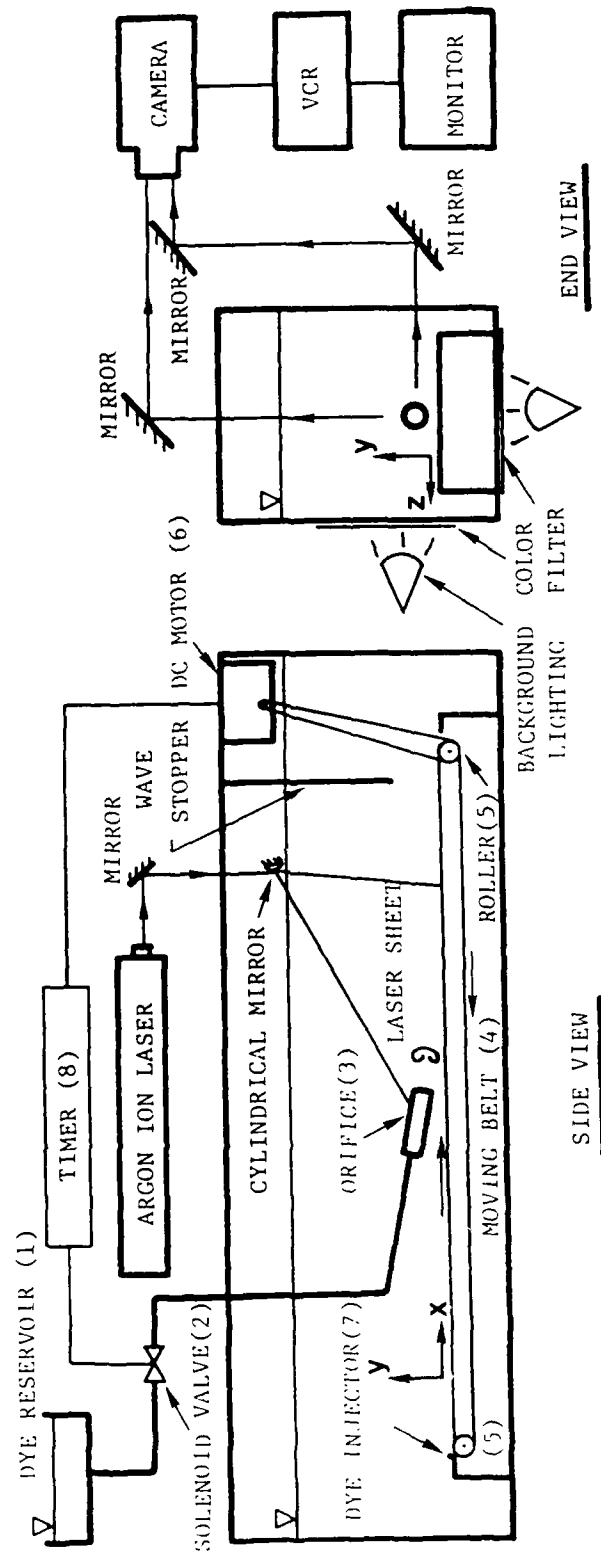


Fig. 3.3 A schematic of the side view and end view of the experimental apparatus used in the vortex ring/moving wall simulations.



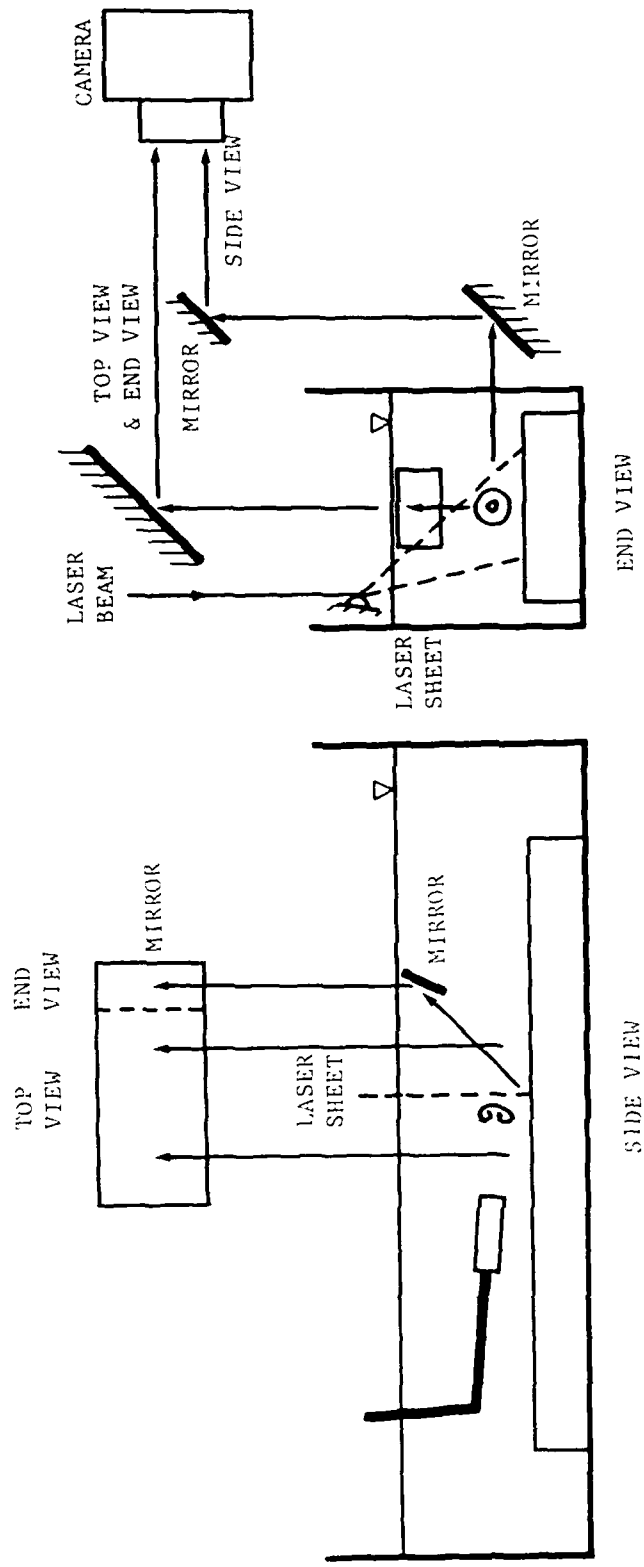


Fig. 3.4 A schematic of the three-view visualization system; note that only the end view was illuminated by the laser sheet.

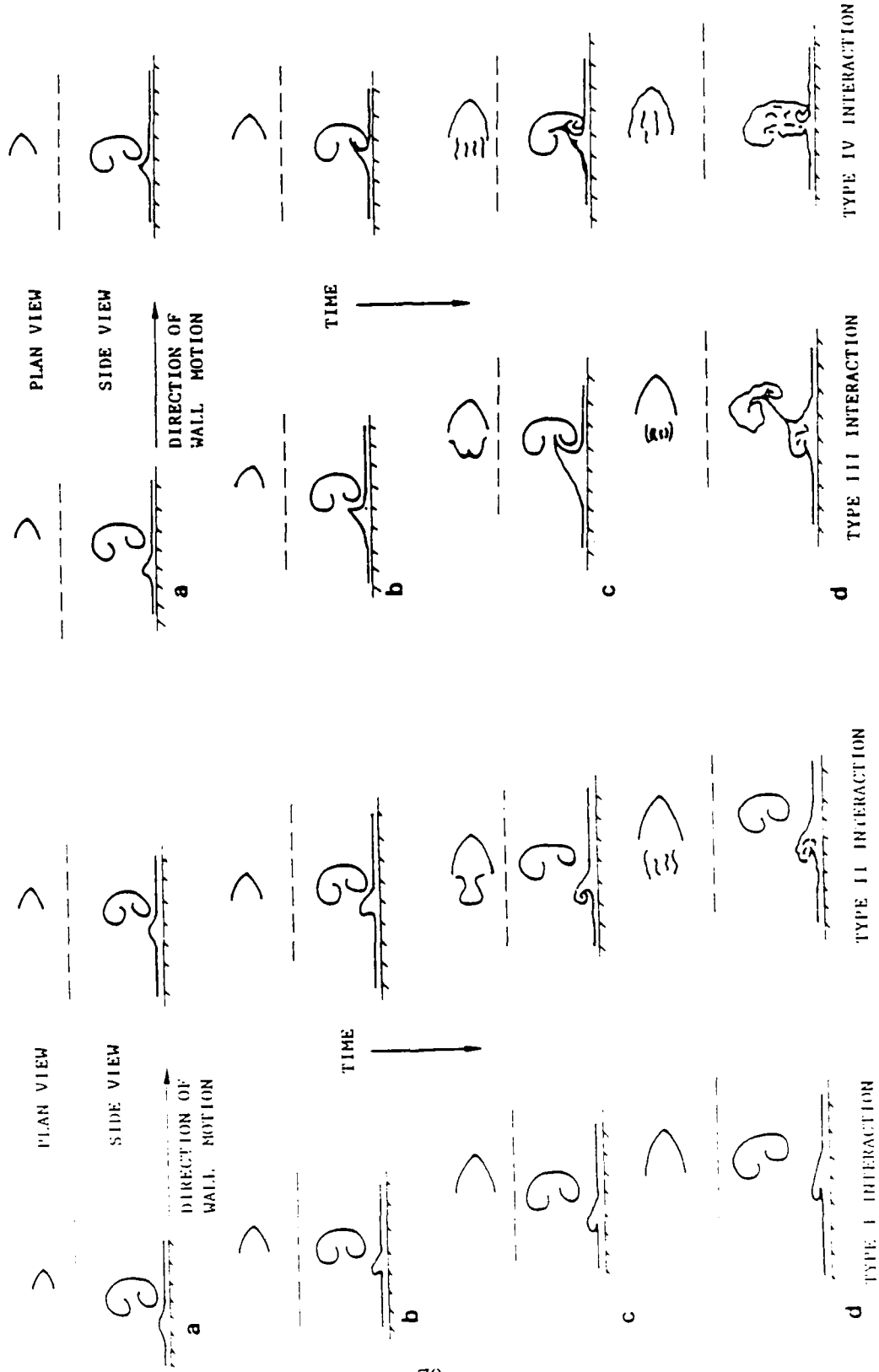


Fig. 3.5 Sketches of the four types of local vortex ring/moving wall interactions (see text for explanation).

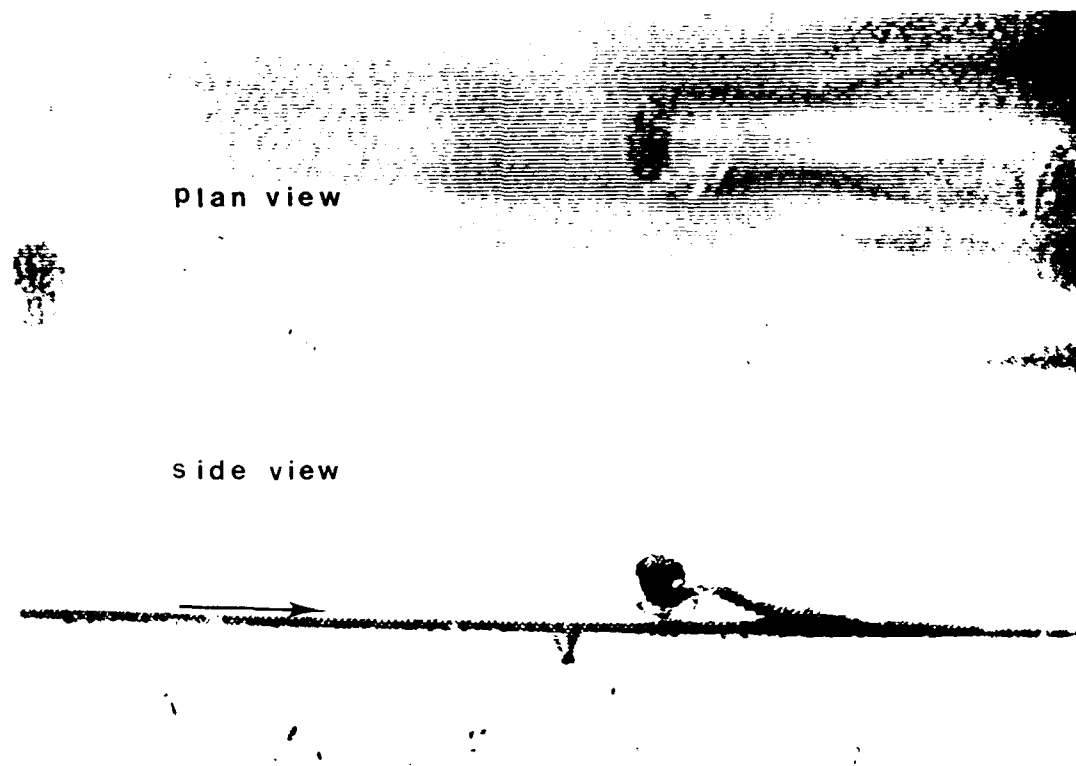


Fig. 3.6 Streaks form from the stretching of the lifted hairpin for  $U_T/U_w \approx 0.8$ .

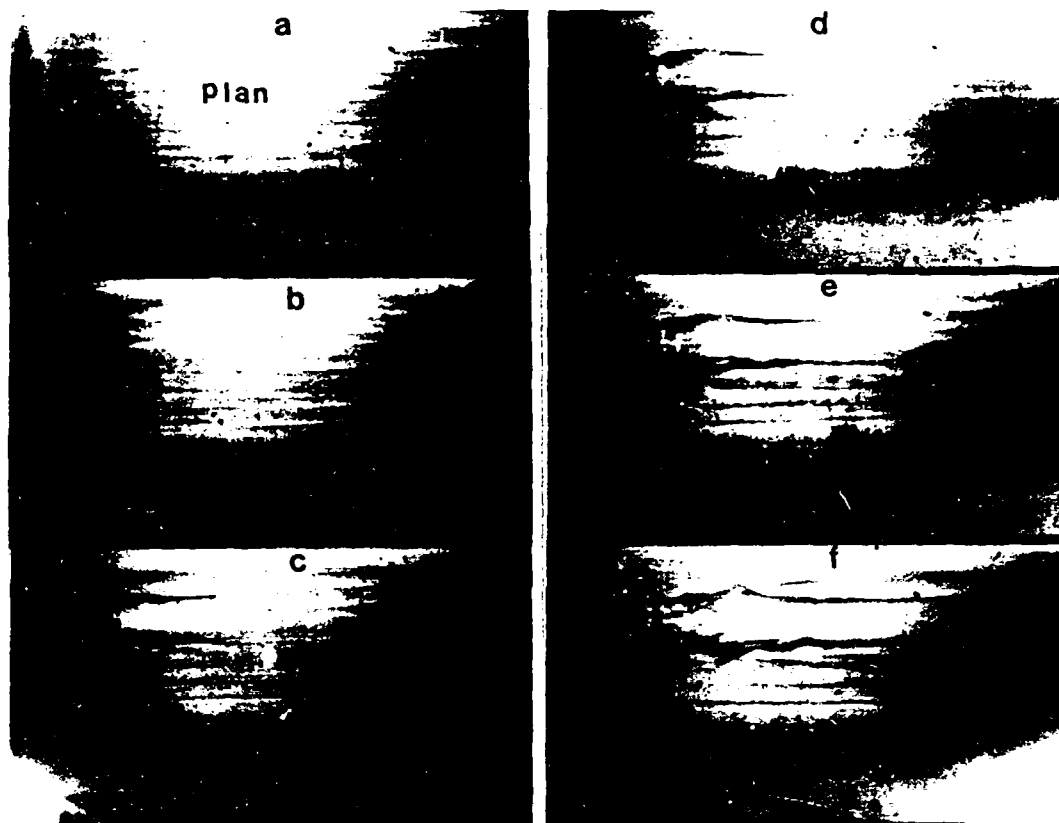


Fig. 3.7 Six photos of a vortex ring/moving wall interaction for  $U_r/U_w < 0.35$  when the ring moves toward the wall at a 3 degree angle. Both plan and side views are shown. The ring and the wall are moving to the right and only the wallward side of the ring has dye in it. The interaction results in a pair of long streaks, a pocket and its associated hairpin lift-up, which then gets partially ingested into the ring.

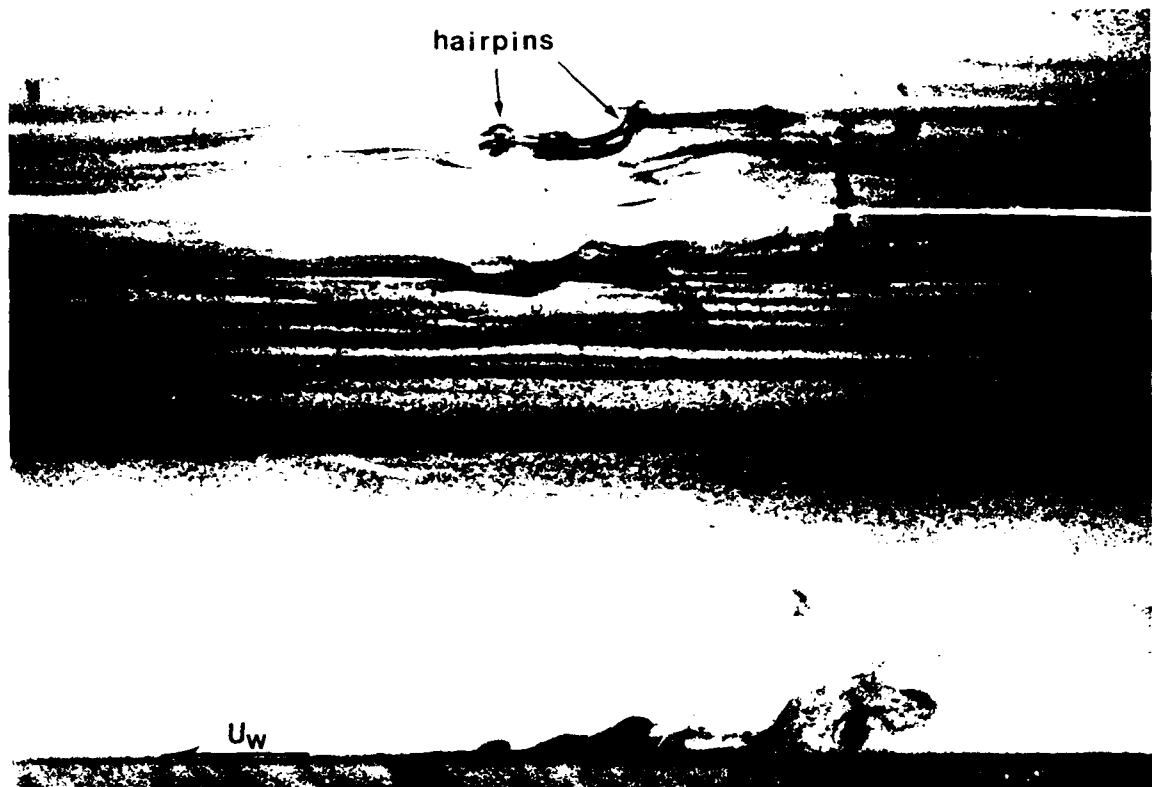


Fig. 3.8 Hairpins form over streaks.

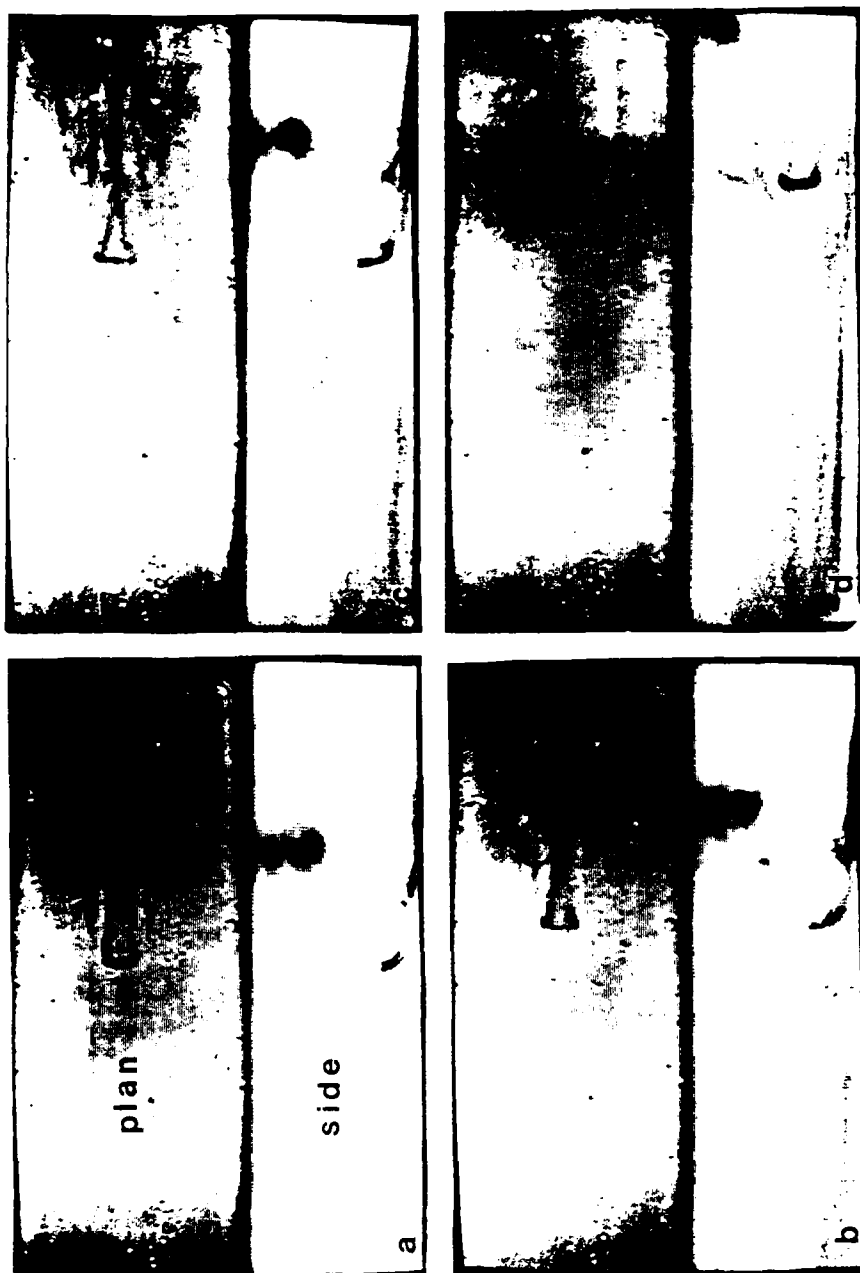


Fig. 3.9 Four photos of a vortex ring/moving wall interaction for  $U_r/U_w > 0.45$  when the ring is moving away from the wall at a 2.5 degree angle. Both plan and side views are shown. The ring and the wall are moving to the right. A hairpin forms first. The long stable streaks which also form, come closer and closer together, indicating that the streamwise vorticity which caused them are of opposite sign. This evolution leads to "pinch-off" and the creation of a new vortex ring.

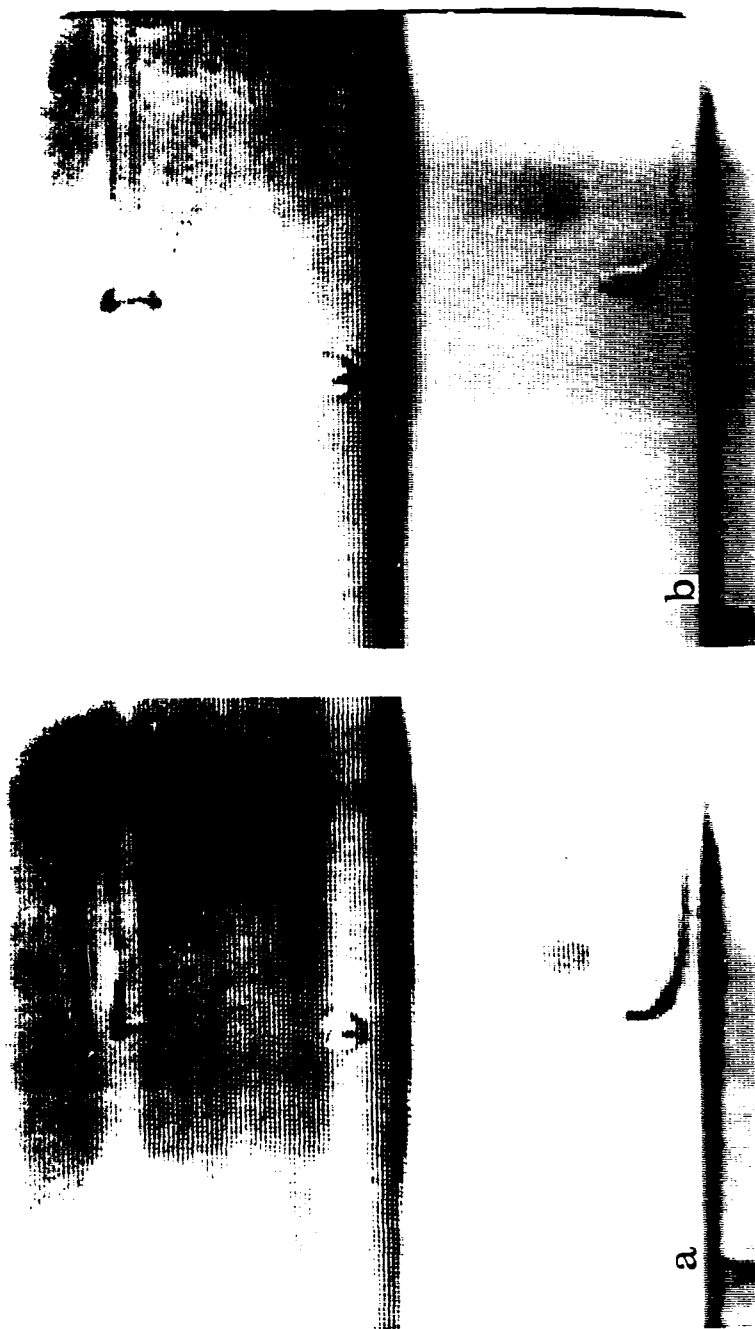


Fig. 3.10 Same conditions as Fig. 4.9, except that the wall layer is very thin. We obtain long stable streaks and a long stretched hairpin which does not pinch-off over 2500 wall layer distance of the facility. The time between each photo is approximately 50 wall units.

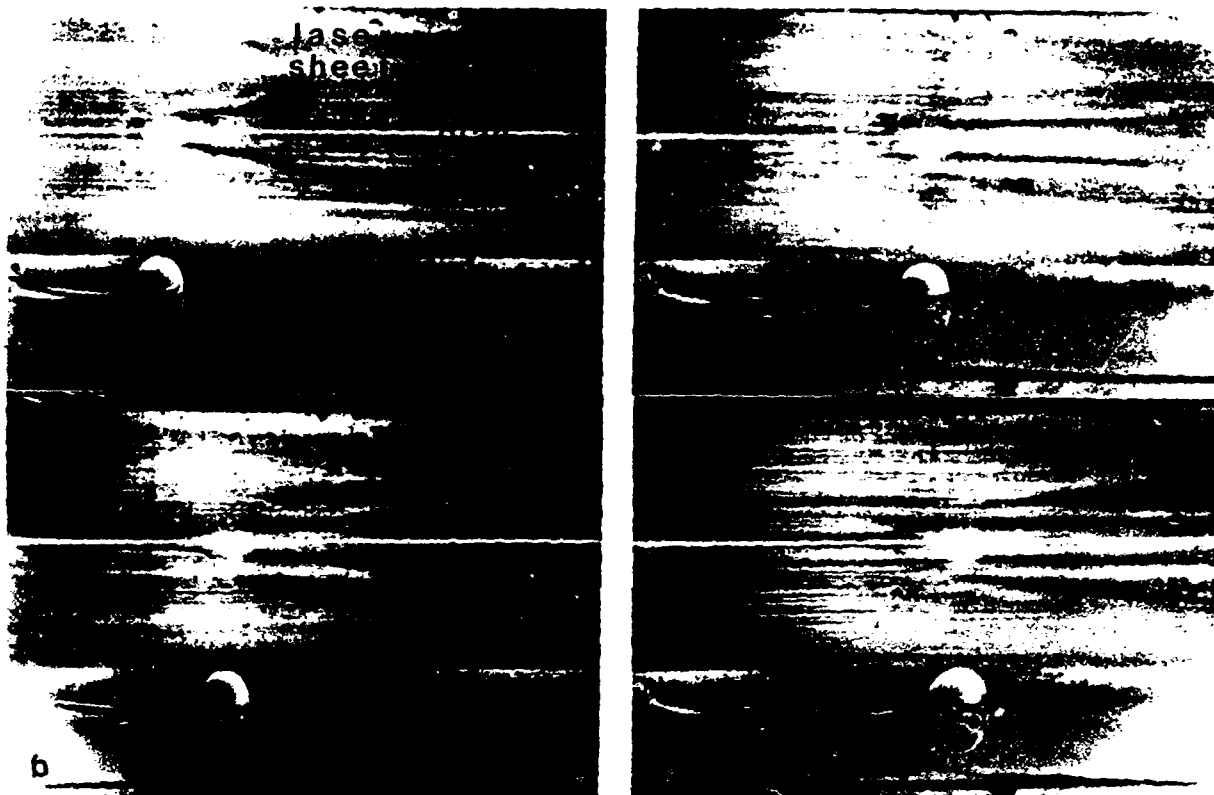


Fig. 3.11 Four photos of the evolution for  $\delta/D > .15$ . In this case a pocket does not form, and it appears that the hairpin has been generated by the initial vortex ring/wall interaction.



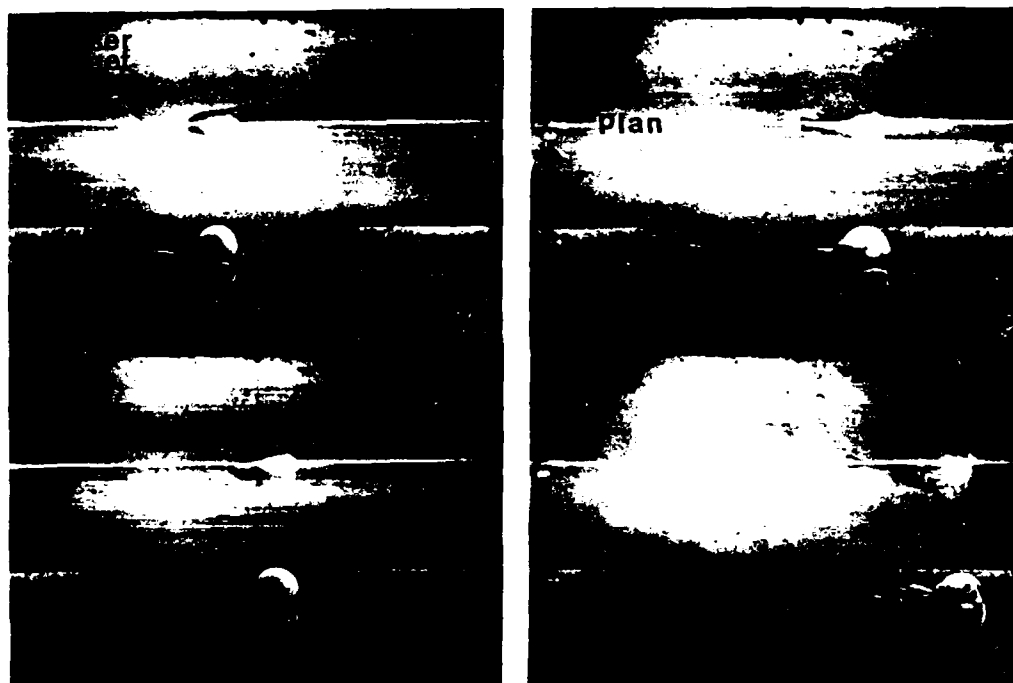


Fig. 3.12 Four photos of the interaction for  $\delta/D < .15$ . In this case pinch-off of a portion of the lifted hairpin does occur, creating a new small vortex ring.

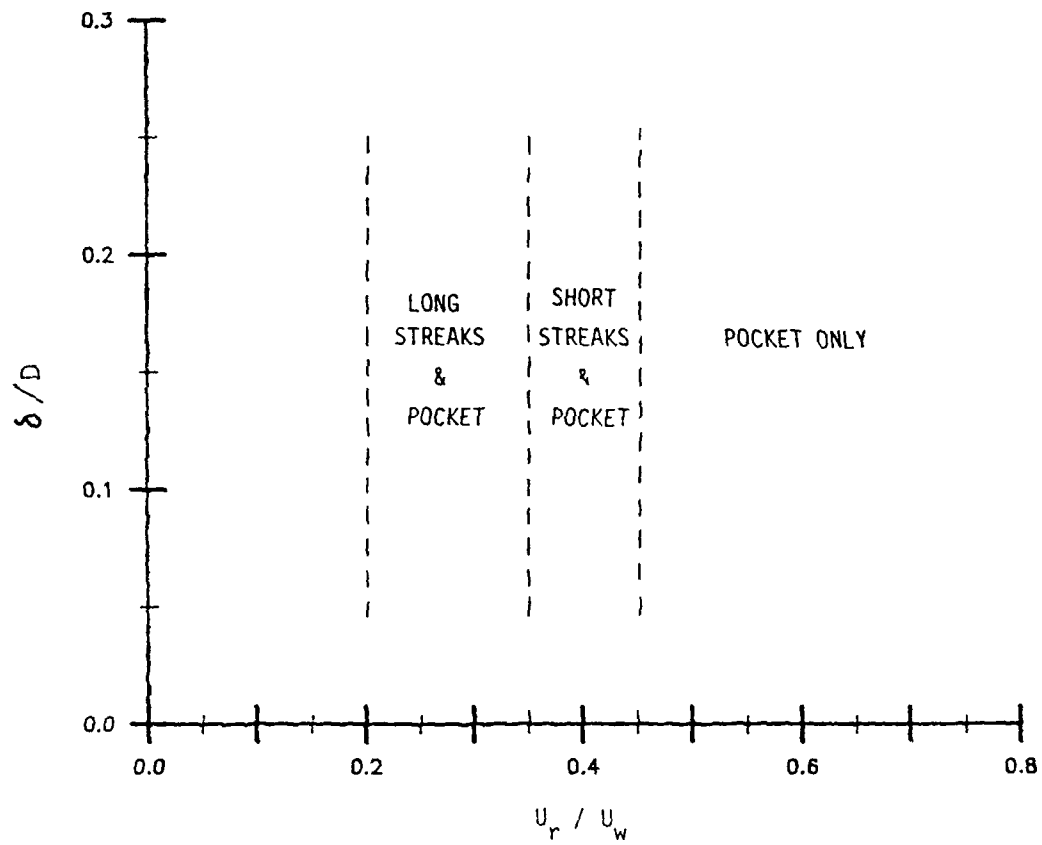


Fig. 3.13 The dependence of the formations and evolutions of streaks on  $\delta/D$  and  $U_r/U_w$  for  $D^+ > 250$  and a 3 degree incidence angle. The indicated boundaries between different evolutions are approximate.

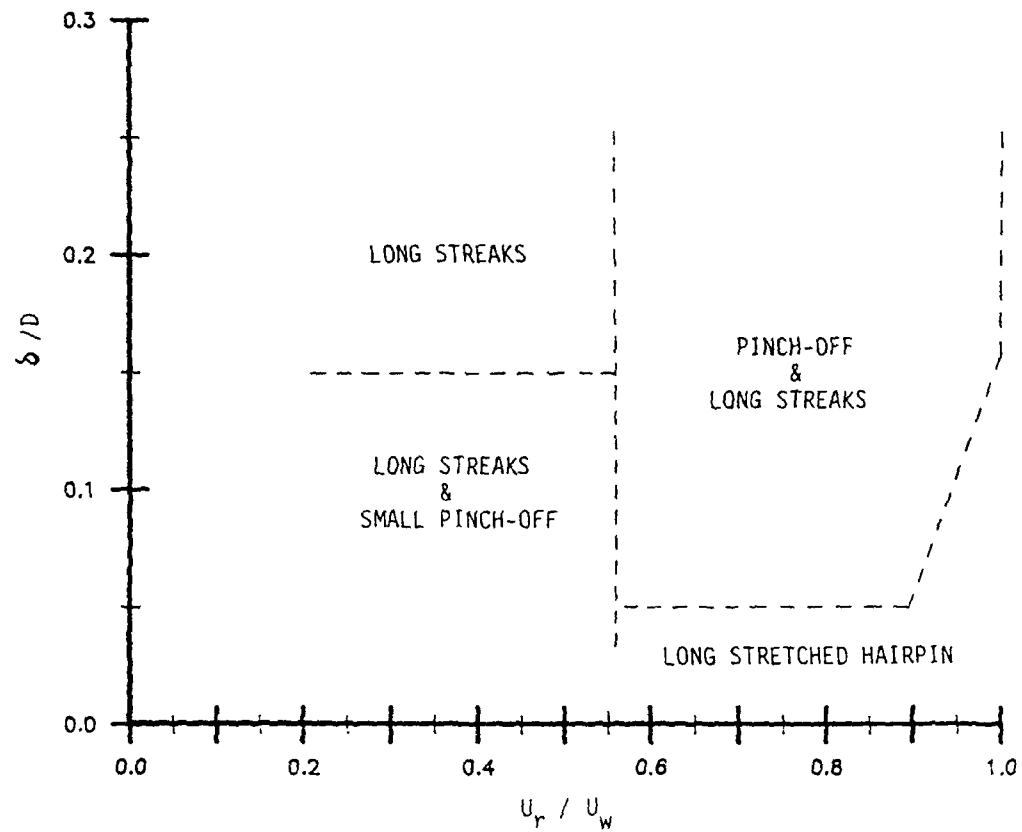


Fig. 3.14 The dependence of  $\delta/D$  on  $U_r/U_w$  for rings moving away from the wall at 2.5 degrees.  $\delta/D$  now plays a much more important role, and long streaks are generated over the entire speed ratio range studied.

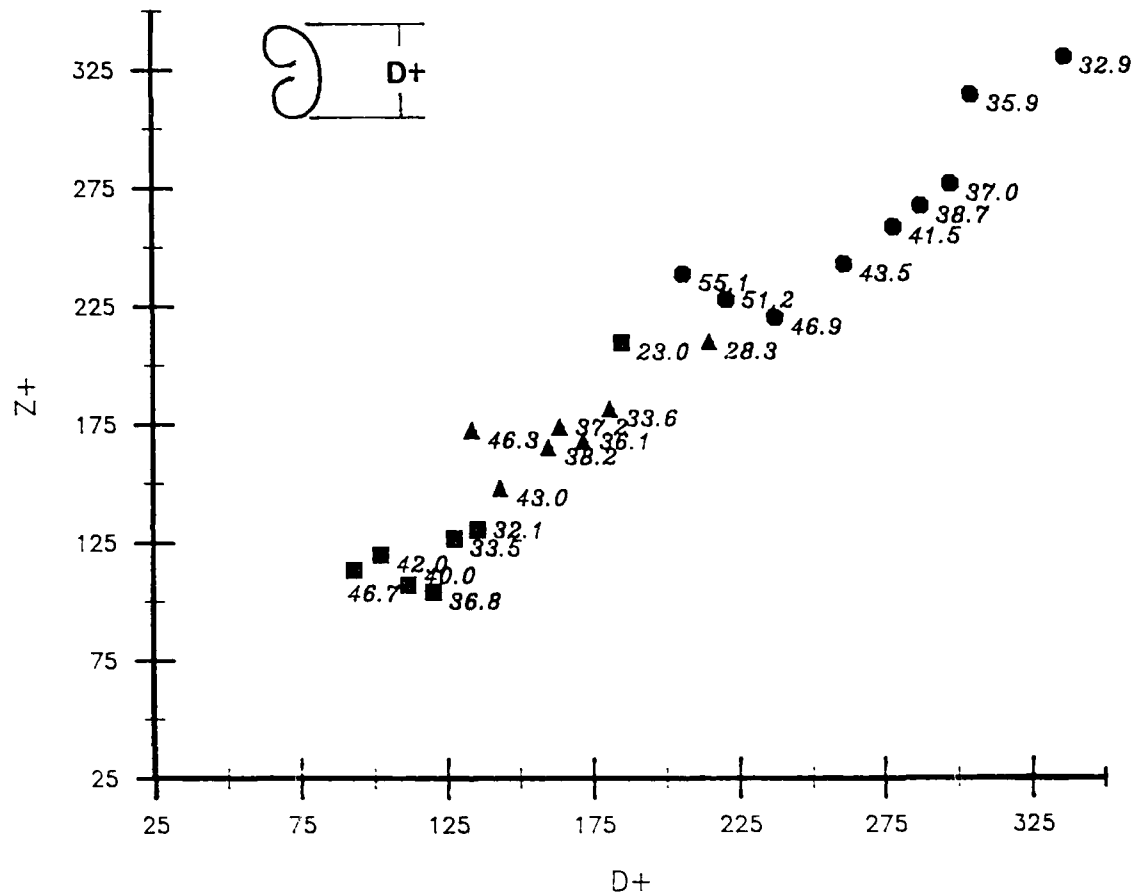


Fig. 3.15 The dependence of the streak spacing in wall units on the size of the vortex ring in wall units, for an incidence angle of 3 degrees and  $U_r/U_w = .31$ . The thickness of the wall layer (in wall units) is shown next to each data point.

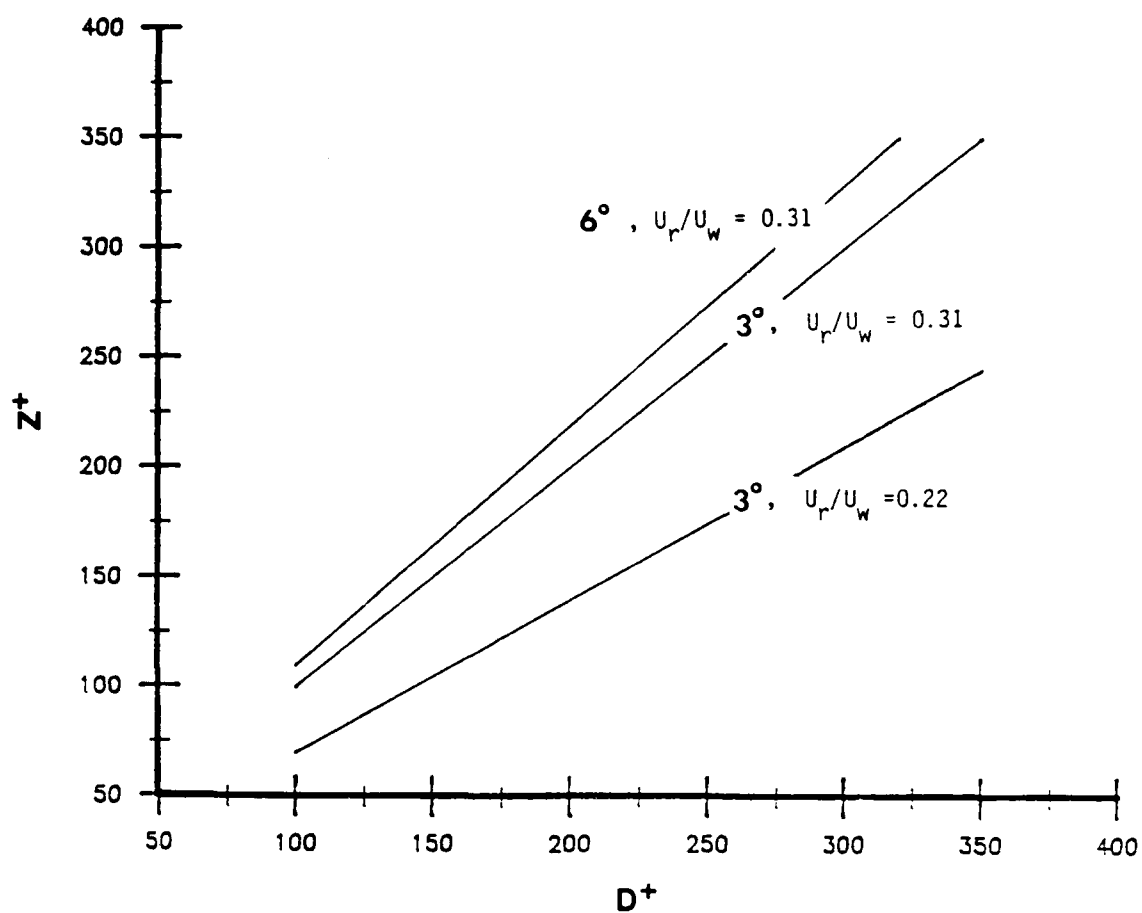


Fig. 3.16 The dependence of the streak spacing on the speed ratio and angle.

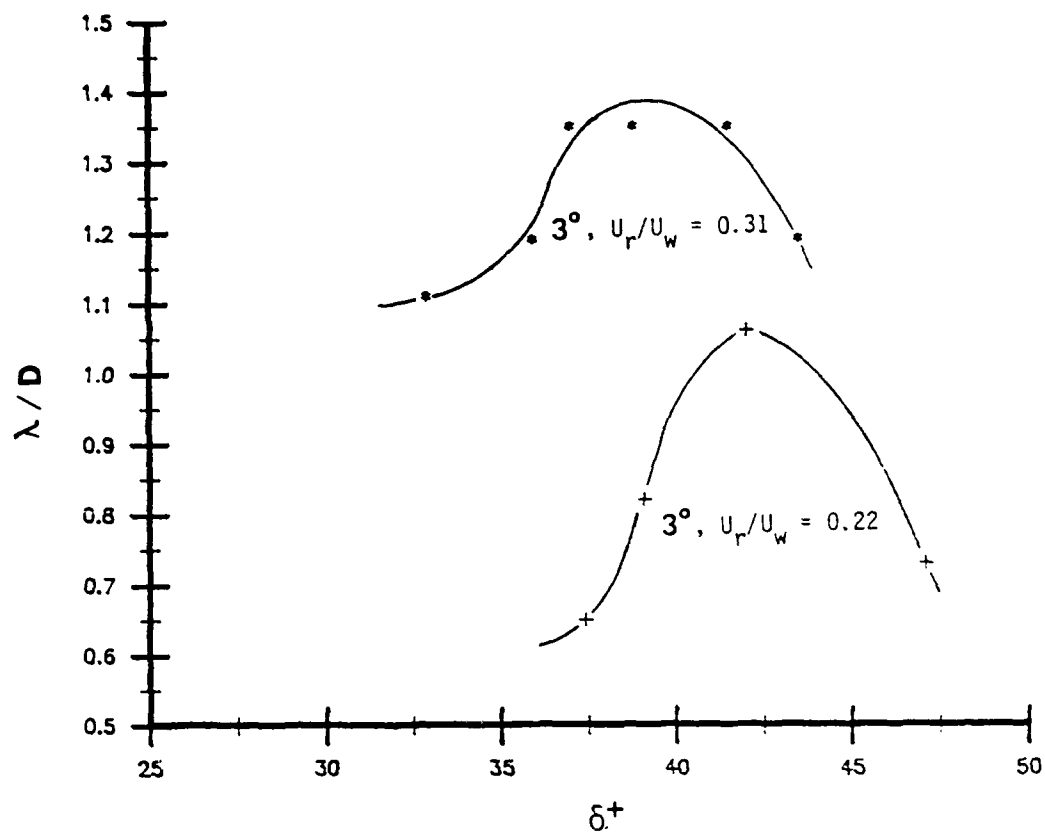


Fig. 3.17 The non-dimensionalized streamwise wavelength that sets in as a function of  $\delta^+$  for different  $U_r/U_w$  and angles.

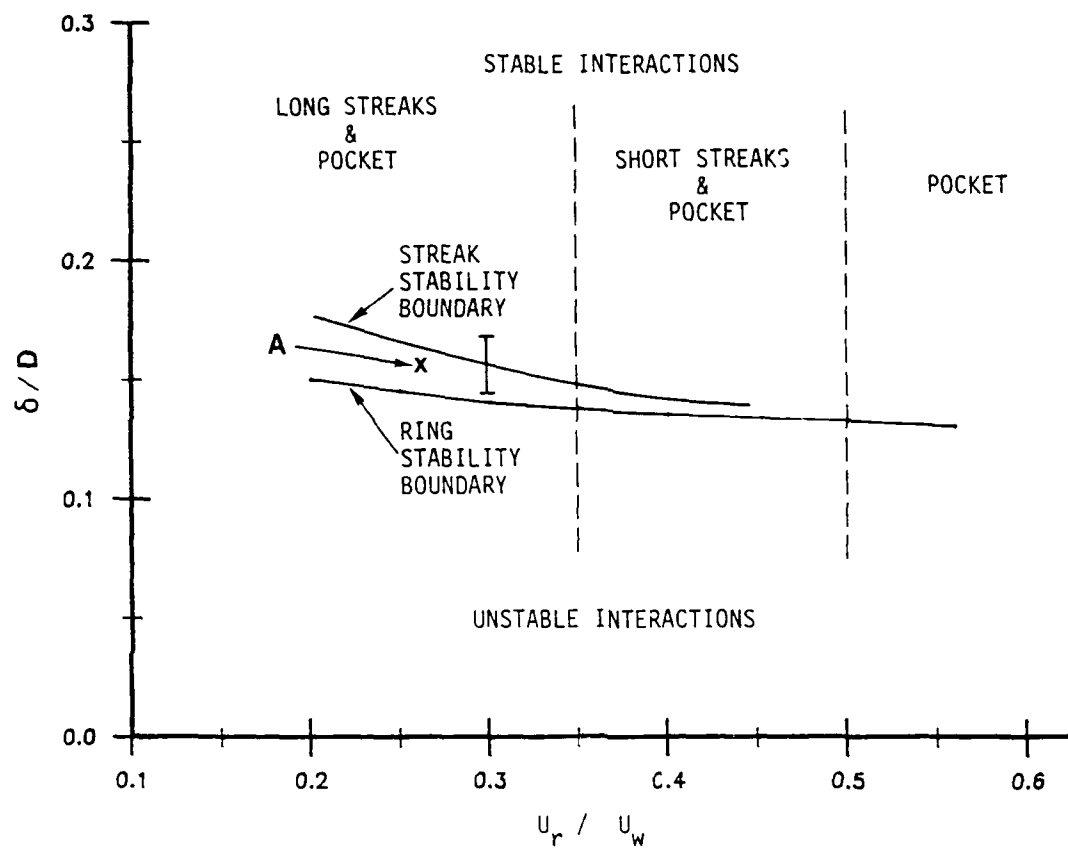


Fig. 3.18 A comparison between ring and streak stability the of a three degree ring moving towards the wall.

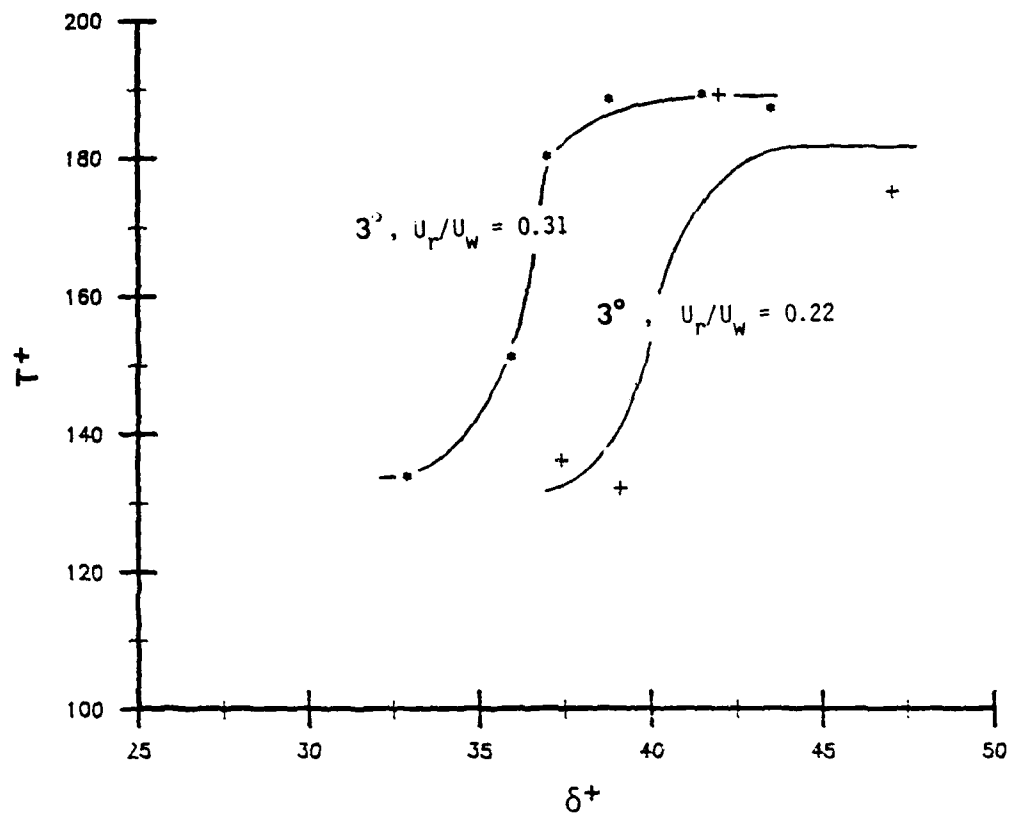
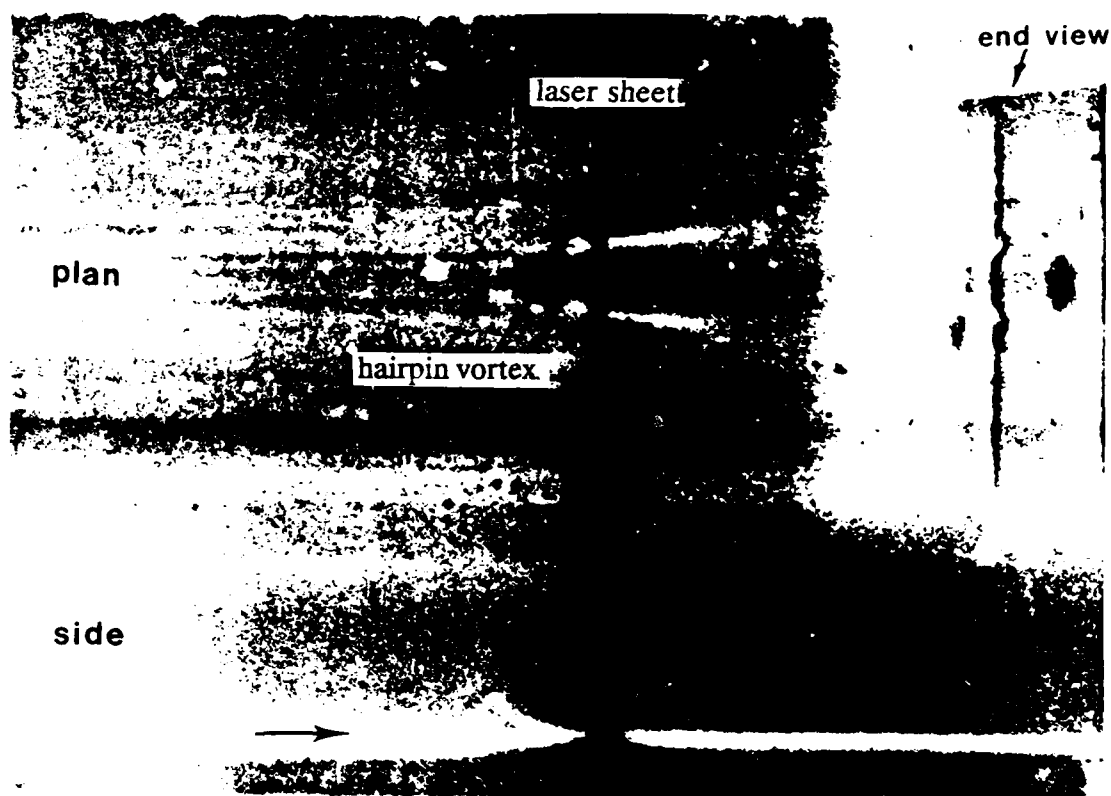
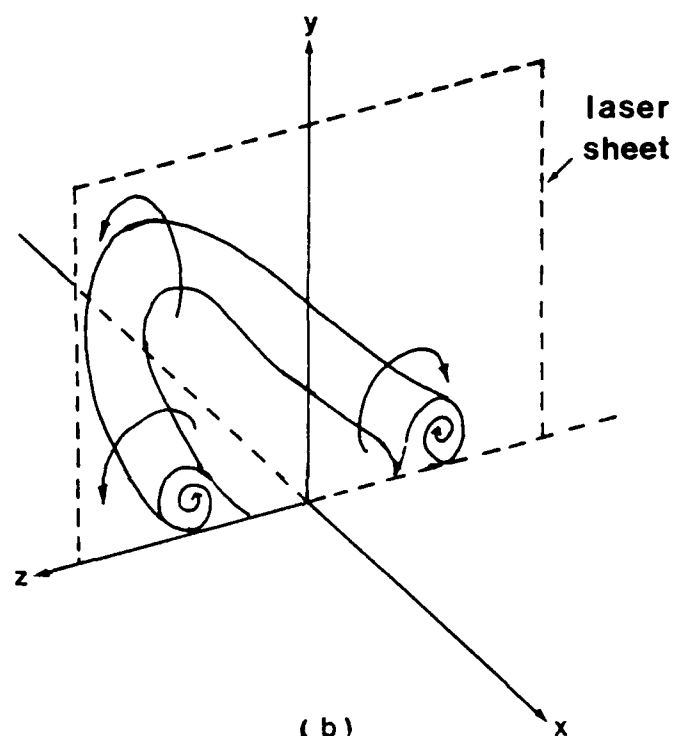


Fig. 3.19 The dependence of the time to instability of the streaks on the wall layer thickness (both quantities are non-dimensionalized by wall layer variables) for three degree incidence rings.





(a)



(b)

Fig. 3.20 (a) A photo of a hairpin vortex in three-view flow visualization;  
 (b) A sketch of the vortical motion of the hairpin vortex;  
 note that the arrows indicate the sign of rotation

end view

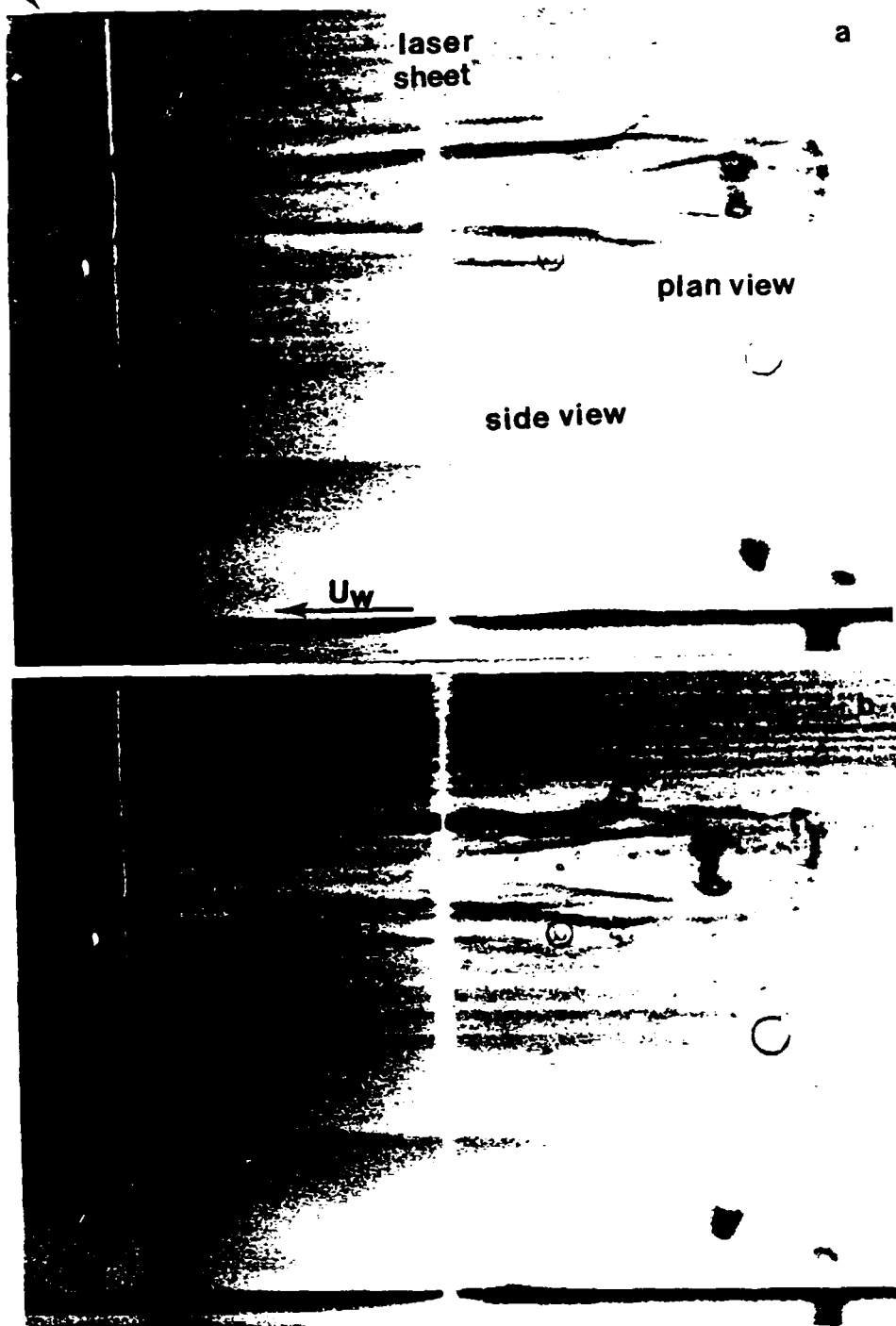


Fig. 3.21 Four photos of the three-view visualization; each photo is  $10 t^+$  apart.

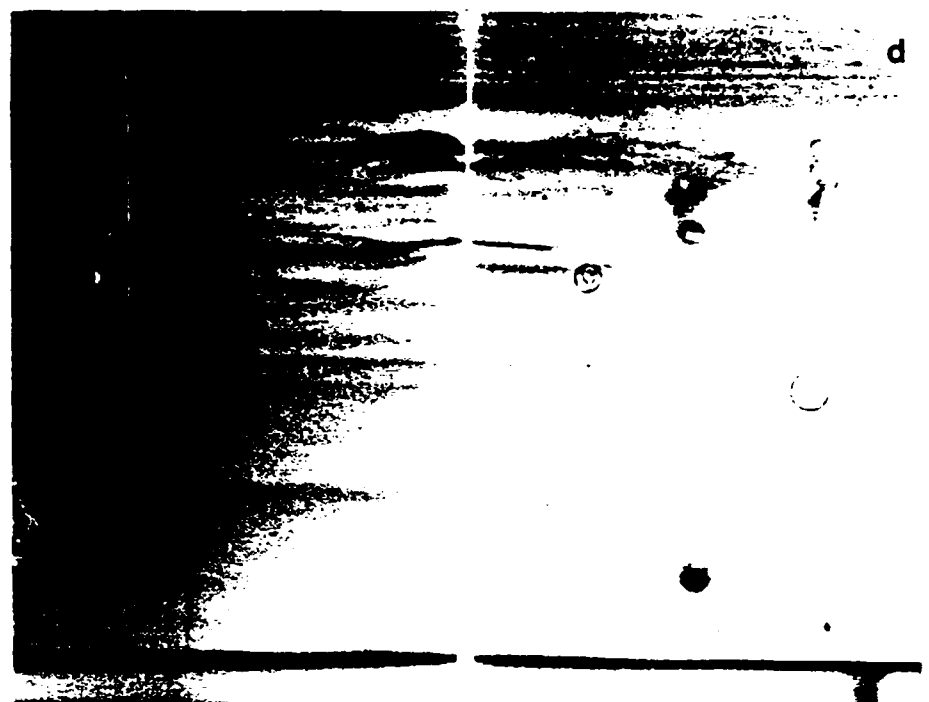
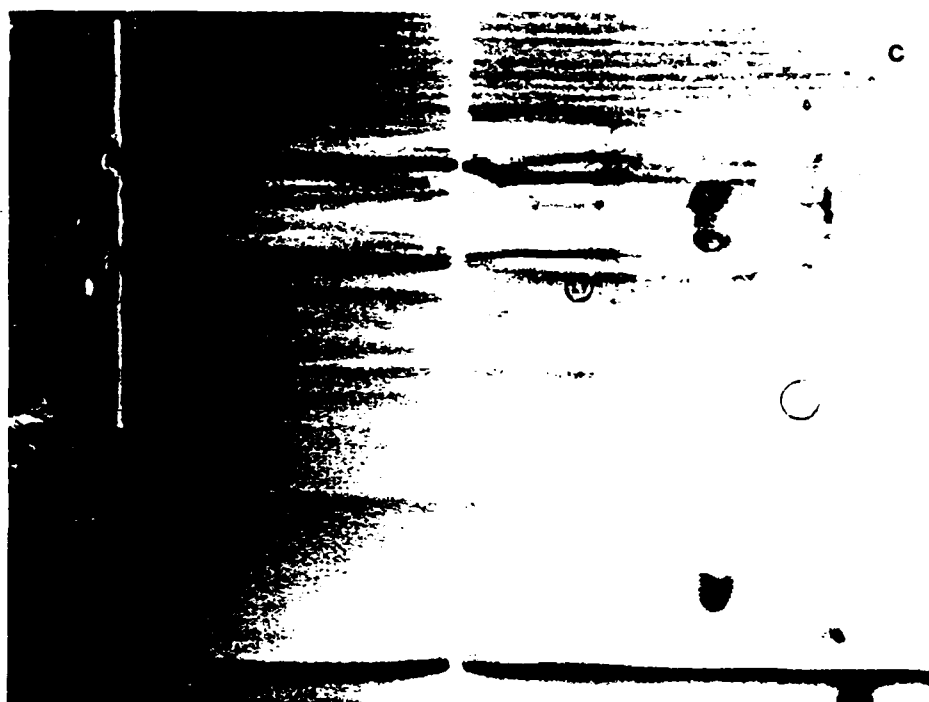


Fig. 3.21 Cont.

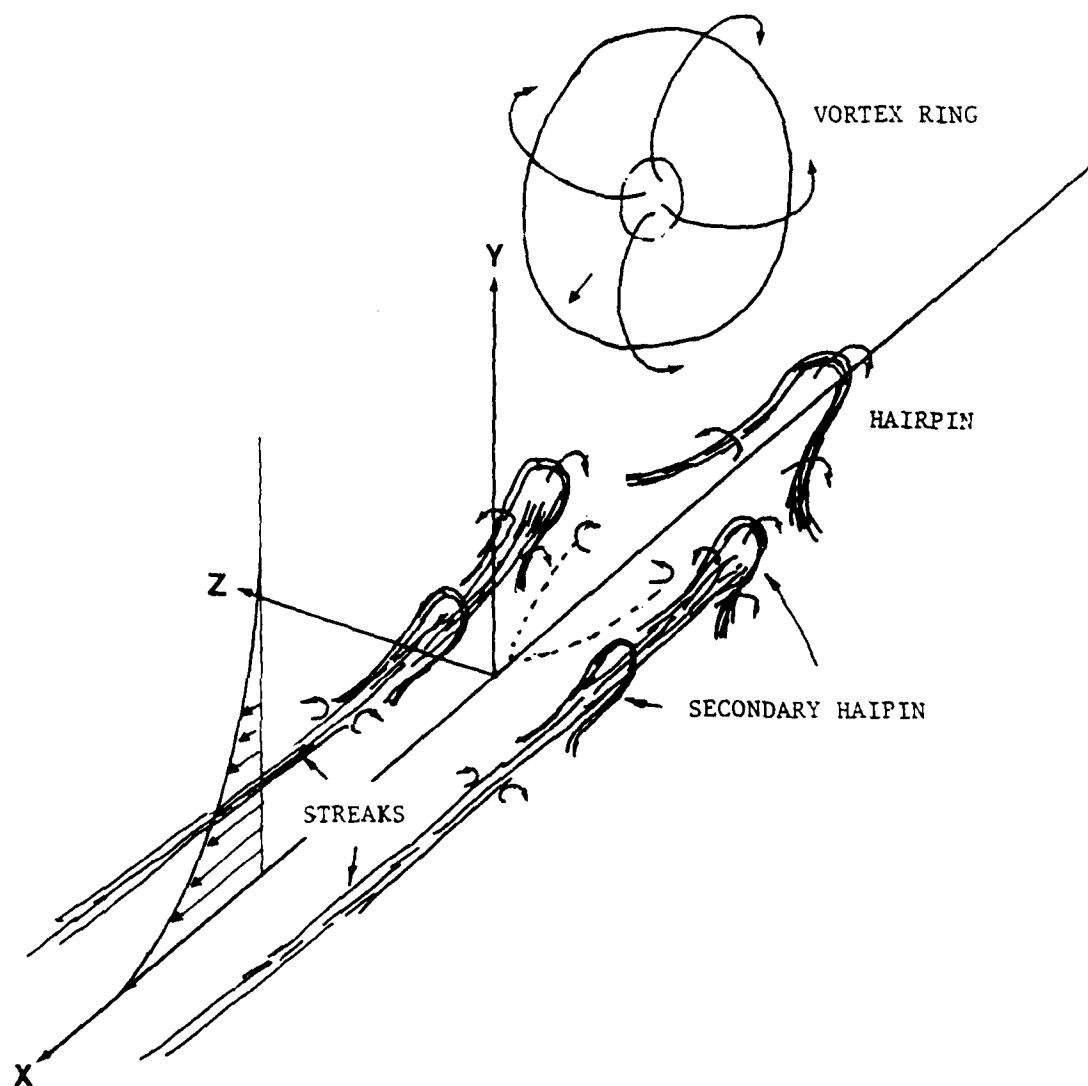
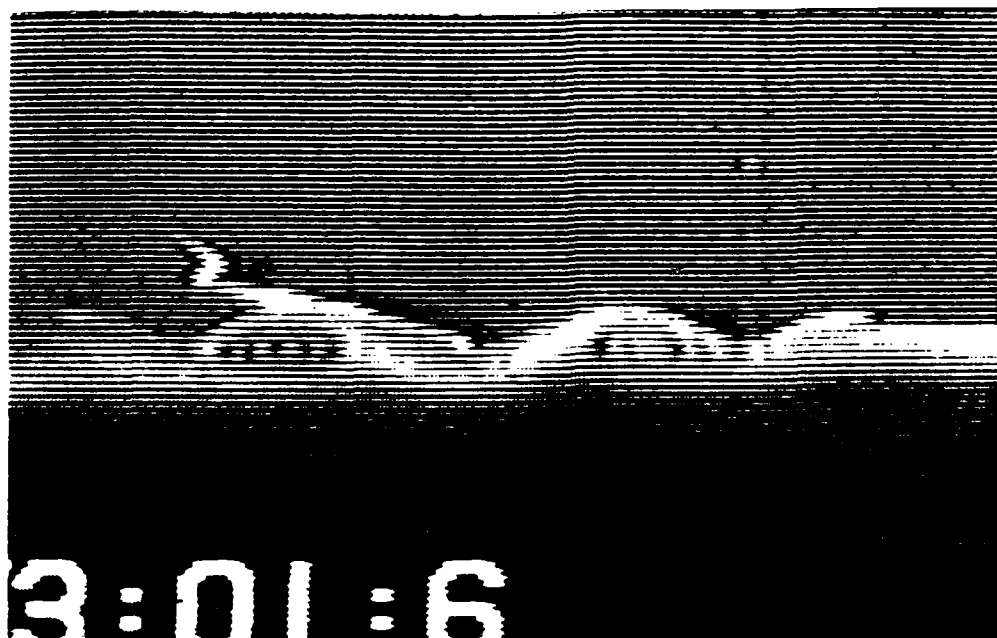
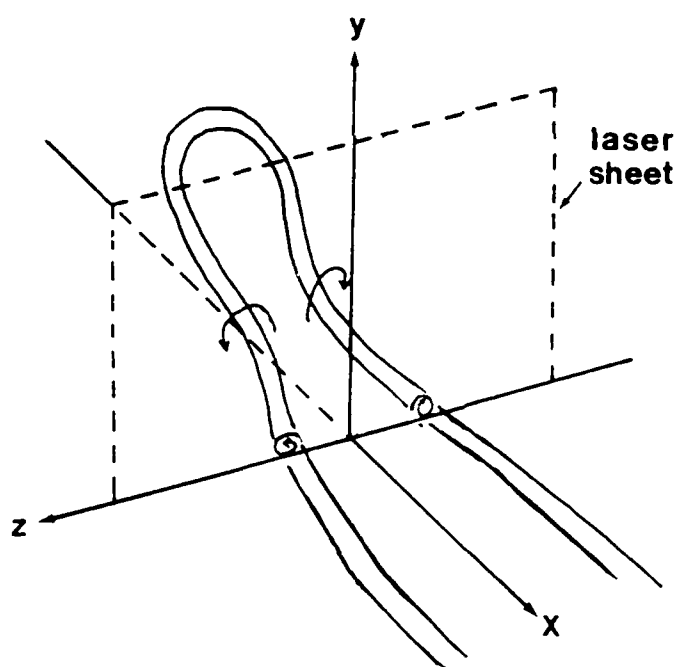


Fig. 3.22 A conceptual picture describing the spatial relationship of the formation of visual features observed in the vortex ring/moving wall interaction including the main hairpin vortex, secondary hairpin vortices, long streaks, and pocket; the arrows indicate the local flow direction.



a



b

Fig. 3.23 A photo showing the laser illuminated end view flow visualization for a fast ring moving away from the wall. The observed long streaks were just the legs of the lifted hairpin vortex; they were one unit. The dye marker actually concentrated within the streamwise vortices. The sign of the vorticity shown in Fig. 4.23 (b) is consistent with that associated with the hairpin vortex shown in Fig. 4.20 (b).

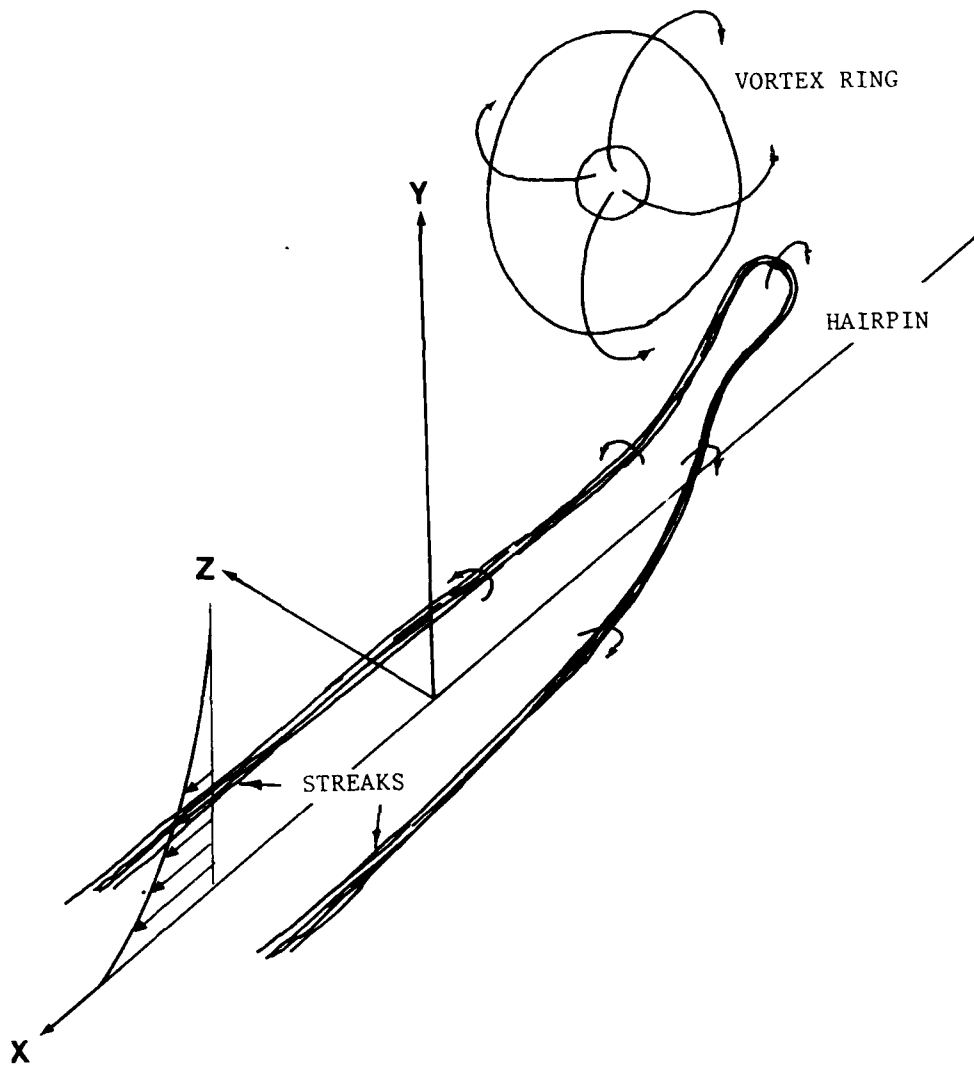


Fig. 3.24 The conceptual picture summarizing the spatial evolution of the vortex ring/moving wall interaction for  $U_r/U_w > 0.6$  when the vortex ring moves away from the wall.

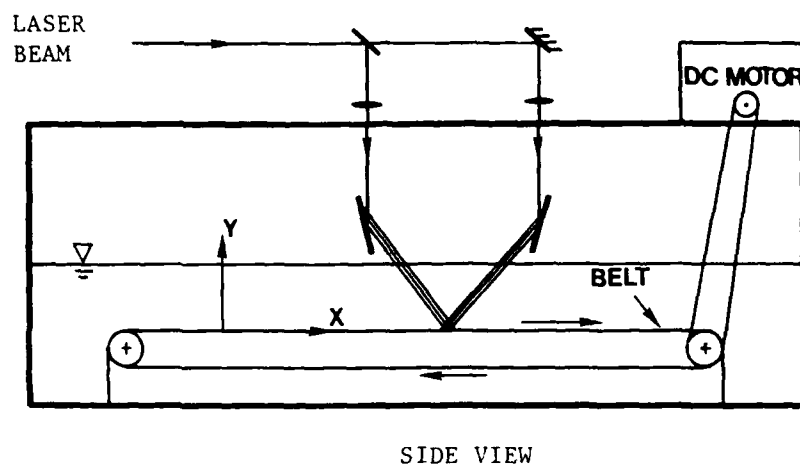


Fig. 4.1 A schematic of experimental apparatus of the Stokes' layer measurement; the moving belt system is similar to what was used in water tank.

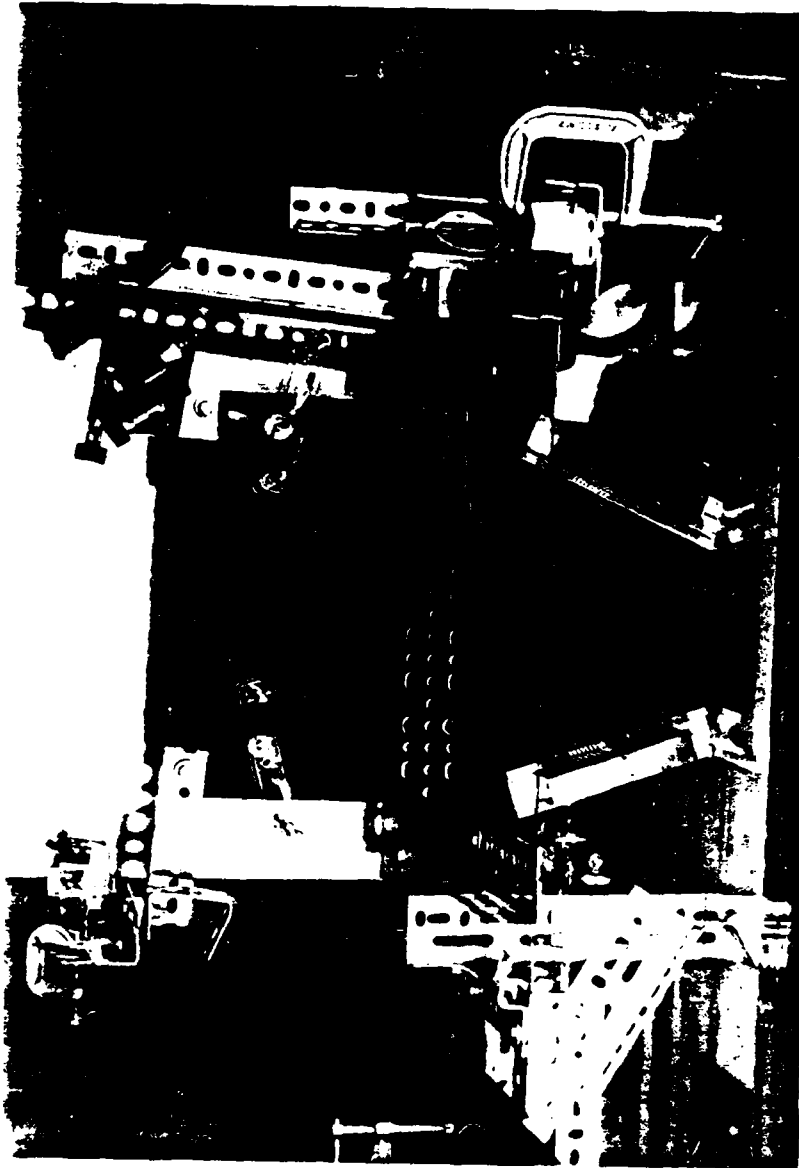


Fig. 4.2 The optical configuration for generating the photochromic grid.



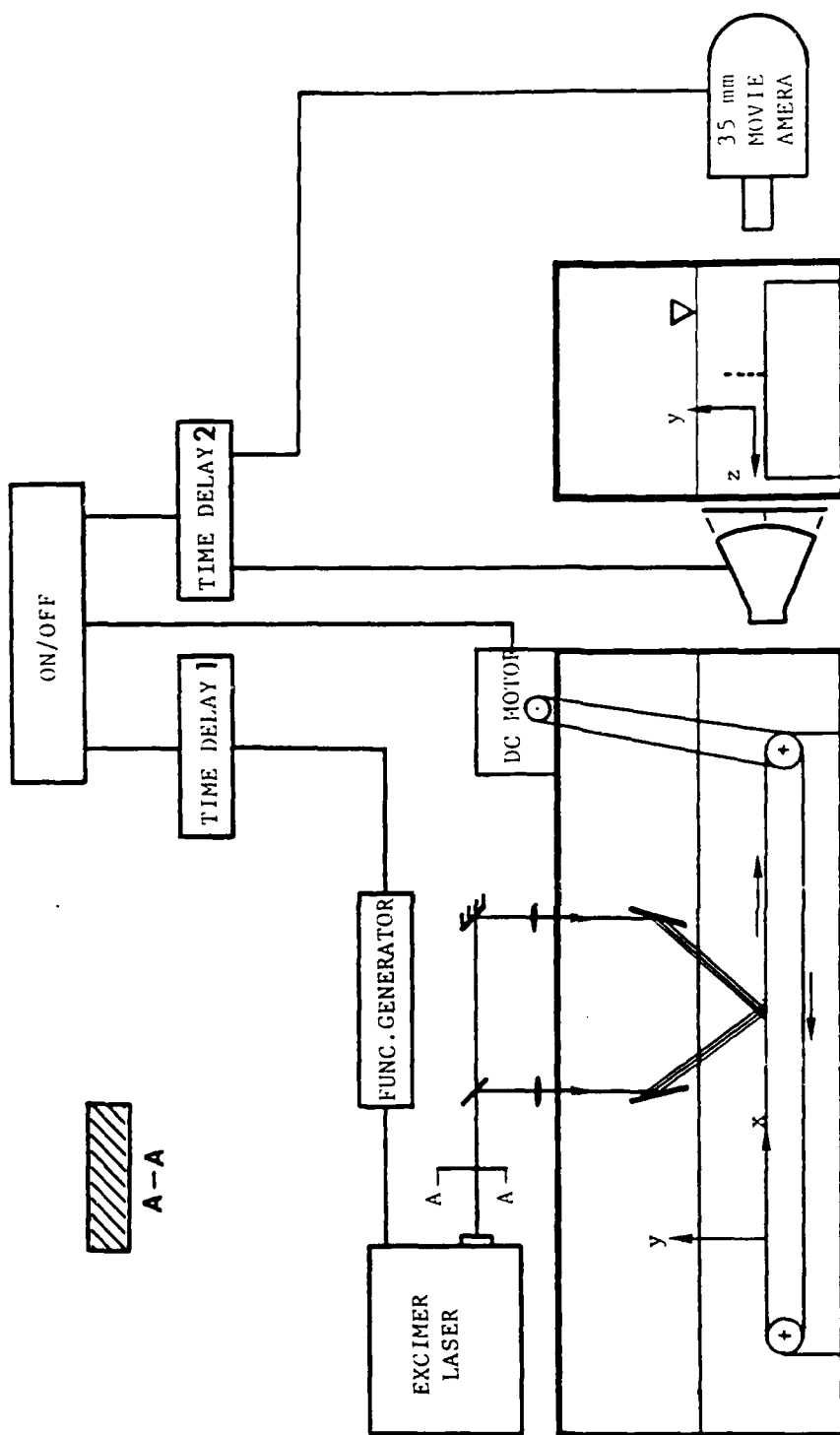


Fig. 4.3 The flow chart of the control system of the Stokes' layer measurement. The best orientation of the incident laser beam is also shown in this figure.

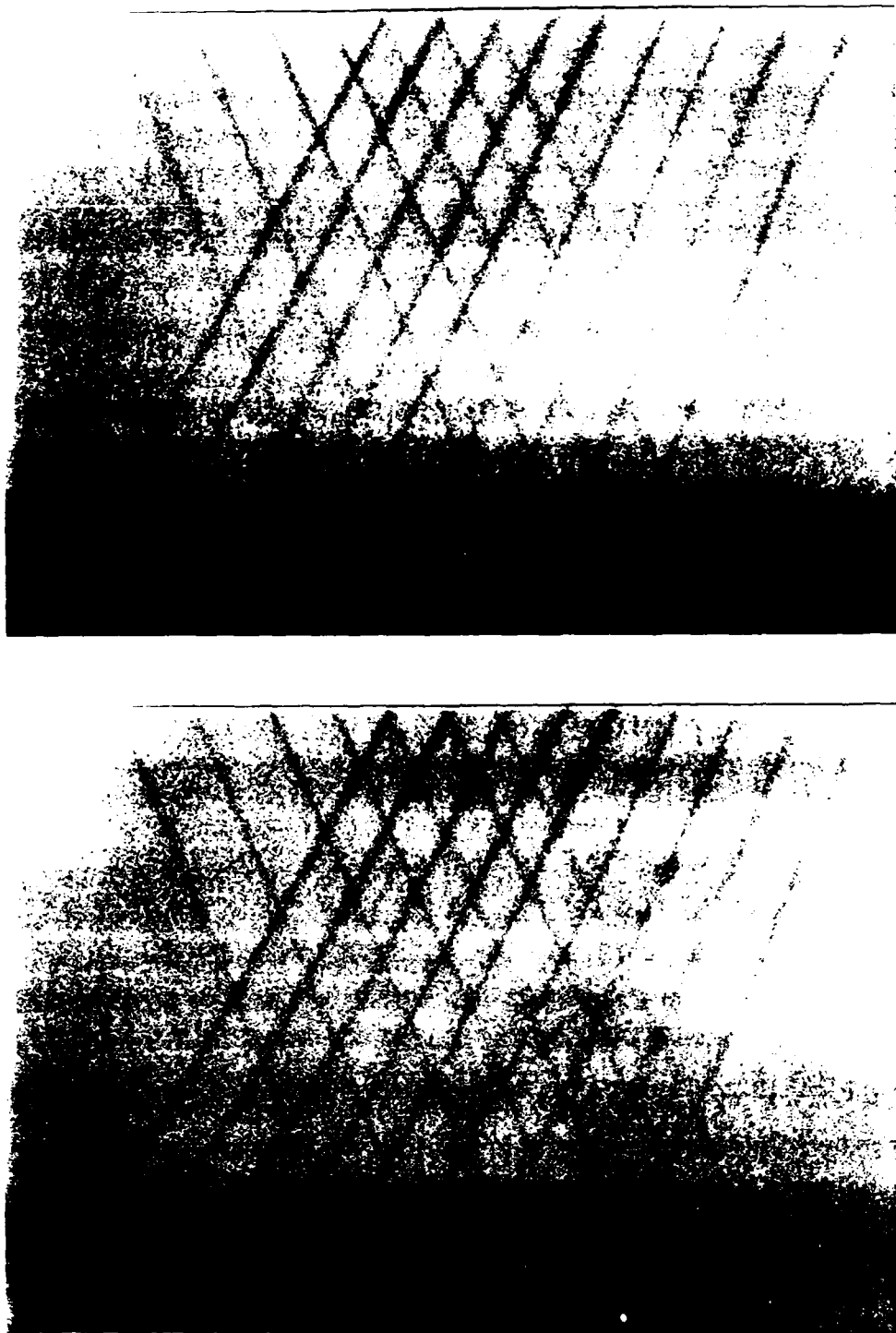


Fig. 4.4 Two photos from the result which are 0.05 second apart; these photos were taken for  $U_w = 12.7$  cm/sec and belt running time  $t = 5.25$  seconds; the belt moved from right to left.

# STOKES' LAYER VELO. DISTR.

U0 : •, .. 0.417 fps; +.. 0.494 fps. t=5.25 sec. layusp

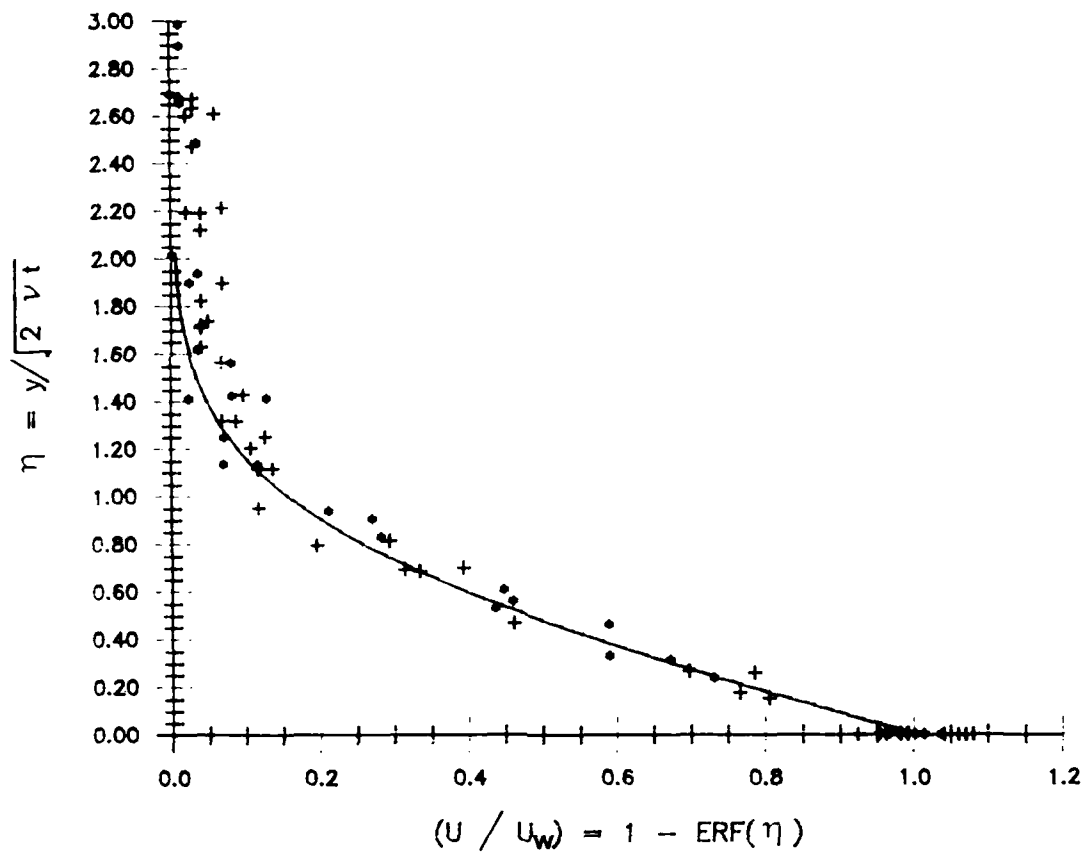


Fig. 4.5 The nondimensionalized velocity profile for two belt running speeds where the solid line represents the exact solution.

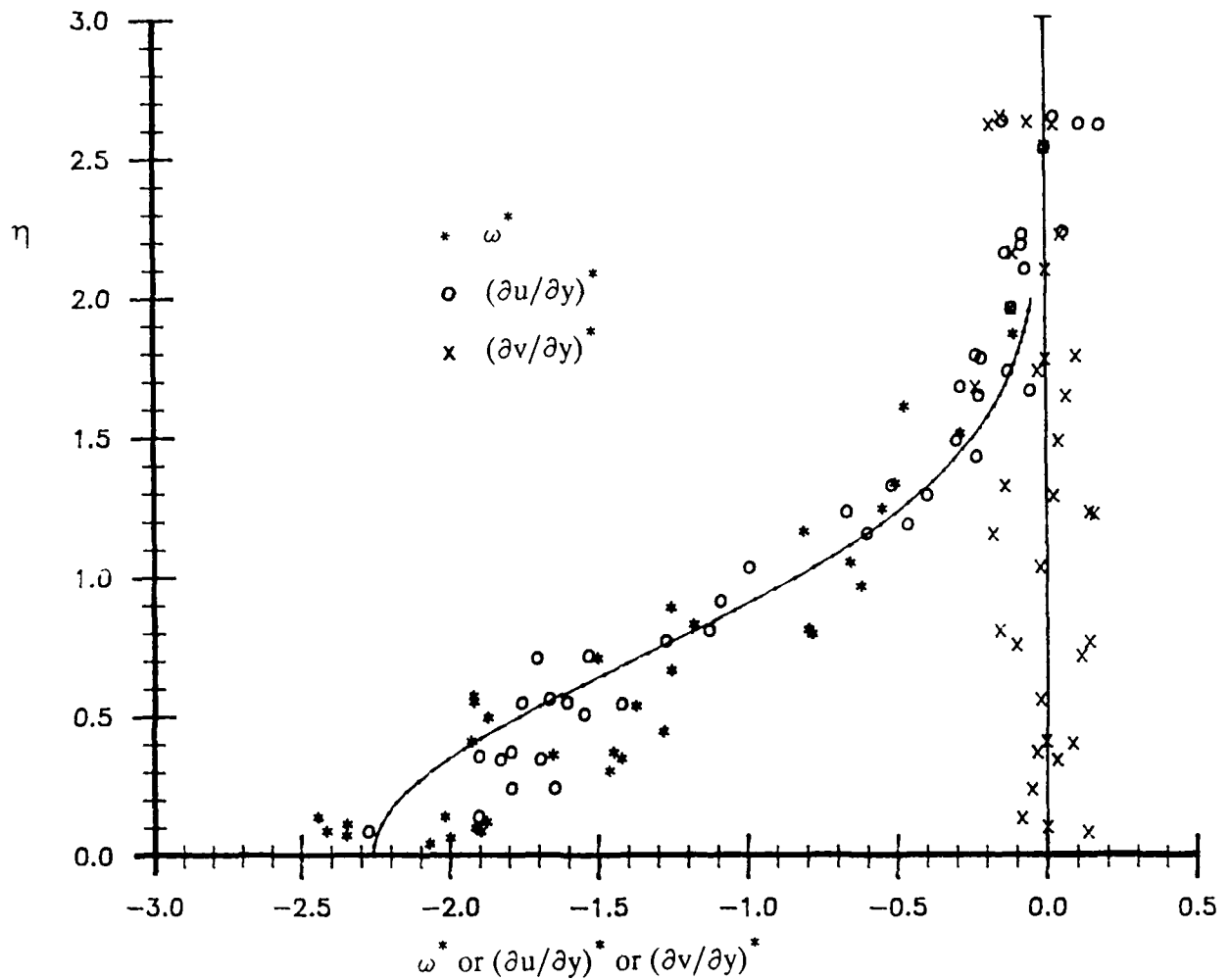


Fig. 4.6 Results of the velocity gradient  $\partial u / \partial y$  obtained from double differentiation and of the spanwise vorticity obtained from circulation approach are shown in this figure where they are compared with the exact solution (represented by solid line). Everything is nondimensionalized by the similarity variables of the exact solution. A check of continuity equation is also shown in this figure.

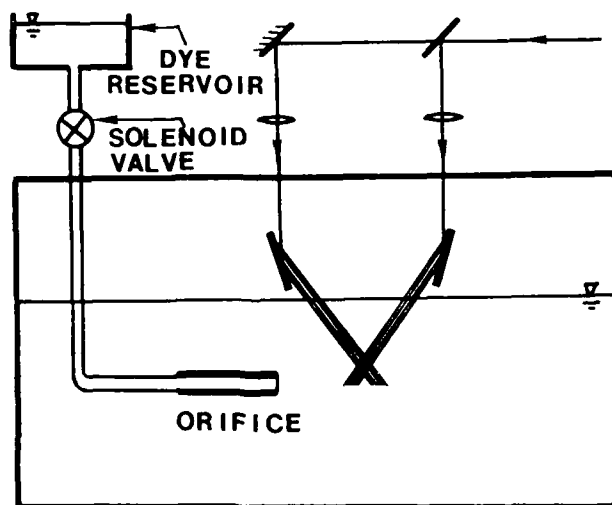


Fig. 4.7 A schematic of the experimental configuration used to generate and measure the vortex ring.

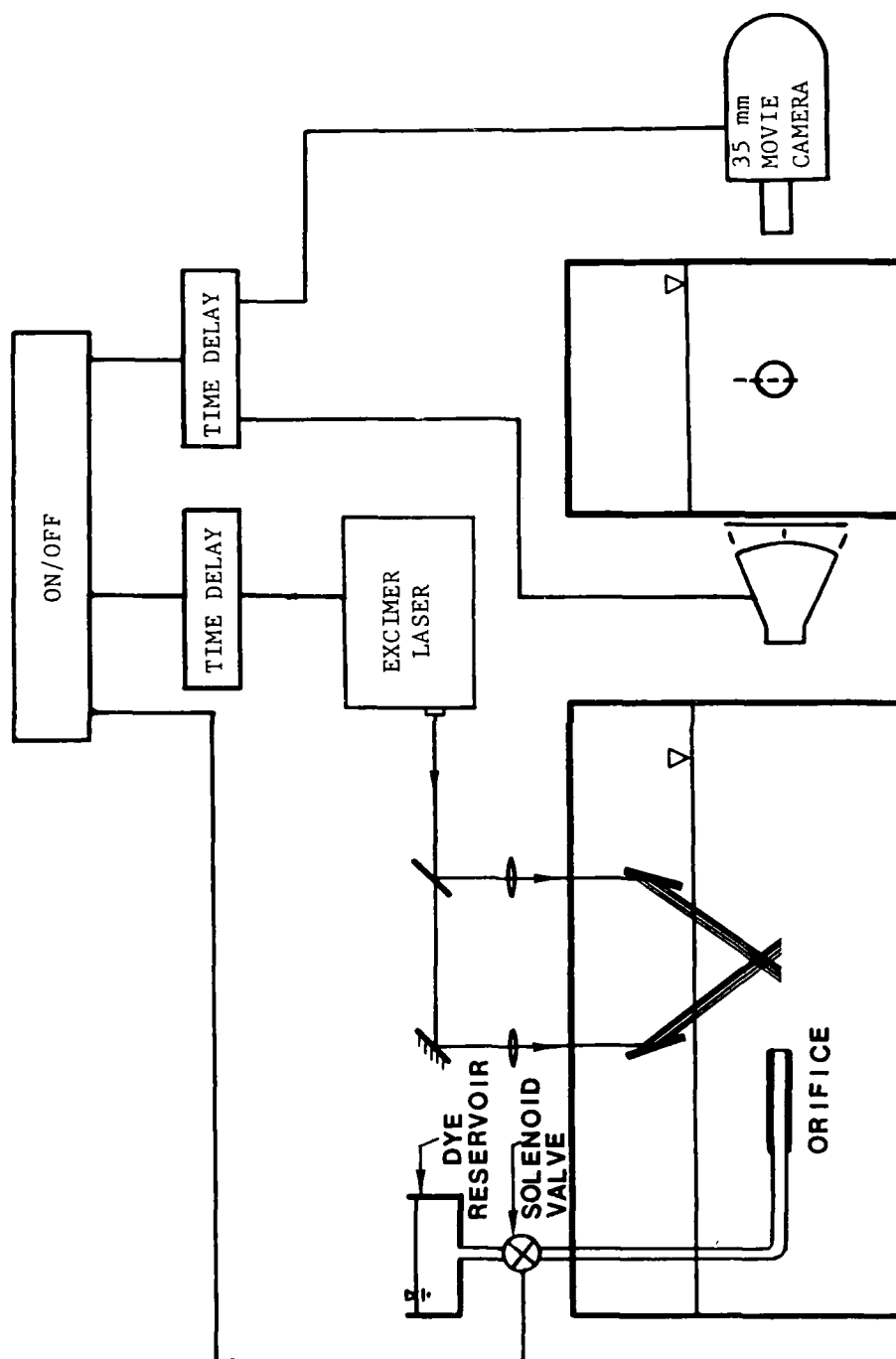


Fig. 4.8 The flow chart of the control system for vortex ring measurement.

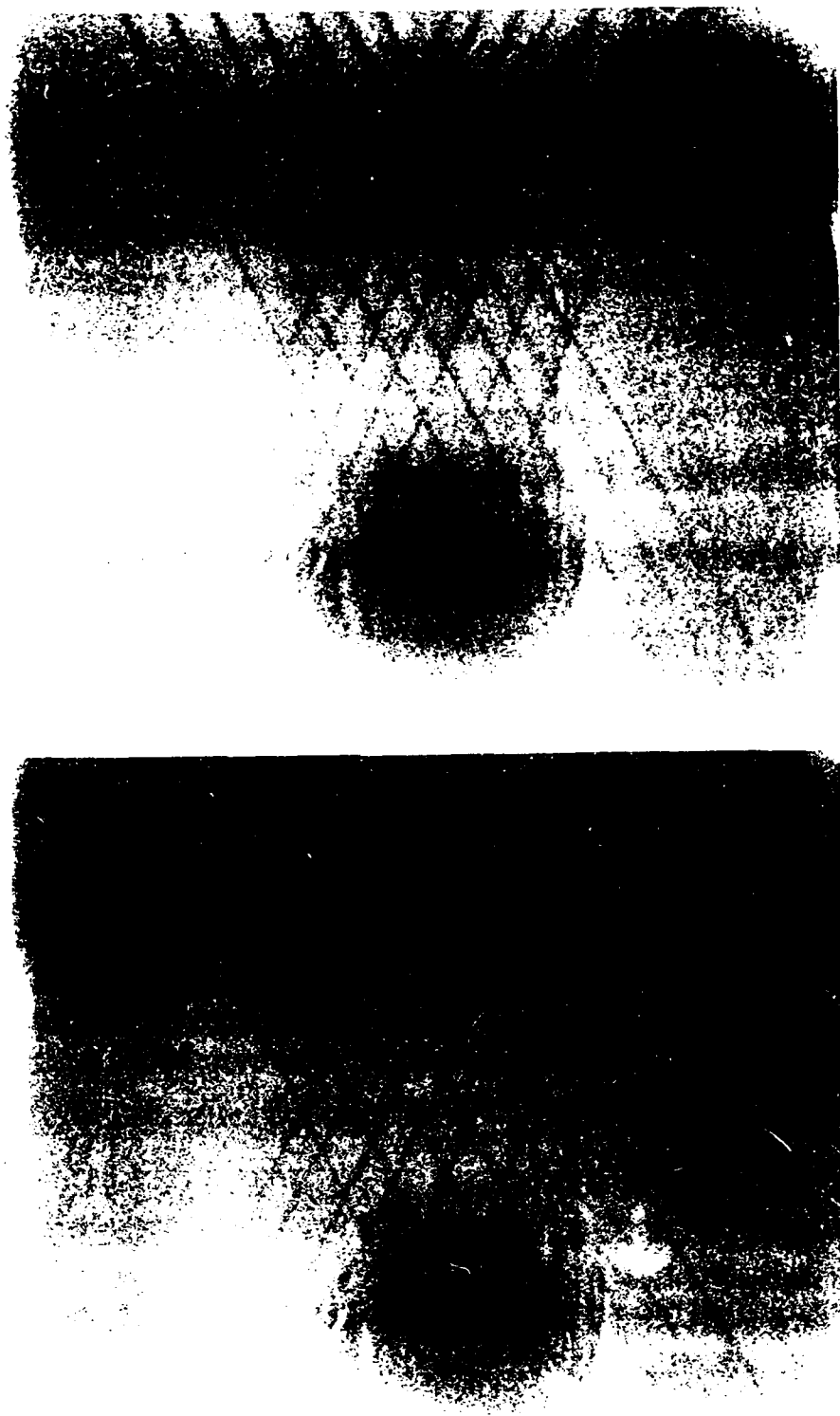


Fig. 4.9 Two photos of the result which are 0.07 second apart

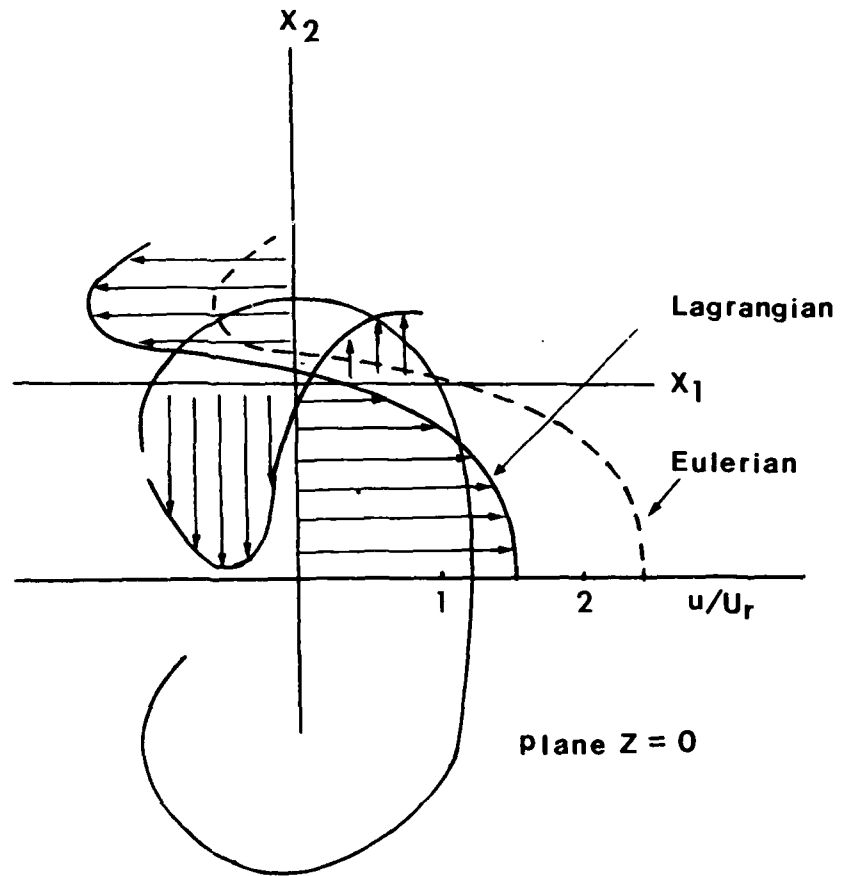


Fig. 4.10 The instantaneous velocities distribution along two axes of the ring.



# CIRCULATION DISTRIBUTION

●..Current measurement ,□.. Hill's, Δ∇..Sullivan et al.

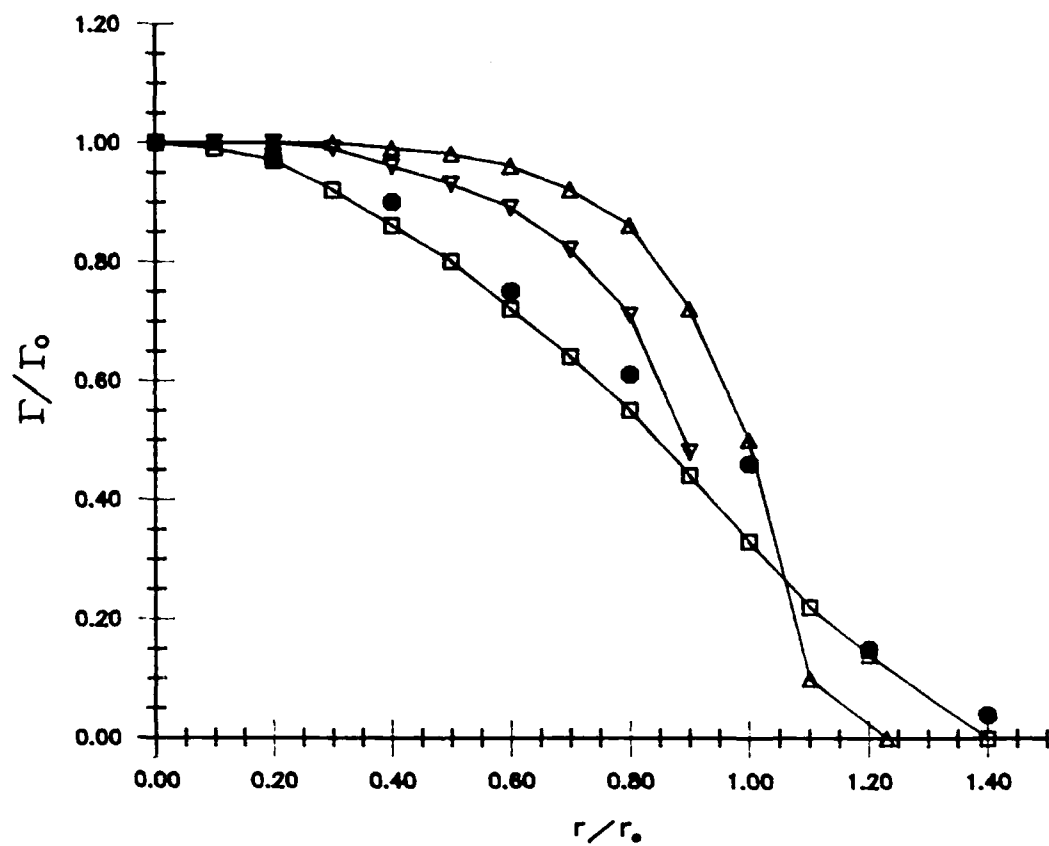


Fig. 4.11 The instantaneous circulation distribution of the ring, which also shows the results obtained by Sullivan et al. (1973) for different Reynolds numbers and shows Hill's exact solution of a spherical vortex.

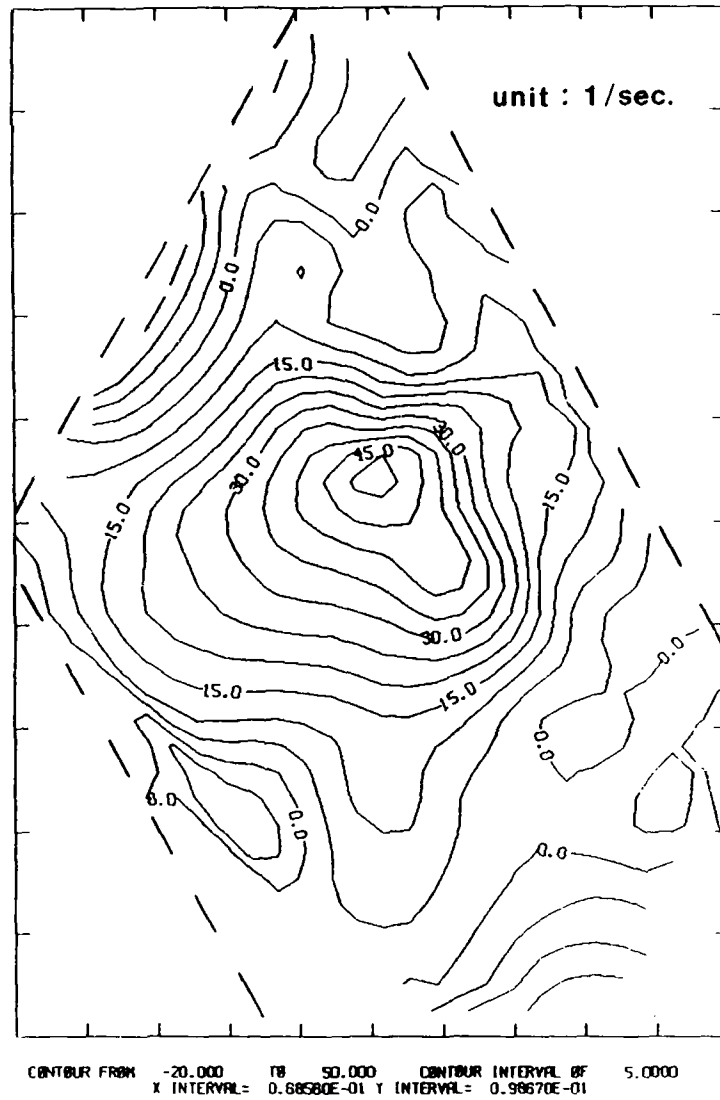


Fig. 4.12 The instantaneous vorticity distribution over a vortex ring.

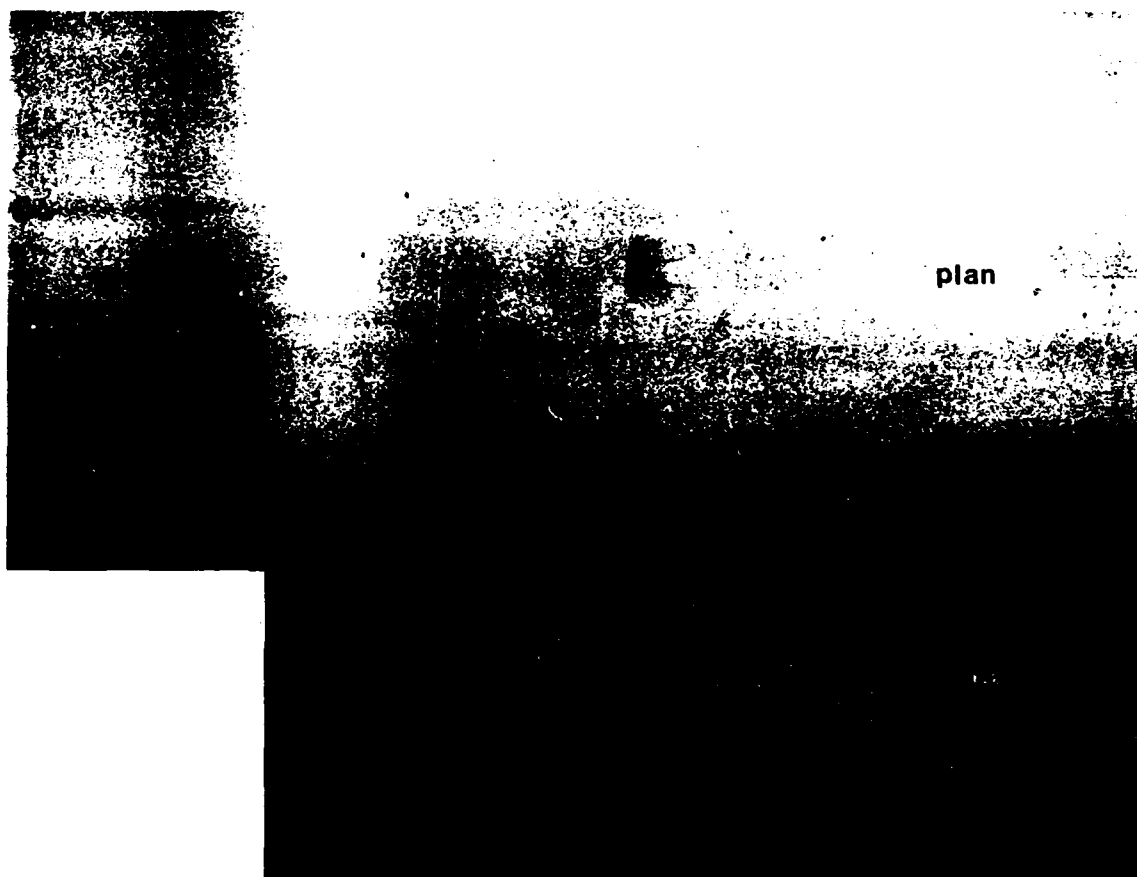


Fig. 4.13 Four sets of photos with both top view and side view describing the time evolution of vortex ring/moving wall interactions in the conditions of  $U_r/U_w = 0.26$ , 3 degree of incident angle,  $\delta/D = 0.18$  and  $U_w = 15.5$  cm/sec.

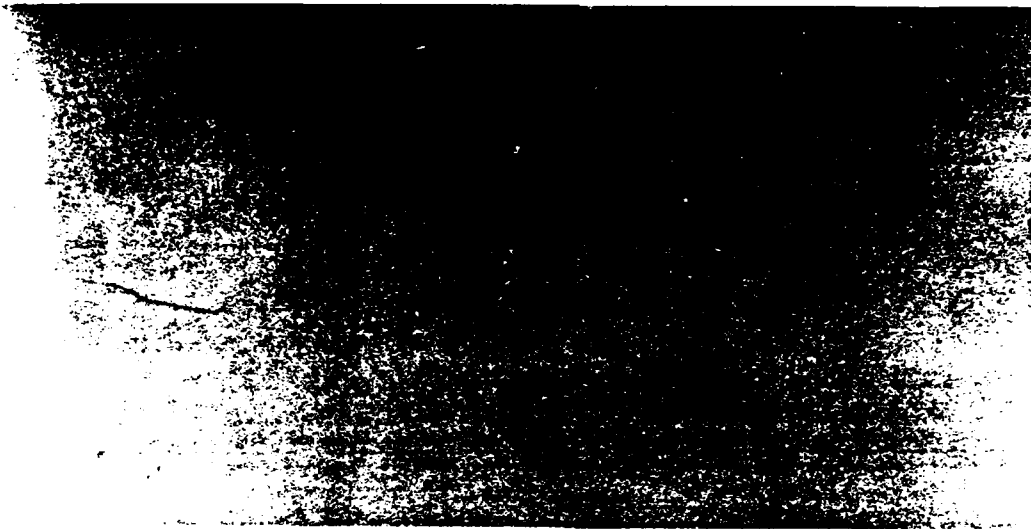


Fig. 4.14 By sending a single photochromic tracer parallel to the moving wall at  $y^+ \approx 16$  we obtained the visual result of the interaction shown in this figure, which is the same as that obtained from the hydrogen bubble technique by many other researchers, such as Kim et al.(1971) and Smith et al.(1983).

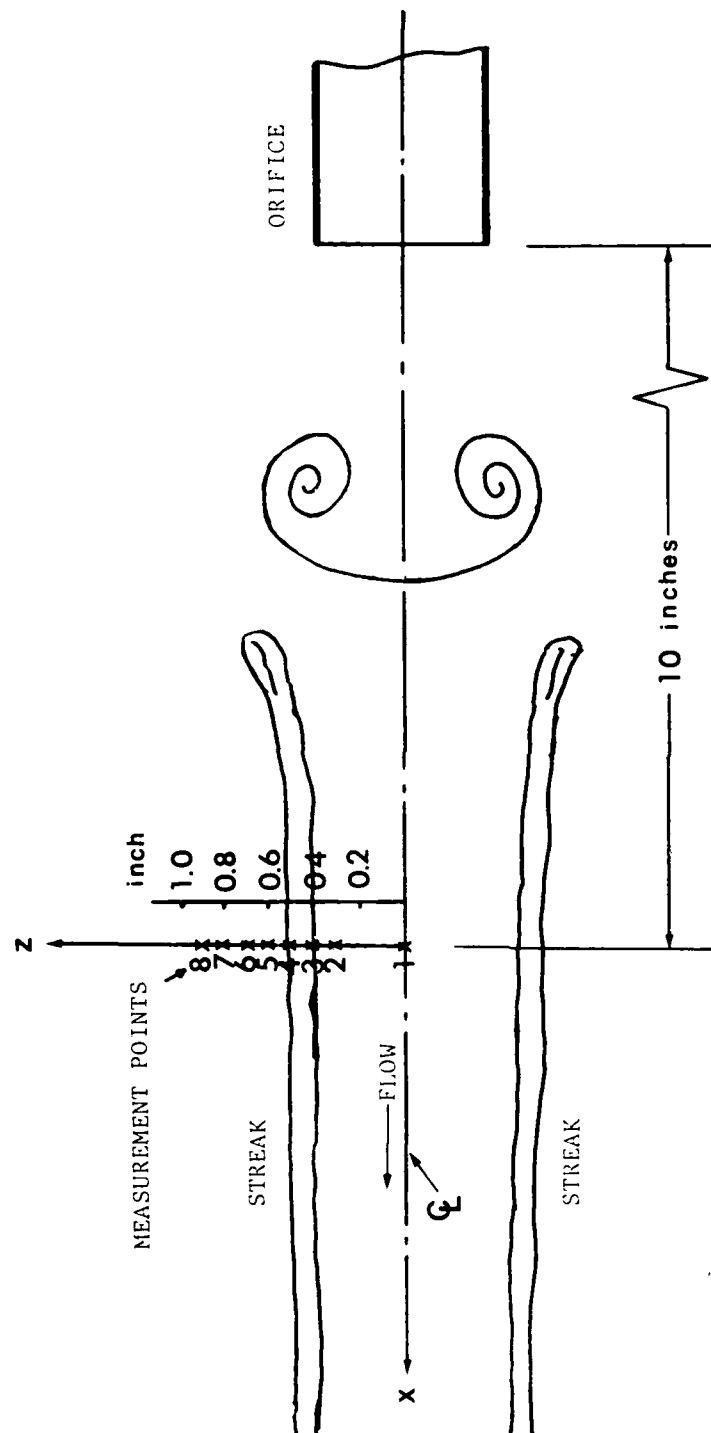


Fig. 4.15 The locations of velocity measurement.

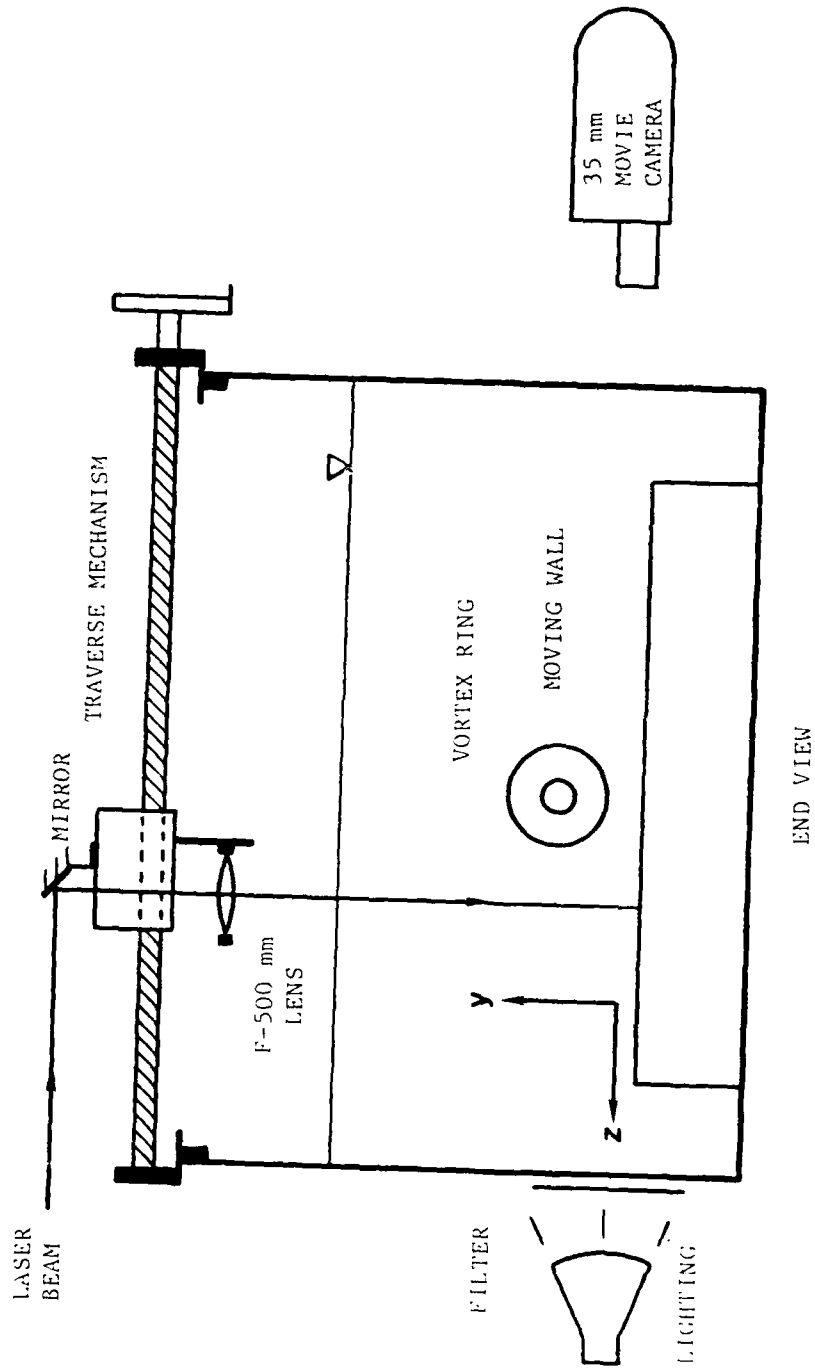
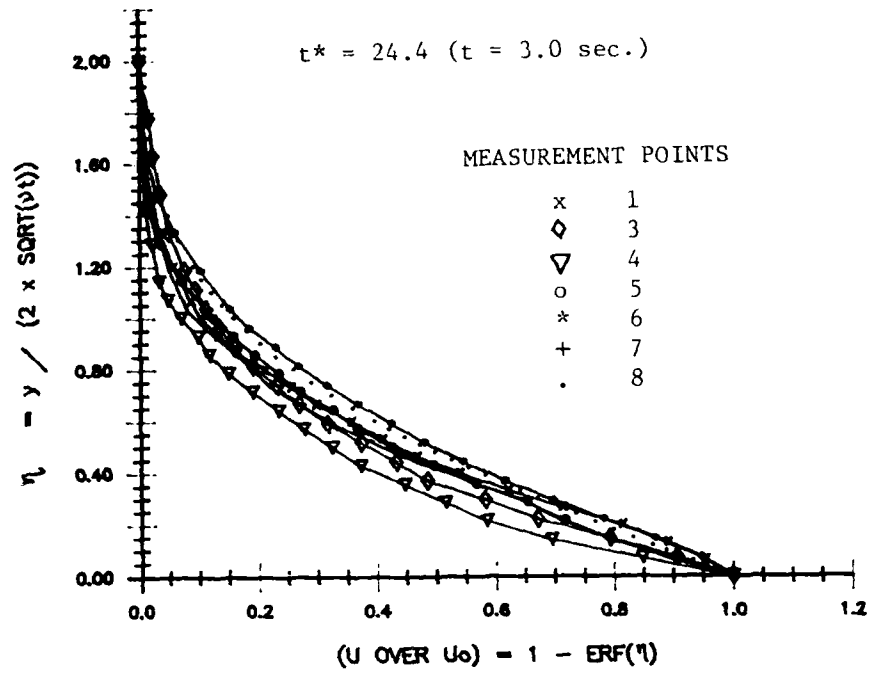


Fig. 4.16 The details of the optical configuration.

A



B

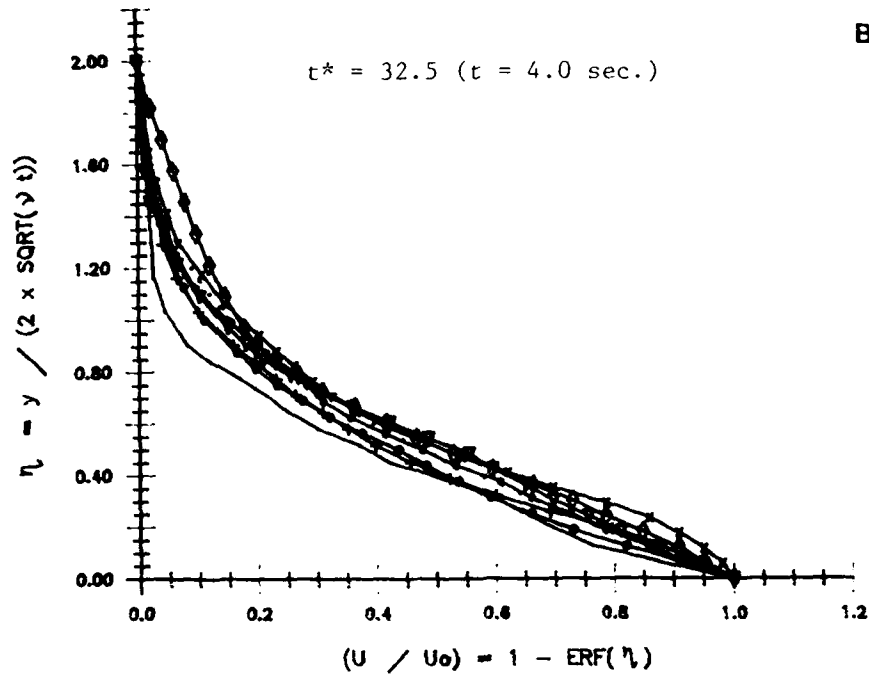


Fig. 4.17 The time evolution of the streamwise velocity distribution at the measurement points. The dotted lines represent the undisturbed velocity profiles of the Stokes' layer.

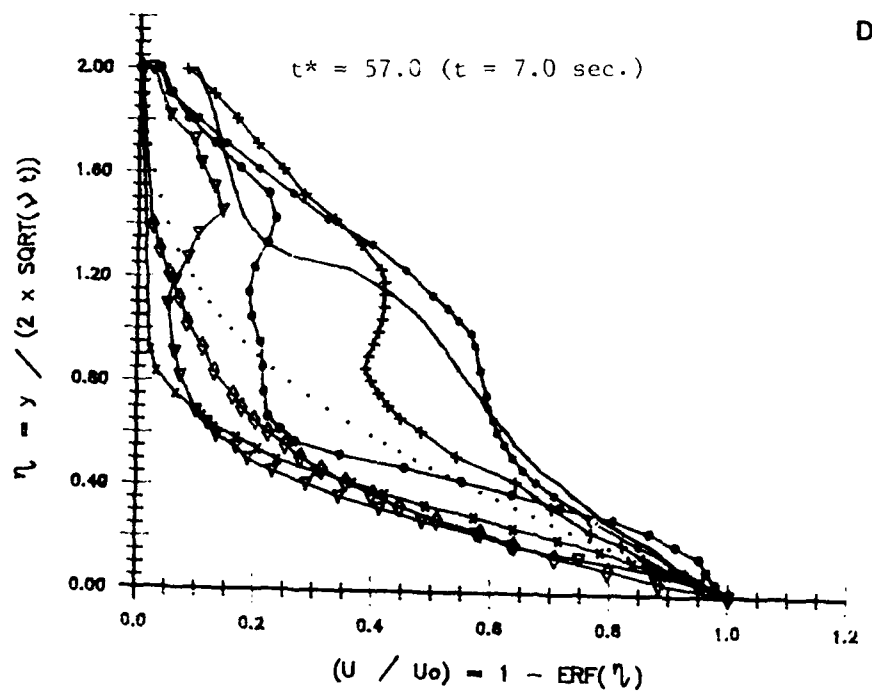
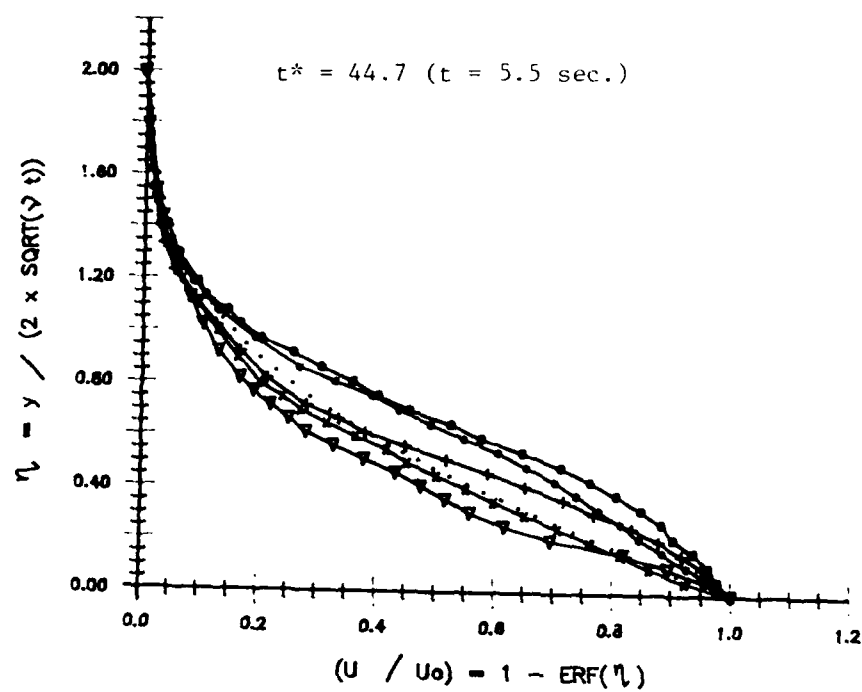
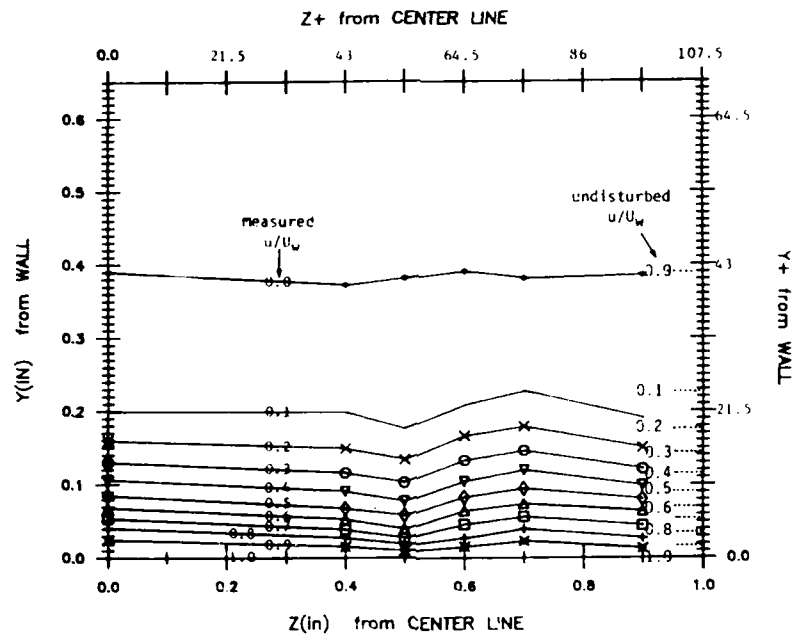


Fig. 4.17 Cont.



CONST.  $u$ , at  $t^* = 24.4$  (3.0 sec)



CONST.  $u$ , at  $t^* = 32.5$  (4.0 sec)

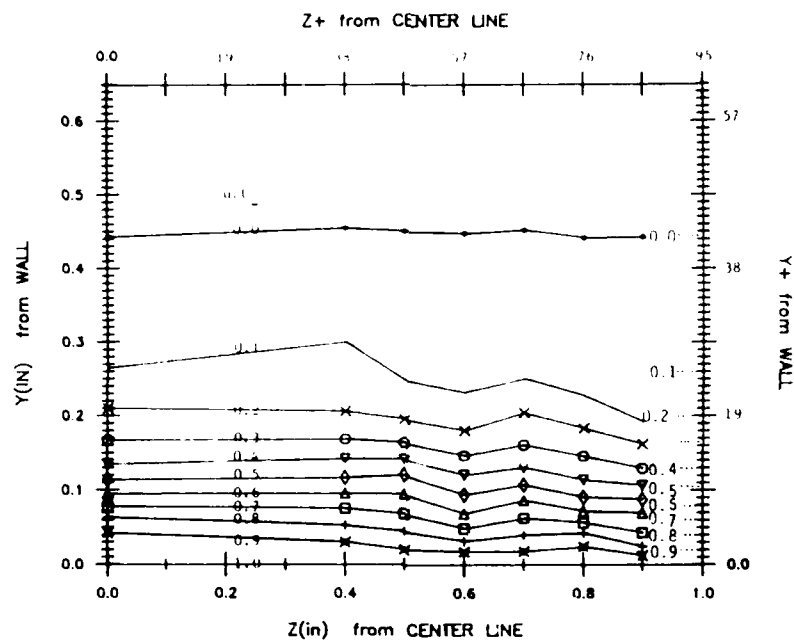
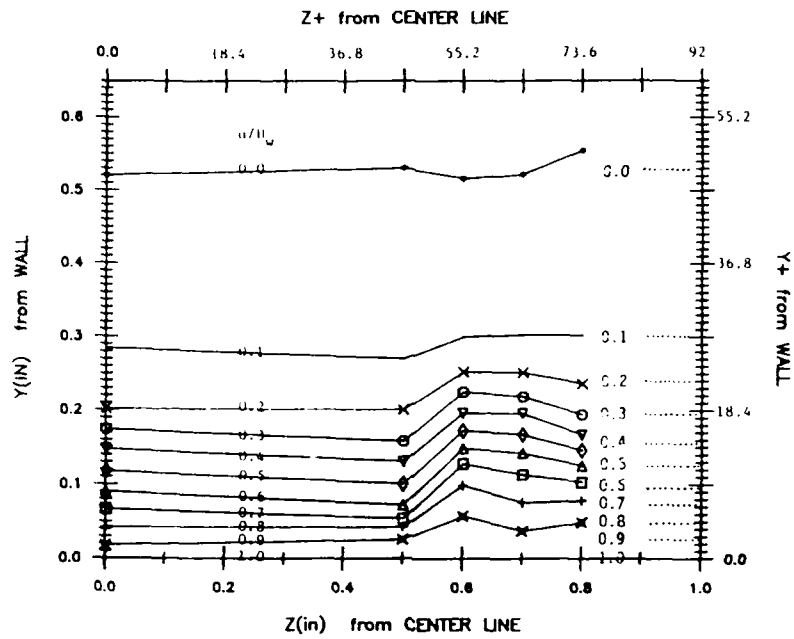


Fig. 4.18 The constant velocity lines in  $y$ - $z$  plane.

CONST.  $u$ , at  $t^* = 44.7$  (5.5 sec)



CONST.  $u$ , at  $t^* = 57.0$  (7.0 sec)

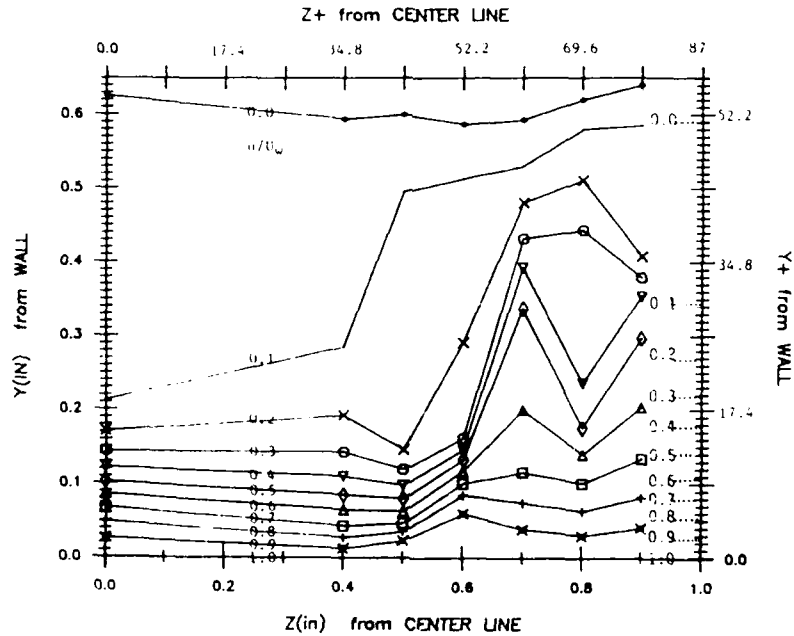


Fig. 4.18 Cont.

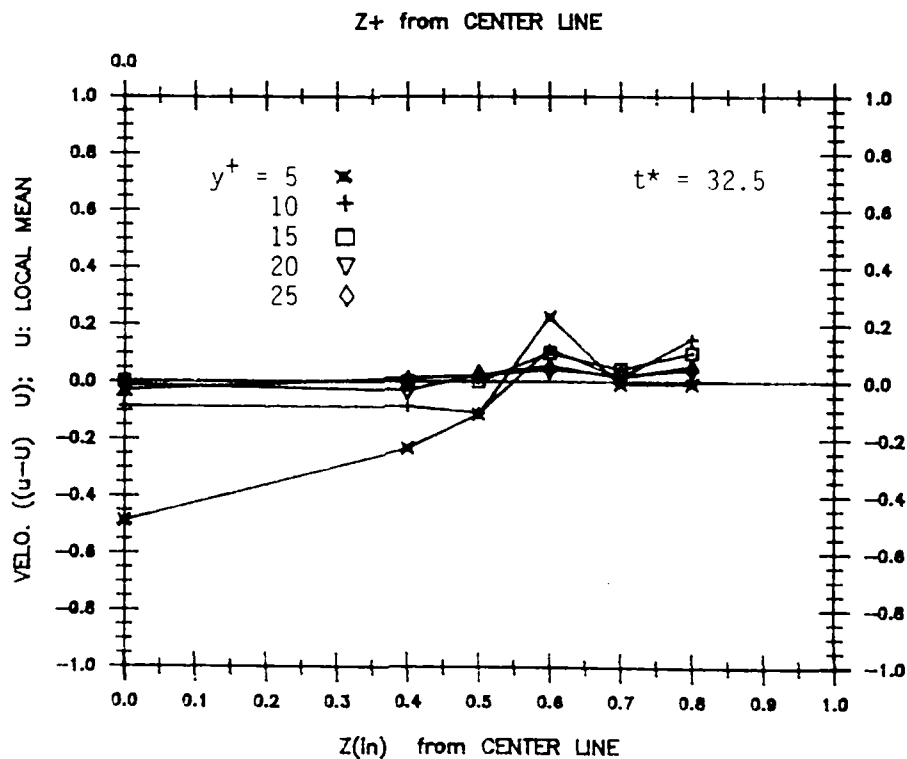
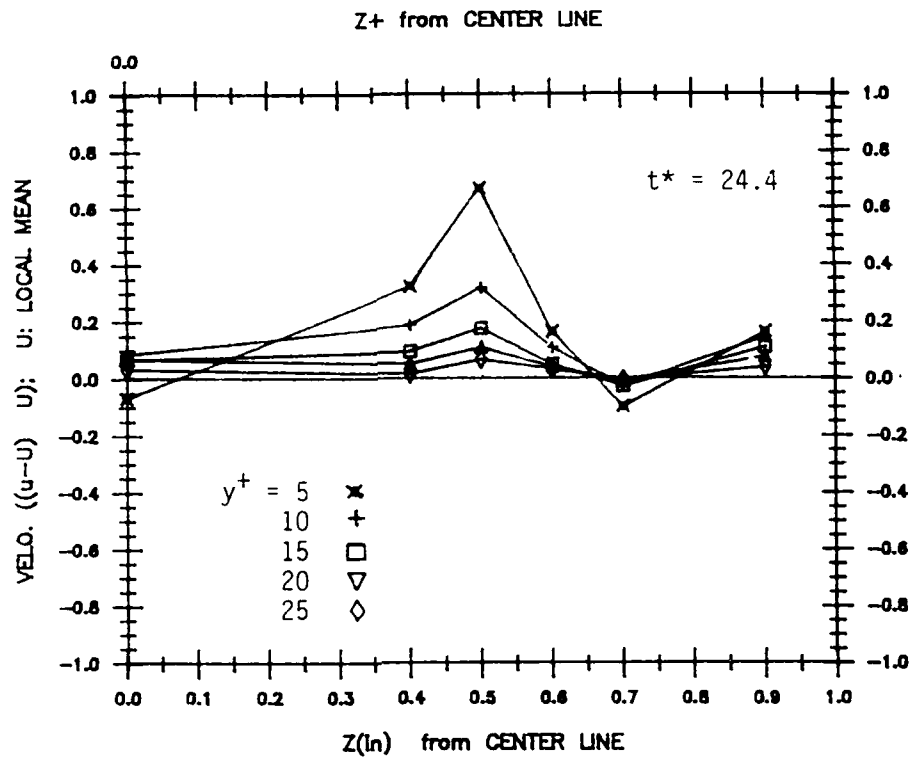


Fig. 4.19 The velocity defect or gain with respect to the undisturbed wall layer shown in (a). These sets of data had been converted to the turbulent boundary layer point of view by performing the Galilean transformation.

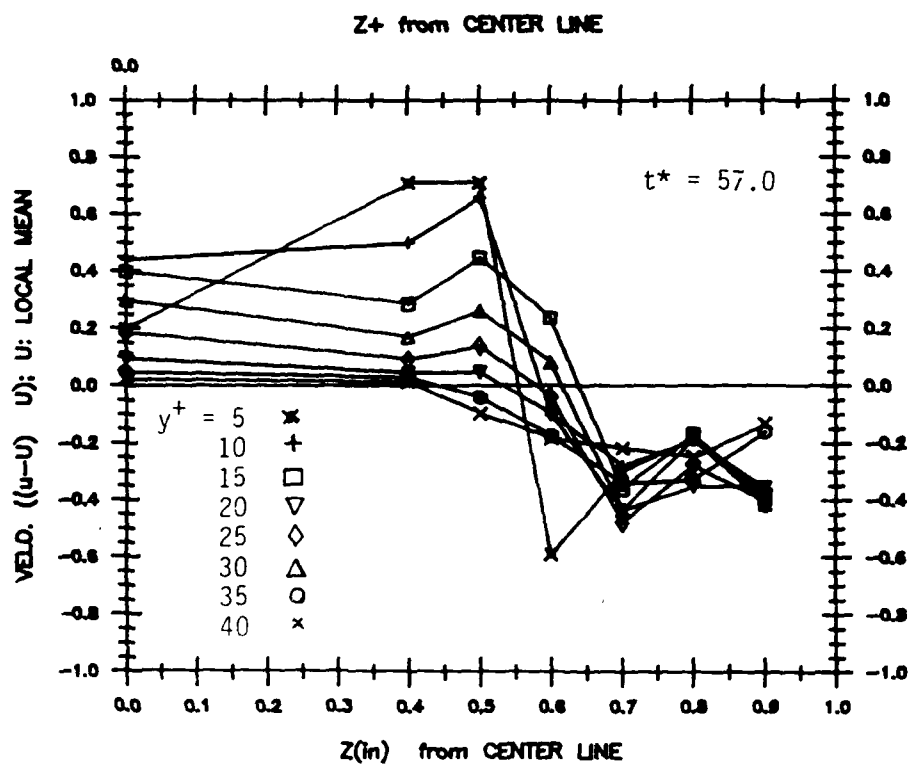
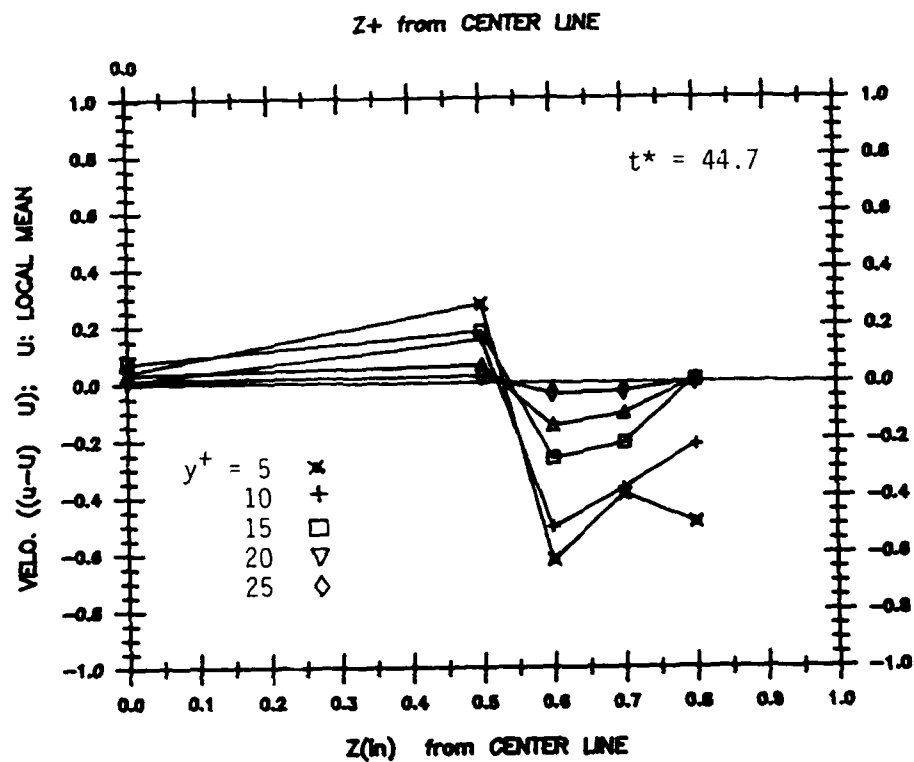


Fig. 4.19 Cont.

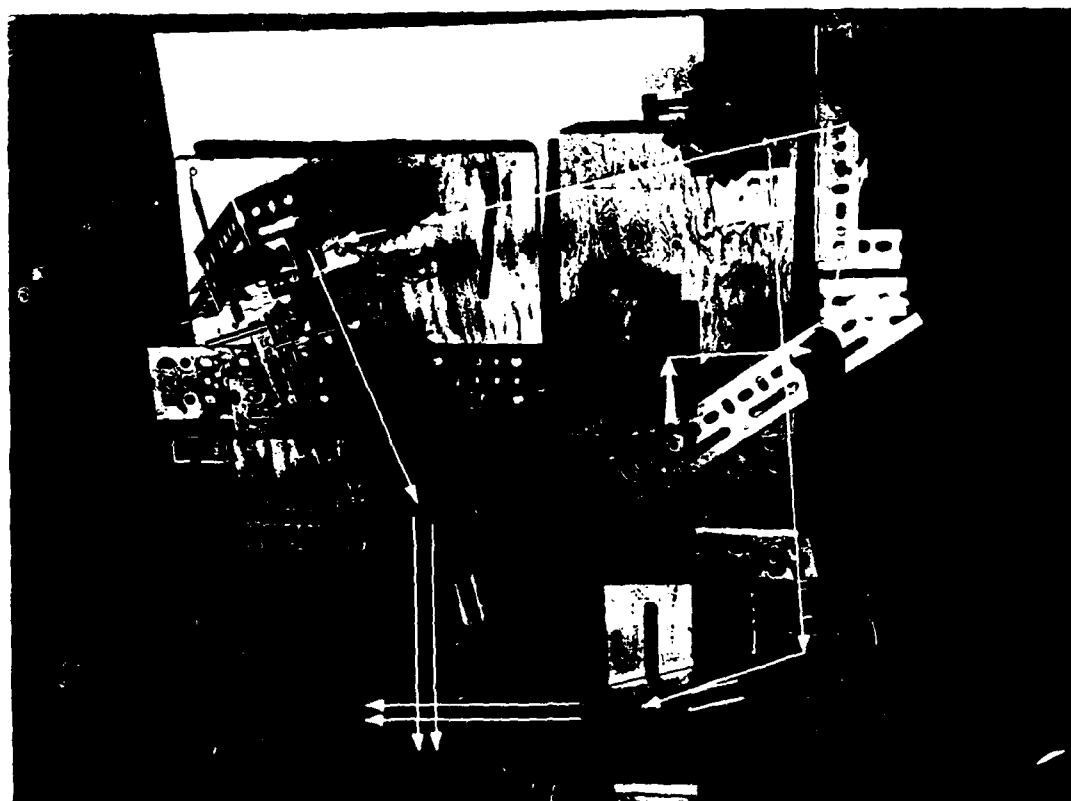


Fig. 4.20 A photo of the optical configuration and the orientation of the laser beam.

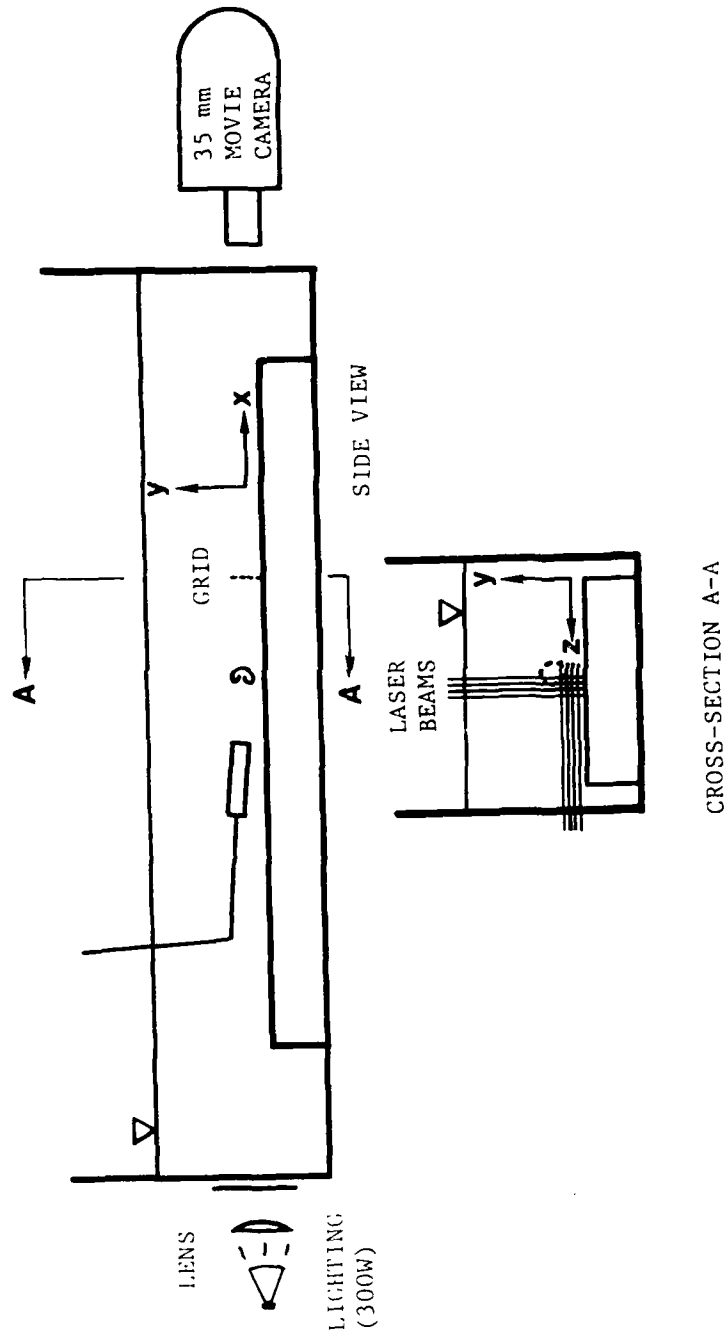


Fig. 4.21 The side view of the data acquisition and lighting system.

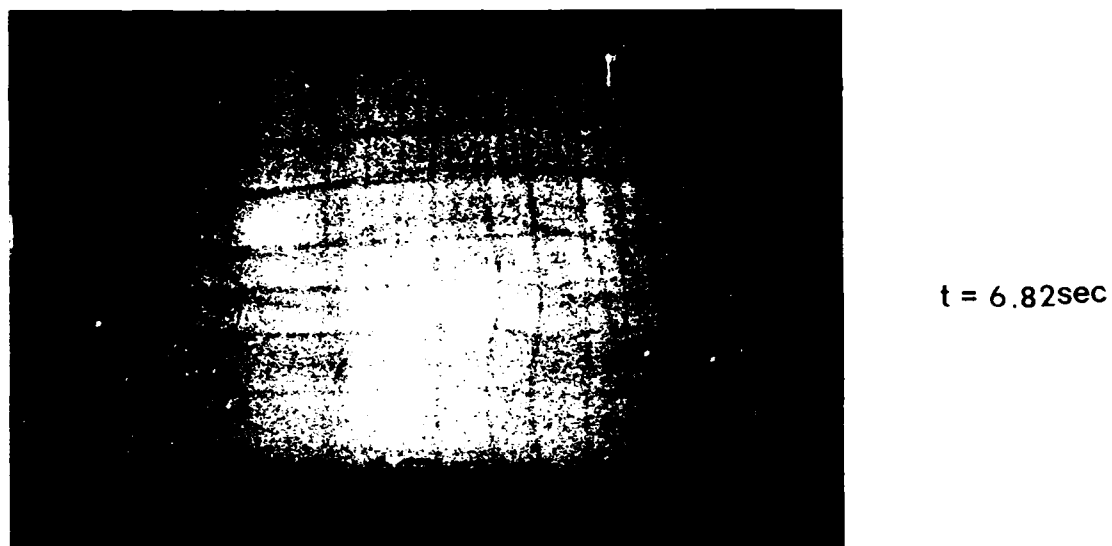
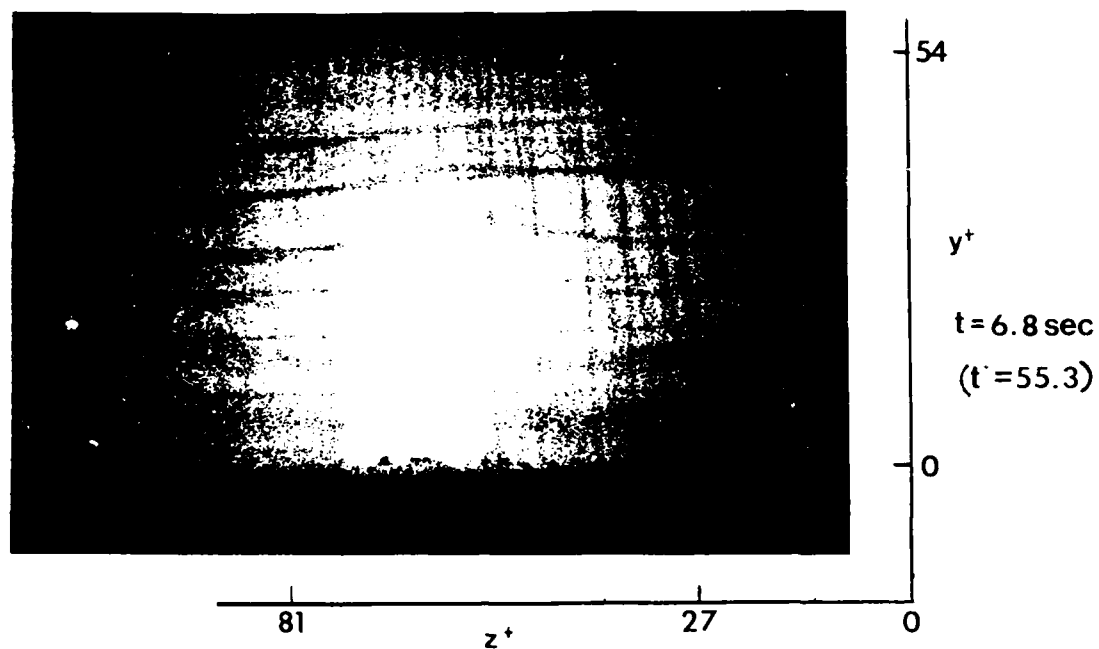


Fig. 4.22 The result of the streamwise vorticity measurement. Those photos are selected from the same sequence of movie in one experiment. Two photos of each set were 0.02 second apart which corresponded to  $0.5t^+$  apart.

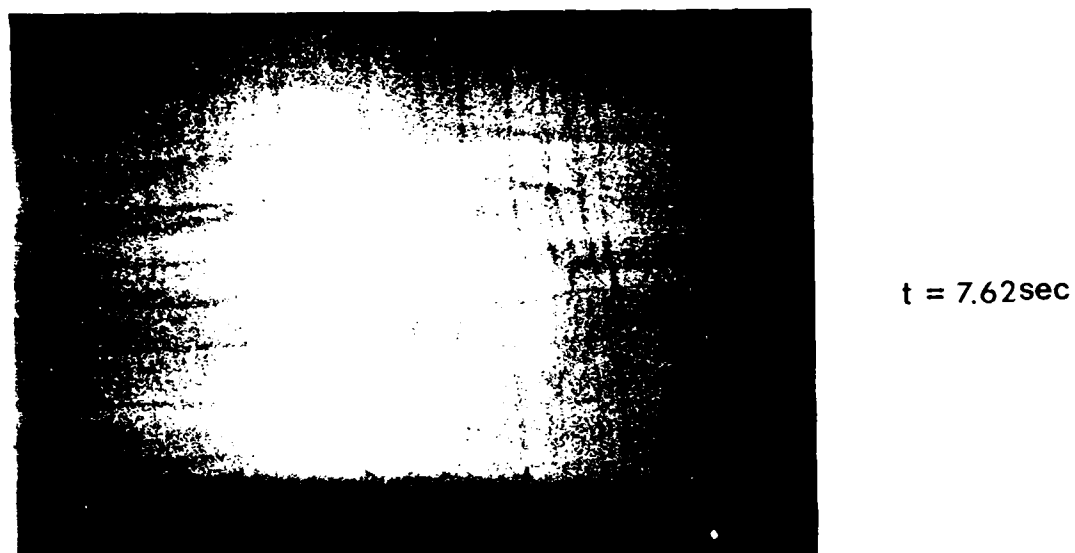
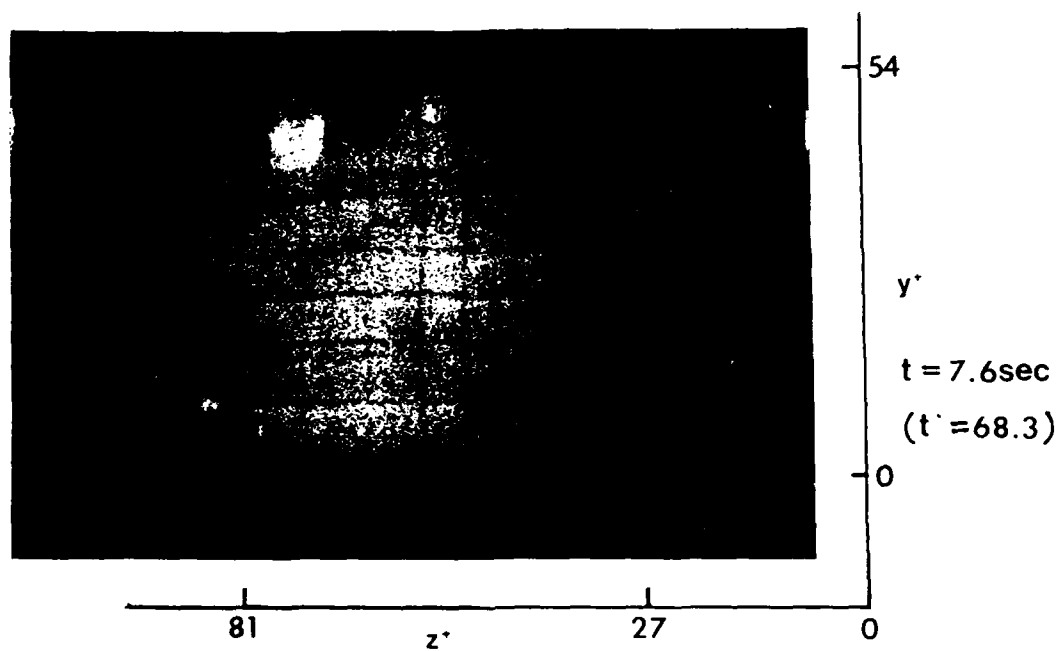


Fig. 4.22 Cont.



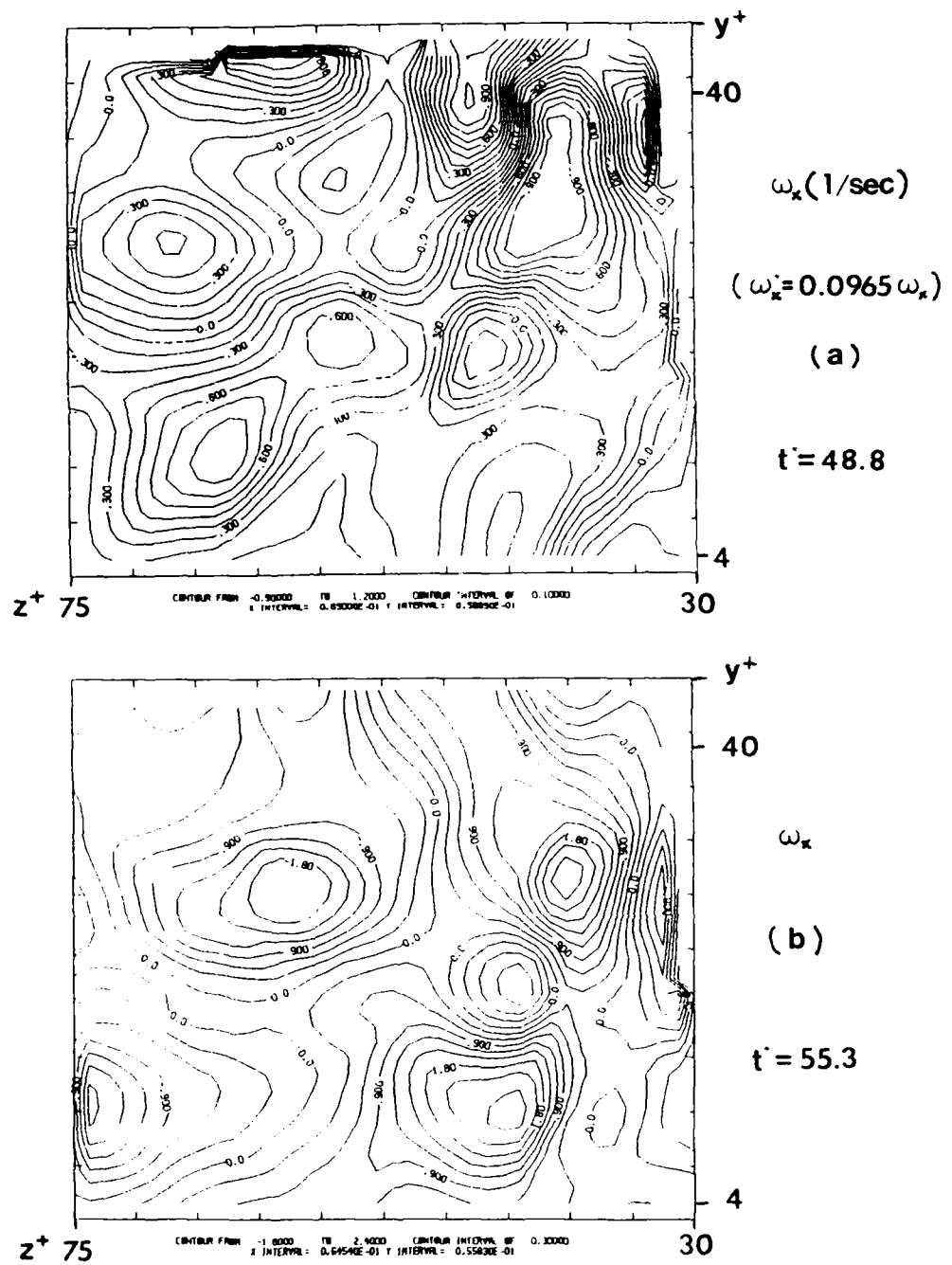


Fig. 4.23 The contour plots of the instantaneous streamwise vorticity distribution.

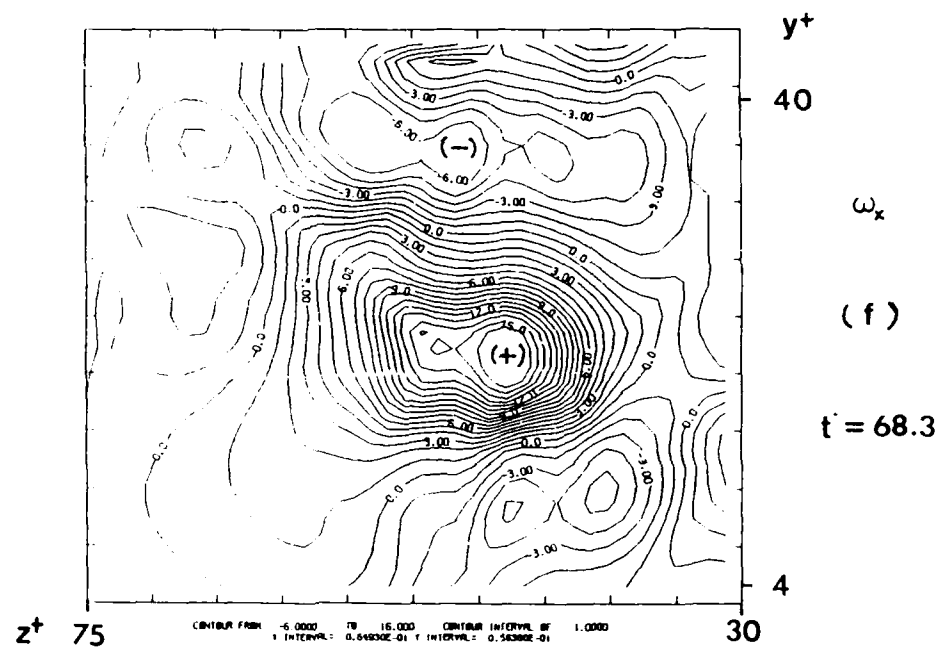
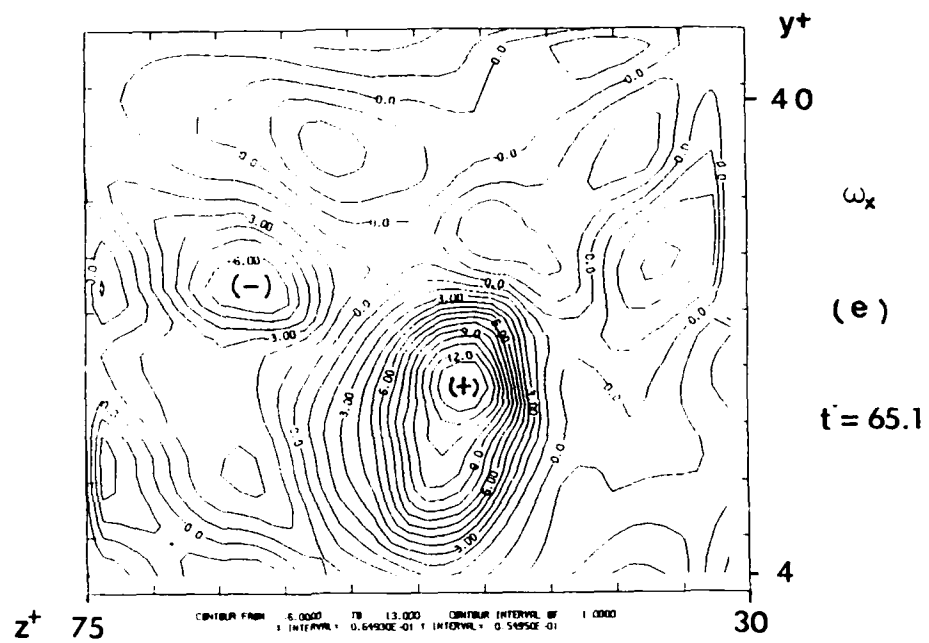


Fig. 4.23 Cont.

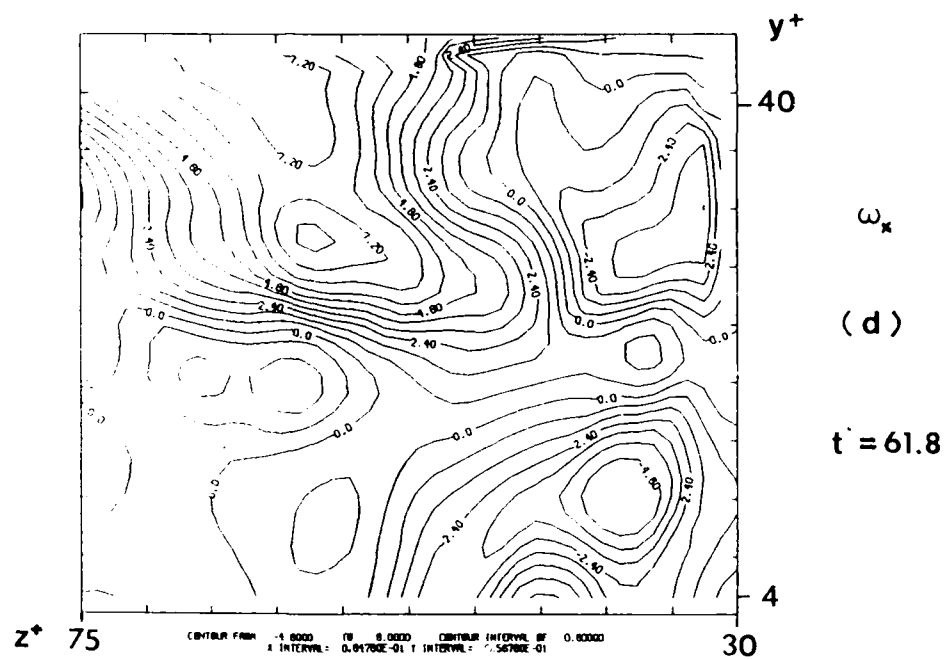
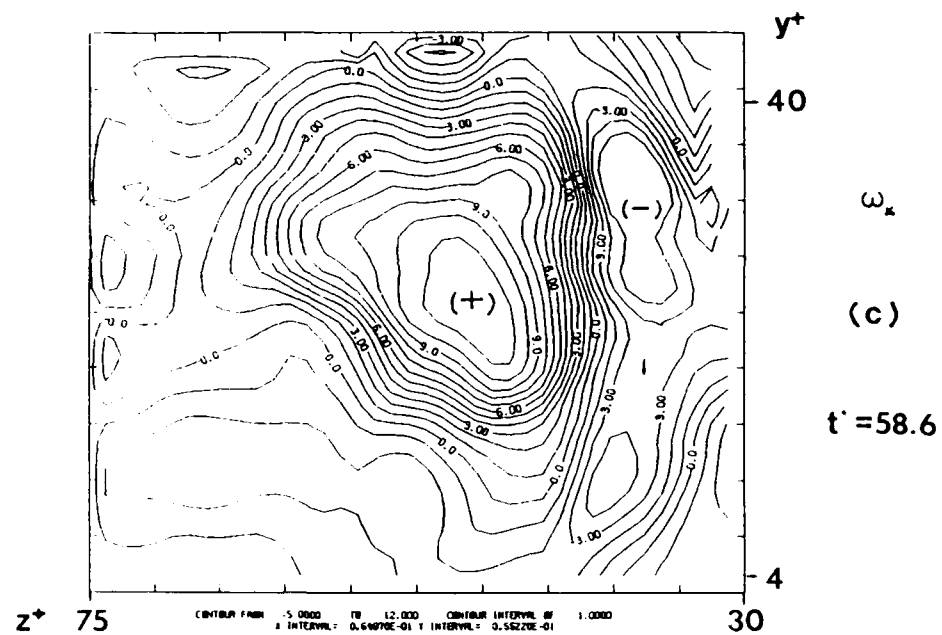


Fig. 4.23 Cont.

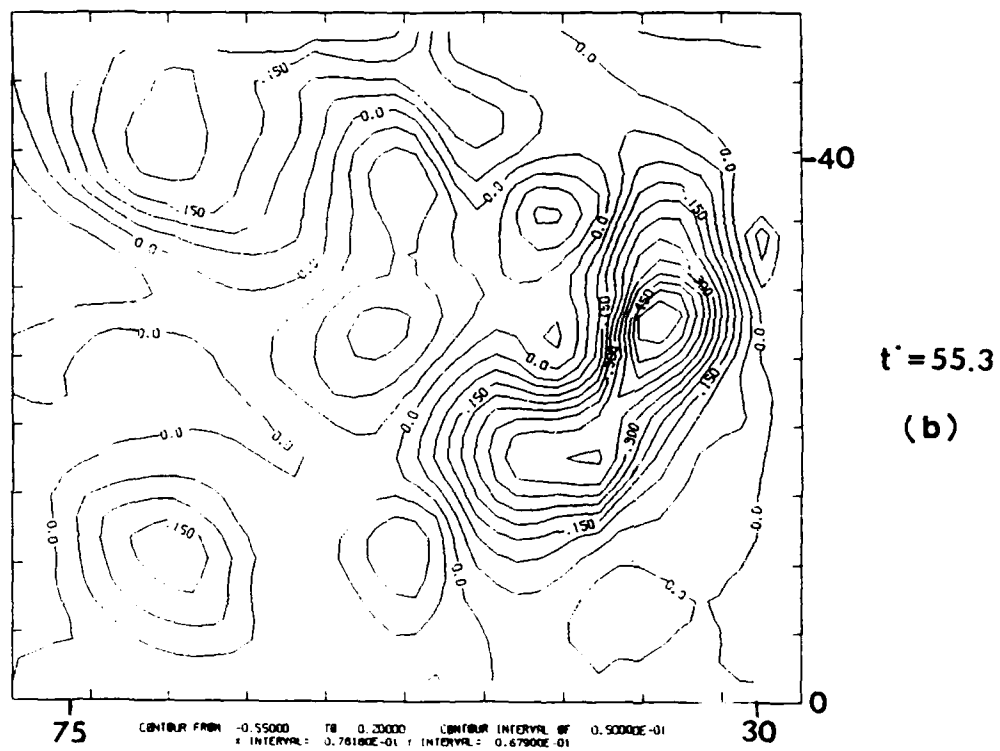
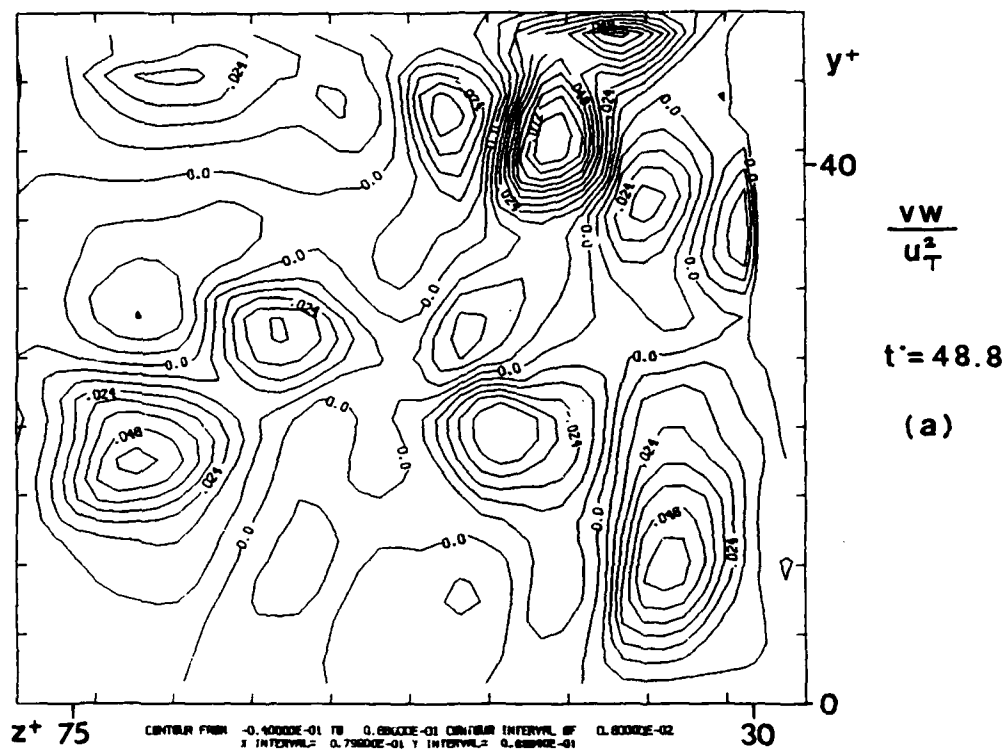


Fig. 4.24 The instantaneous Reynolds stress distributions obtained from Fig. 5.22 (a)-(f).

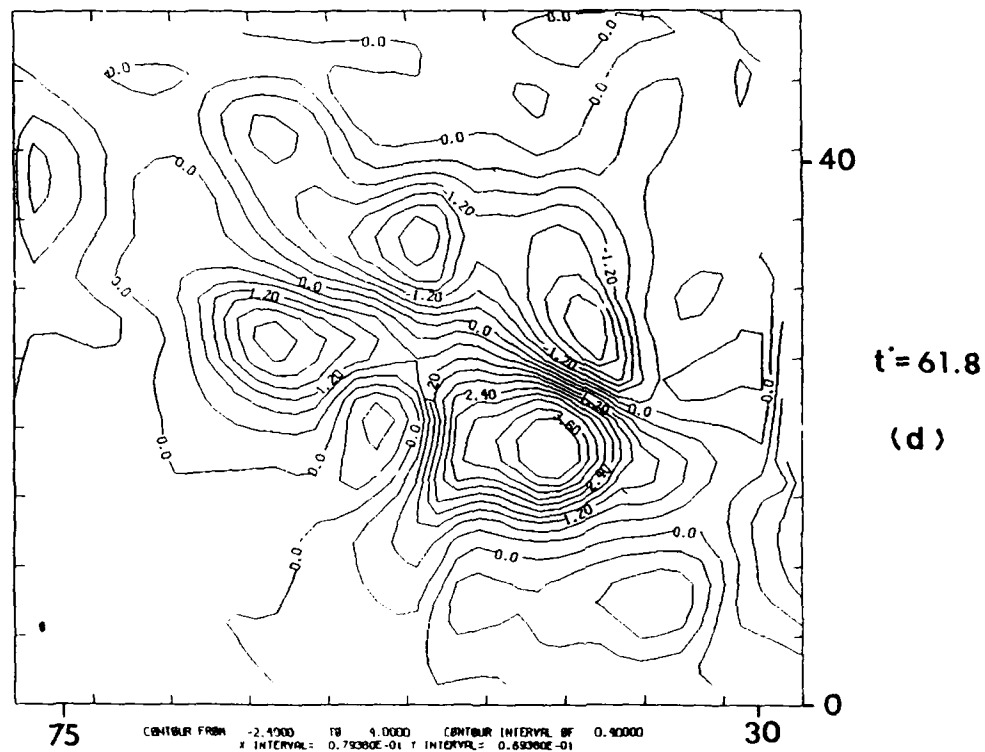
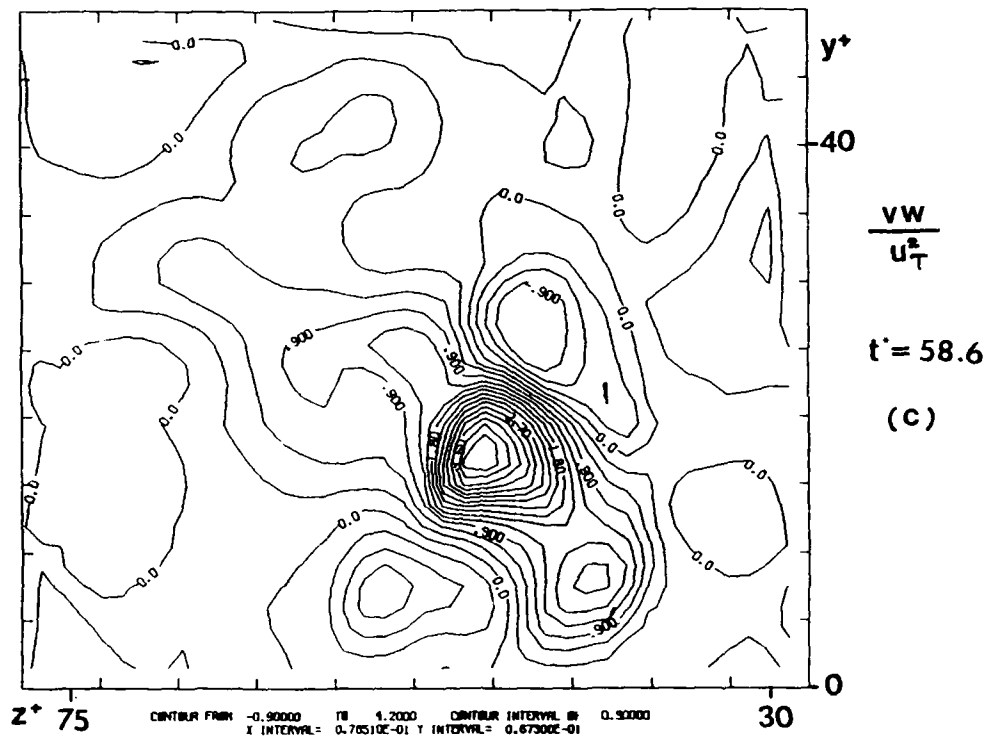


Fig. 4.24 Cont.

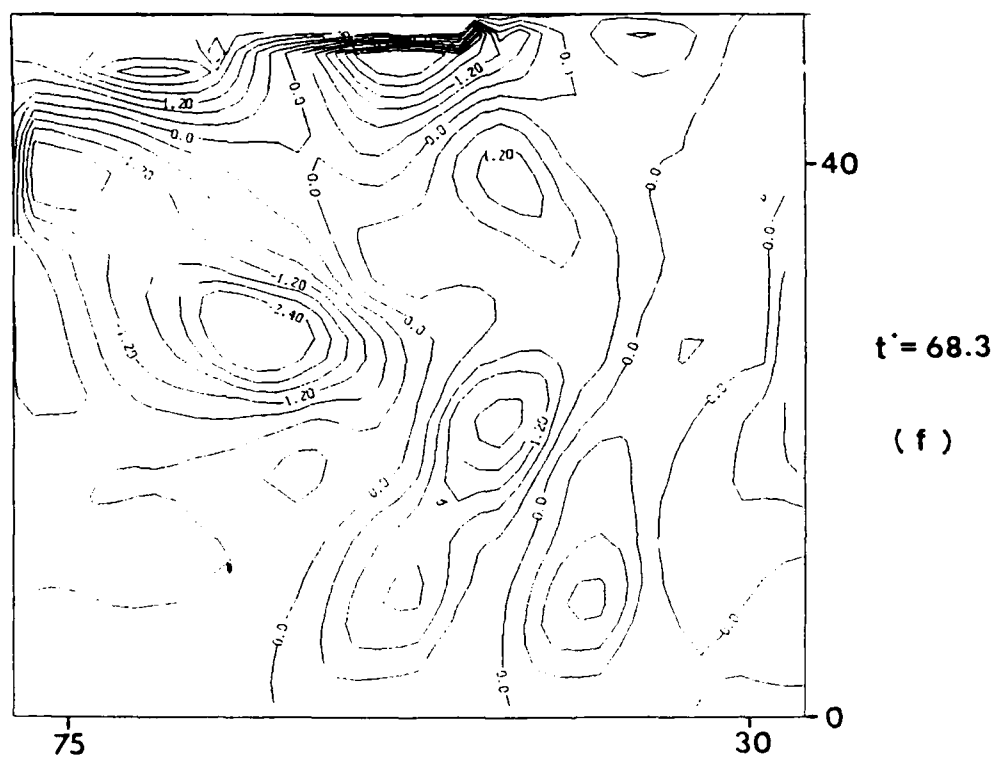
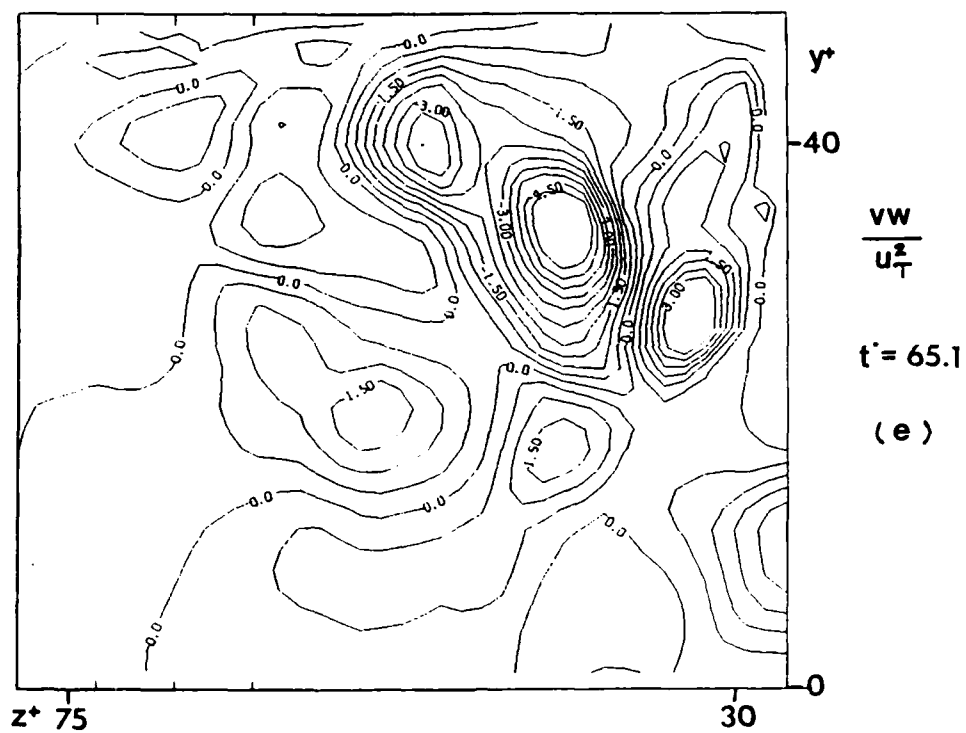
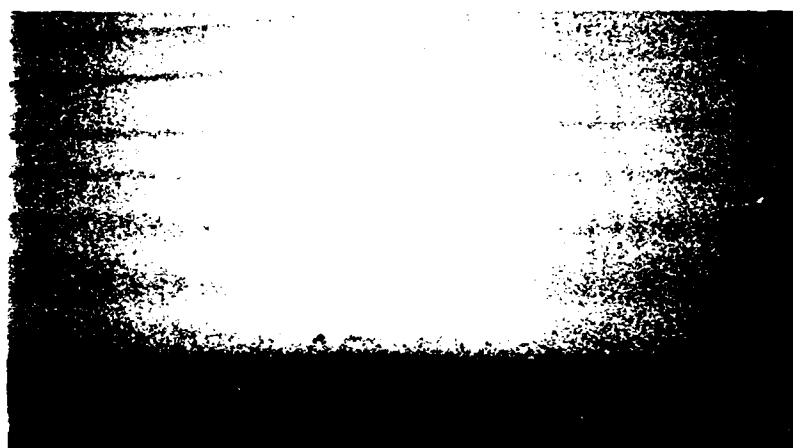
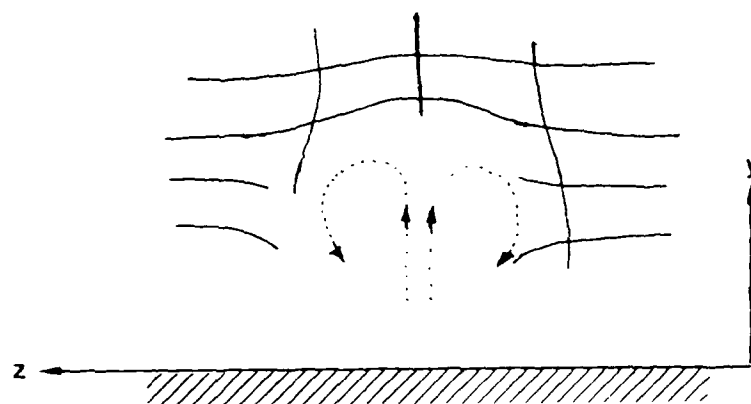


Fig. 4.24 Cont.



( a )



( b )

Fig. 4.25 A photo taken 0.02 second before  $t=6.8$  seconds (shown in Fig. 5.25 (a)) indicates that a pair of counter-rotating streamwise vortices formed from the wall and moved upward.

# CIRCULATION VS TIME

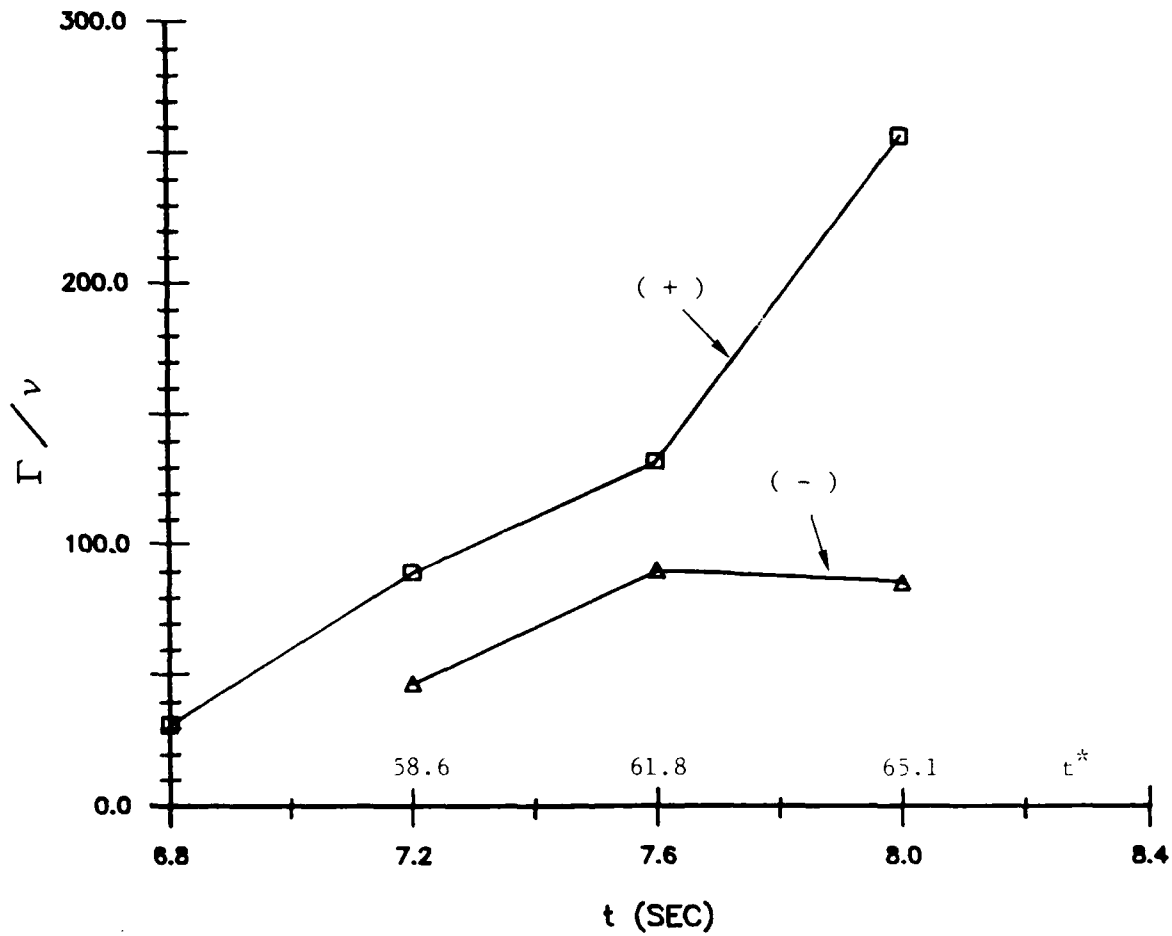


Fig. 4.26 The time evolution of total circulation of the strong vortex (the region with positive sign in Fig.5.22 (c)-(e)); and the time evolution of the total circulation of one leg of the hairpin (the region with negative sign in Fig. 5.22 (c)-(e)).



## APPENDIX A

### ERROR ANALYSIS OF THE PHOTOCHROMIC GRID TRACING TECHNIQUE FOR THE MEASUREMENT OF VORTICITY

Consider a unit of the mesh (see Fig. A.1). The corners of the undistorted mesh are defined as points 1a to 4a in counterclockwise rotation. We will assume that the mesh is spaced  $\epsilon$  and that a worse case line movement between images is 1/2 the mesh width. After time  $\Delta t$  the mesh square will move to position 1b to 4b. The vorticity

$$\begin{aligned}\omega_z &= \partial v / \partial x - \partial u / \partial y \\ &= \frac{(y_{1a} - y_{1b}) / \Delta t - (y_{2a} - y_{2b}) / \Delta t}{(x_{2a} - x_{1a})} \\ &\quad - \frac{(x_{1a} - x_{1b}) / \Delta t - (x_{4a} - x_{4b}) / \Delta t}{(y_{4a} - y_{1a})}\end{aligned}$$

where,

$$y_{1a} - y_{1b} = \Delta y_I = 1/2 \epsilon$$

$$y_{2a} - y_{2b} = \Delta y_{II} = 1/2 \epsilon$$

$$y_{4a} - y_{1a} = \Delta y_{III} = \epsilon$$

$$x_{1a} - x_{1b} = \Delta x_I = 1/2 \epsilon$$

$$x_{4a} - x_{4b} = \Delta x_{II} = 1/2 \epsilon$$

$$x_{2a} - x_{1a} = \Delta x_{III} = \epsilon$$

$$t_2 - t_1 = \Delta t$$

$$\therefore \omega_z = \frac{(\Delta y_I - \Delta y_{II}) / \Delta t}{\Delta x_{III}} - \frac{(\Delta x_I - \Delta x_{II}) / \Delta t}{\Delta y_{III}}$$

The uncertainty in the measurement of vorticity ( $\delta \omega_z$ ) is thus,

$$(\delta \omega_z)^2 = (\partial \omega_z / \partial \Delta y_I \cdot \delta \Delta y_I)^2 + (\partial \omega_z / \partial \Delta y_{II} \cdot \delta \Delta y_{II})^2$$

$$\begin{aligned}
& + (\partial\omega_z/\partial\Delta y_{III} \cdot \delta\Delta y_{III})^2 + (\partial\omega_z/\partial\Delta x_I \cdot \delta\Delta x_I)^2 \\
& + (\partial\omega_z/\partial\Delta x_{II} \cdot \delta\Delta x_{II})^2 + (\partial\omega_z/\partial\Delta x_{III} \cdot \delta\Delta x_{III})^2 \\
& + (\partial\omega_z/\partial\Delta t \cdot \delta\Delta t)^2
\end{aligned}$$

Estimates of the magnitudes of the terms are:

$$\begin{aligned}
\partial\omega_z/\partial\Delta t &= -((\Delta y_I - \Delta y_{II})/\Delta x_{III}/(\Delta t))^2 \\
&+ ((\Delta x_I - \Delta x_{II})/\Delta y_{III}/(\Delta t))^2 \\
&= -((1/2 \epsilon - 1/2 \epsilon)/\epsilon)/(\Delta t)^2 \\
&\cong 0
\end{aligned}$$

$$\partial\omega_z/\partial\Delta y_I = 1/\Delta t \cdot \Delta x_{III} \cong 1/\Delta t \cdot \epsilon$$

$$\partial\omega_z/\partial\Delta y_{II} = -1/\Delta t \cdot \Delta x_{III} \cong 1/\Delta t \cdot \epsilon$$

$$\begin{aligned}
\partial\omega_z/\partial\Delta y_{III} &= ((\Delta x_I - \Delta x_{II})/\Delta t)/(\Delta y_{III})^2 \cong (1/2\epsilon - 1/2\epsilon)/\Delta t \cdot \epsilon^2 \\
&\cong 0
\end{aligned}$$

$$\partial\omega_z/\partial\Delta x_I = -1/\Delta t \cdot \Delta y_{III} \cong -1/\Delta t \cdot \epsilon$$

$$\partial\omega_z/\partial\Delta x_{II} = 1/\Delta t \cdot \Delta y_{III} \cong 1/\Delta t \cdot \epsilon$$

$$\begin{aligned}
\partial\omega_z/\partial\Delta x_{III} &= -((\Delta y_I - \Delta y_{II})/\Delta t)/(\Delta x_{III})^2 \cong -(1/2\epsilon - 1/2\epsilon)/\Delta t \cdot \epsilon^2 \\
&\cong 0
\end{aligned}$$

Therefore  $\delta\omega_z$  squared is equal to :

$$\begin{aligned}
(\delta\omega_z)^2 &= (\delta\epsilon/2\epsilon\Delta t)^2 + (\delta\epsilon/2\epsilon\Delta t)^2 + 0 + (\delta\epsilon/2\epsilon\Delta t)^2 \\
&+ (\delta\epsilon/2\epsilon\Delta t)^2 + (\delta\epsilon/2\epsilon\Delta t)^2 + 0 + 0 \\
&= 4 (\delta\epsilon/2\epsilon\Delta t)^2
\end{aligned}$$

Finally,

$$\delta\omega_z = (1/\Delta t)(\delta\epsilon/\epsilon) \text{ to the first order in } \epsilon.$$

For example, (see Fig. A.2) assume that

96. meshing spacing =  $1000\ \mu\text{m}$

97. line width =  $100\ \mu\text{m}$

98. 10% reading error in reading the center of the  $100\ \mu\text{m}$  line, i.e.  $\delta\epsilon = 10\ \mu\text{m}$ ;

$$\therefore \delta\epsilon/\epsilon = 0.01$$

if  $\Delta t = 0.01$  second (between two frames), we will have

$$\delta\omega_z = (1/\Delta t)(\delta\epsilon/\epsilon) = 1/\text{sec}$$

## APPENDIX B

## APPENDIX C

## Vortex ring/viscous wall layer interaction model of the turbulence production process near walls\*

C. C. Chu and R. E. Falco

Turbulence Structure Laboratory, Dept. of Mechanical Engineering, Michigan State University, East Lansing, MI 48824, USA

**Abstract.** An experimental simulation of the interaction of vortex ring-like eddies with the sublayer of a turbulent boundary layer is investigated. An artificially generated vortex ring interacting with a Stokes' layer enables investigation of the interaction with reproducible initial conditions and in the absence of background turbulence. All of the observed features in the turbulent boundary layer production process such as the streaky structure, the pockets, the hairpin vortices, streak lift-up, oscillation, and breakup, have been observed to form. The model shows us that hairpin vortices can pinchoff and reconnect forming new vortex ring-like eddies. Interestingly, the model includes interactions that occur with low probability in the turbulent boundary layer, but which contribute significantly to transport, and may be the events most readily controllable.

### List of symbols

$D$	the diameter of a vortex ring
$R_\mu$	Reynolds number based on momentum thickness
$T$	time to instability
$T_p$	average time between pockets
$U_c$	convection velocity
$U_r$	velocity of a vortex ring
$U_{TE}$	convection velocity of a Typical eddy
$U_m$	velocity of the moving belt
$u_\tau$	friction velocity
$U_\infty$	freestream velocity
$x$	coordinate in the main flow direction
$y$	coordinate normal to the surface
$z$	spanwise coordinate
$\delta$	the Stokes' layer thickness
$\theta$	momentum thickness of the shear layer
$\nu$	kinematic viscosity
$\lambda$	streamwise wavelength
$\tau$	shear stress
$\omega_z$	spanwise vorticity

### Superscripts

( )<sup>+</sup> non-dimensionalized by  $\nu/u_\tau$ .

### 1 Introduction

There is a need to construct both experimental and numerical simulations of the turbulence production process

near walls, because of the difficulty of isolating mechanisms when experiments are conducted in the boundary layer flows. A good simulation must embody the essential features of the production process. In this paper we report a new observation in turbulent boundary layers that helps complete the picture of structural feature interactions, and then present an experimental simulation that models all of the important properties.

Turbulent boundary layer structure that should be modeled includes the long streaks (Runstadler et al. 1963), the pockets (Falco 1980a, 1980b), the hairpins (Falco 1982, Acarlar and Smith 1984), the Typical eddies (Falco 1977, 1983), and coherent regions of streamwise vorticity and/or streamwise vortices. Basically, these structural features have been shown to be associated with the production process, but the formation of the structures and the interactions are not completely understood. A number of investigators have studied the formation of low speed streaks. Oldaker and Tiederman (1977) observed that a pair of low speed streaks formed as a result of the response to what appeared to be a sequence of local high speed outer region eddies interacting with the wall and aligned along a streamwise direction. The path left by the outer region disturbances clearly formed a high speed streak. Falco (1980a) observed the formation of low speed streaks in pairs by a similar mechanism. Although low speed streaks are often observed to exist singly, care must be taken when interpreting low speed streak formation, because once formed the low speed streaks can persist for very long times (Smith and Metzler 1983), and have simply convected into the observation zone.

Since the mid fifties, it has been suggested that long counter rotating streamwise vortices exist in the wall region and that pairs of these vortices produce a gathering of wall layer dye between them that we see as the low speed streaks. A high speed streak would be the result of high speed fluid being induced towards the wall between a pair of these streamwise vortices rotating the other way. A number of authors have suggested causes for these streamwise vortices. The currently most popular sug-

\* A version of this paper was presented at the Tenth Symposium on Turbulence, University of Missouri-Rolla, Sept. 22–24, 1986

gestion is that they are the 'legs' of hairpin vortices that are also observed in the wall region. However, as Acarlar and Smith (1981) have pointed out, it is very hard to understand how the hairpin legs could extend upstream as far as would be necessary to produce streaks of length  $x^+ = O(1000)$ . Thus, there is still no experimental evidence supporting the various rational physical hypotheses describing the formation of long streaks.

Another feature of the wall region structure is the frequent rearrangement of marker that moves it away from a local region, leaving a scoured 'pocket' of low marker concentration. Figure 1 shows two pockets as seen in a layer of smoke marked sublayer fluid. Pockets are footprints of outer region motions that interact with the wall. Falco (1980a) showed that they start out as a movement of wall layer fluid away from a location as a high speed outer region eddy (a Typical eddy, discussed below), nears the wall. The interaction results in the footprint opening up into a developed pocket shape. Fluid is seen to lift-up from the downstream end of the pocket, and take on the characteristics of a hairpin vortex (Falco 1982).

We have also observed hairpins appearing to form over individual streaks. The streak is seen to become lumpy, and one of the lumps grows and a hairpin emerges from it. Acarlar and Smith (1984) have also observed hairpins growing over simulated streaks, and it appears, in a turbulent boundary layer.

The microscale coherent motions observed across a turbulent boundary layer, which are similar to laminar vortex rings embedded in a shear flow, are called Typical eddies. They have been studied by Falco (1974, 1977, 1982, 1983), who showed that they contribute significantly to the Reynolds stress in the outer part of the boundary layer, and that they are the excitation eddies that create the pockets. Experiments using two mutually orthogonal sheets of laser light enabled Falco (1980b) to determine, as far as the smoke marking allows, that the coherent feature was a ring, as opposed to a portion of a hairpin vortex, as suggested by Head and Bandyopadhyay (1981).

Both types of hairpin creation mechanisms described above can produce hairpins that can pinch-off and form new vortex rings. Falco (1983) showed visual evidence of a hairpin lifting from the downstream end of a pocket, contorting and pinching off to form a new vortex ring-like Typical eddy. This pinch-off mechanism has also been clearly shown to occur in the calculations of Moin et al. (1986) mentioned above.

Many investigators have noted the presence of streamwise vortices in the wall region. Almost without exception, the vortices have been of short extent (Praturi and Brodkey 1978, Falco 1980b, Smith 1982). A number of investigators have suggested that streamwise vortices of much greater extent exist in the wall region, essentially laying just above the wall in pairs, which are responsible for the creation of both low and high speed streaks. This evidence is of a statistical nature, usually from correlation measure-

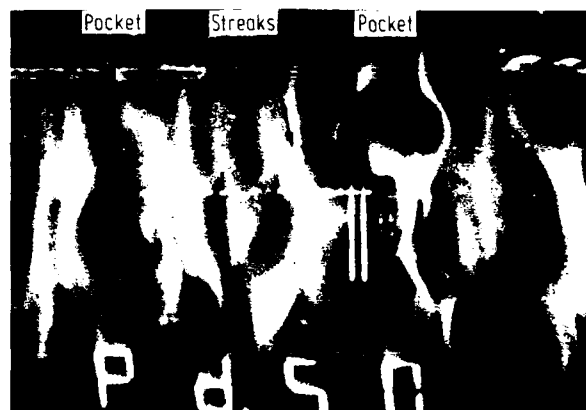


**Fig. 1.** Two pockets and a pair of streaks as seen in wall slit visualization of the sublayer of a turbulent boundary layer using smoke as the contaminant in air; the slit is at the top of the photo, and the flow is from top to bottom

ments. However, no one has ever observed them, and recent calculations of turbulent channel flow using the full Navier-Stokes equations (Kim 1986), have shown that the eddies which have streamwise vorticity are not elongated in the stream direction.

We will present new boundary layer observations on the formation of streamwise streaks, show that the vortex ring/wall layer simulation can exhibit all of the structural features discussed above, and help us understand their formation and interactions.

## 2 Experimental techniques

The boundary layer motions were made visible by seeding the flow with 0.5 – 5 micron oil droplets, and illuminating the oil fog with laser light spread into sheets that could be placed parallel to the wall in the wall region, or perpendicular to the wall and parallel to the flow, or both. The technique has been described by Falco (1980c), so we will not repeat the details here. A new twist, used in these new experiments, which was of particular value in finding the long streaks and their correspondence with the coherent motions above the wall, was the capability to observe the washout of smoke in a laser sheet parallel to the wall while we could simultaneously observe the motion above the wall in a laser sheet perpendicular to the wall and parallel to the flow.

### 2.1 Vortex ring/moving wall simulations

We can simulate the interaction of a Typical eddy with the viscous wall region of a turbulent boundary layer by creating a vortex ring and having it convect towards or away from a moving wall. For convenience, we have used an impulsively started wall. It has the advantages of being

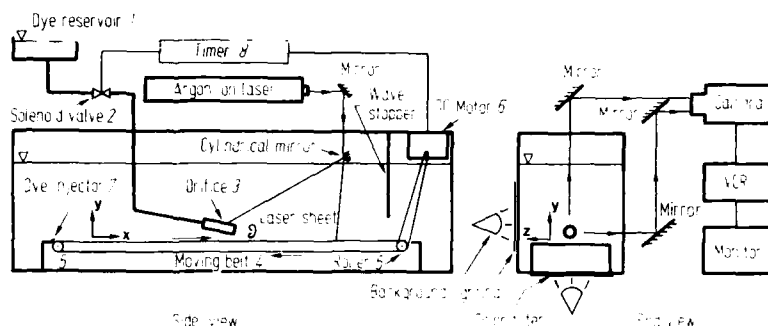


Fig. 2. Side and end views of a schematic of the experimental apparatus used in the vortex ring/moving wall simulations

an exact solution of the Navier-Stokes equations (Stokes' first problem), and therefore is well defined. Furthermore, the velocity profile is approximately linear in the wall region which is similar to the mean velocity profile of the viscous sublayer of a turbulent boundary layer. It is relatively easy to match the friction velocity in these simulations with those found in low Reynolds number turbulent boundary layers. We can also match the Reynolds number and relative convection velocity of the Typical eddies.

Experimental simulations were performed in a water tank which is 0.41 m deep by 0.32 m wide by 2.44 m long. Figure 2 shows the side view and end view of the experimental apparatus which includes a vortex ring generating device, a moving belt and driving arrangement, a synchronizing timer, and visualization recording devices.

The vortex ring generating device includes a constant head reservoir from which fluid, which could be dyed, passes through a solenoid valve whose opening time could be varied, and an orifice of prescribed size (Fig. 2, items 1, 2, and 3). The constant head reservoir (item 1) is filled with a mixture of 10 ppm Fluorescent Sodium Salt Sigma No. F-6377 green dye and water solution. As the solenoid valve (2) opens, a slug of dyed fluid is released from the orifice (3) by the pressure head, and rolls up into a vortex ring. Three different inner diameters of the orifice have been used: 2.54 cm, 1.27 cm, and 0.95 cm. The size and speed of the vortex ring generated depends upon both the height of the dye reservoir and the opening duration time of the solenoid valve for a fixed orifice. The details were discussed in Liang (1984).

The wall upon which the vortex ring interacted is actually a moving belt (4) made of transparent plastic which has a smooth surface. Two ends of the belt are joined together to form a loop, which circulates around two rollers (5) as shown in Fig. 2. The width of the belt is 17.8 cm; and the distance between the two rollers is 152.4 cm. The test section is at 76.2 cm downstream from one of the rollers, giving us a Stokes' layer for this distance (if the belt is run longer, Blasius effects begin to enter into the problem). This width/length ratio is sufficient to prevent the disturbances generated in the corners from reaching the center of the belt at the test section. Therefore, the wall

layer flow on the moving belt could be considered two-dimensional. One of the rollers is driven by a 1/4 hp DC motor (6). The speed of the belt is adjustable within the range of 2.5 cm/s to 22.9 cm/s. The belt reaches a constant speed very soon (within a second) after power is turned on. This short acceleration period allows us to consider the belt to be impulsively started. As the belt moves, a Stokes' layer builds up on the belt. A mixture of red food coloring and water is used to mark the wall layer for visualization. The belt is covered with dye before each run during a 'dye run' using a dye injector near the leading roller of the belt, shown in Fig. 2 (7). The fluid is allowed to come to complete rest before each 'data run'.

The opening duration time of the solenoid valve, and the time delay between the onset of the belt movement and release of the vortex ring, are controlled by a 115 VAC/60 Hz timer designed in the laboratory. Since the thickness of the Stokes' layer,  $\delta$ , is a function of the square root of the belt run time, by carefully adjusting the time delay, we can adjust  $\delta/D$  as desired.

The primary visual data consisted of simultaneous plan and side view time resolved images which were collected using a standard video camera, a VCR, and a monitor, and are shown in the end view of Fig. 2. The side view was often illuminated by a laser sheet emitted from an 8 W Coherent CR-8 Supergraphite Argon Ion Laser. The visual data were analyzed on a high resolution monitor with a superimposed calibrated scale, using the slow motion capabilities of the recorder.

### 3 New boundary layer observations

A major discovery made during this investigation is that as a Typical eddy convects over the wall, it causes an interaction that results in the formation of a pair of long streaks. If the Typical eddy is convecting towards the wall, when it gets close enough, it will create a pocket, and have one of four types of interactions defined below. The creation of the long streaks occurs even when the Typical eddies are quite distant from the wall, well into the log region.



Observations mentioned above have indicated that hairpin vortices can form as a result of pocket evolution and as a result of lumping instability of existing low speed streaks. We have now identified another mechanism that can result in the formation of hairpin vortices. When a Typical eddy is moving away from the wall at a shallow angle and when it is moving relatively slowly, say  $U_x/U_w < 0.4$ , it will create a pair of long very stable streaks that trail behind a hairpin vortex that lifts-up slowly. The eddy can be as far from the wall as indicated above, and thus, will convect appreciably downstream before the hairpin will be noticed. It may convect out of a field of view, leaving the observer with the impression that the formation of the hairpin did not involve the coherent motion.

Thus, only one coherent motion – interacting with the wall – is necessary to create the long streaks, the pockets and the hairpins. Since all of the remaining structure found in the wall region is related to these structures, we can say that the Typical eddy is responsible for the onset of the turbulent production process.

#### 4 Vortex ring/moving wall simulation of the turbulence production process

We can simulate the interaction of a Typical eddy with the wall region of a turbulent boundary layer by creating a vortex ring and having it convect towards a moving wall. Both the wall and the ring move in the same direction. Figure 3 shows the basic idea behind the simulation. The vortex ring can be aimed at or away from the wall at shallow angles.

To interpret the results of the vortex ring/moving wall interactions in terms of turbulent boundary layer interactions, we must perform a Galilean transformation on the velocity field. Our interpretation of the simulation has been to identify the Stokes' layer with the viscous wall region which extends to  $y^+$  approximately 30–50. The mean velocity at this height is approximately 70–80% of  $U_x$ . Thus,

$$U_{TE}/U_x = a(1 - U_x/U_w)$$

where  $a$  represents the outer region velocity defect which we cannot simulate (20–30%). Thus, in thinking about the implications for the turbulent boundary layer, basically high speed ratios in the simulations correspond to low convection velocities of the Typical eddies in the boundary layer.

As a result, we expect the Typical eddies that emerge from wall layer fluid (through a pinch-off of lifted hairpin vortices, for example) to have a low convection velocity. Since these are moving away from the wall, they will correspond to fast rings moving away from the wall. These exhibit long streak formation which is stable, and pinch-off, depending upon the thickness of the wall layer. We do see long stable low speed streaks in the boundary layer, and we have limited evidence of hairpin pinch-off. On the other hand, Typical eddies that are convecting towards the wall will be of relatively high speed, and thus simulated by low speed vortex rings moving towards the wall.

The Reynolds numbers based upon the initial ring velocity and diameter of the dyed ring bubble,  $D$ , ranges between 900 and 2000. When created away from walls, these rings remain stable to azimuthal instabilities over

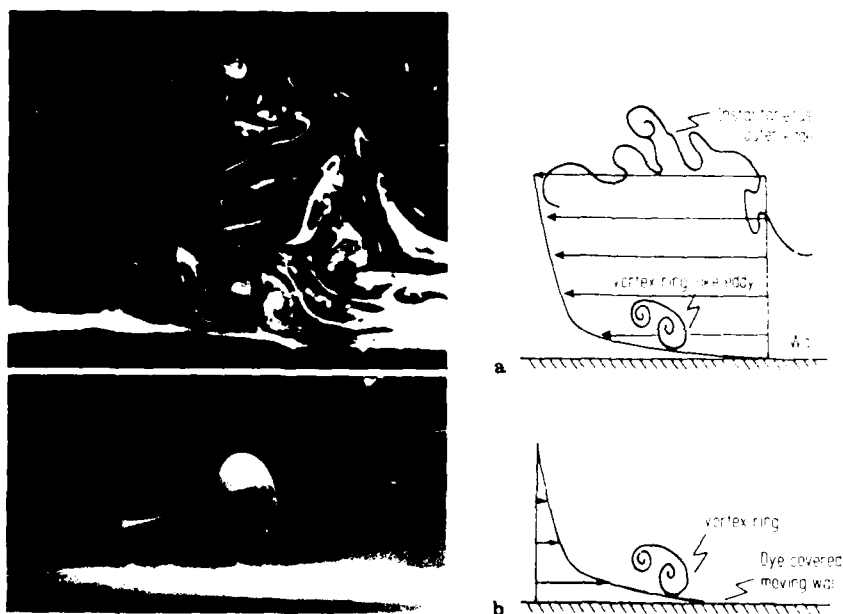


**Fig. 3a and b.** The basic idea behind the simulation. Performing a Galilean transformation on the vortex ring/moving wall interaction makes it a model of the turbulent boundary layer production process; **a** instantaneous turbulent boundary layer; **b** simulated vortex ring/wall shear layer

durations longer than those used in the interaction experiments.

## 5 Vortex ring/moving wall interactions

We will describe the model in terms of the velocity ratios and spatial relationships of the simulation. Later in the discussion, we will invoke the Galilean transformation to relate the findings to the turbulent boundary layer case.

### 5.1 Fast rings ( $U_r/U_w > 0.45$ ) moving towards the wall

Interactions which result from these rings have been described by Liang et al. (1983). They result in the formation of a pocket, and varying degrees of lift-up of wall layer fluid. The interactions have been divided into four types. Figure 4 shows sketches of the four types of interaction. Type I results in a minor rearrangement of the wall layer fluid; followed by the ring moving away from the wall essentially undisturbed. Type II results in a well defined lift-up of wall layer fluid, which takes on a hairpin configuration. This fluid does not get ingested into the ring, and the ring moves away from the wall unperturbed, but still a stable ring. The hairpin has been observed to pinch-off, or just move back down towards the wall and dissipate. Type III results in a lifted

hairpin of wall layer fluid which gets ingested into the ring, resulting in a chaotic breakdown of both the lifted hairpin and the vortex ring, as the vortex ring is moving away from the wall. Type IV also initiates a hairpin vortex, but in this case the hairpin vortex is ingested into the ring on a much shorter timescale, and the ring and lifted wall layer fluid both breakdown while the ring is very close to the wall.

Liang et al. (1983) used vortex rings with  $D^+ > 250$  and  $\delta^+$  between 20 and 50, and they observed only the above four types of interactions. Our experiments indicate that if  $D^+ < 150$  and  $\delta^+$  is between 20 and 50, we can also obtain the four types of interactions noted above, but, in addition, we found that long streaks also formed. In these cases, a hairpin grew out of the open end of the pocket, its legs stretched and a pair of streamwise streaks formed alongside the hairpin legs. The streaks grew to several hundred wall units. This observation is in contrast to the suggestions of a number of investigators that a lifted hairpin vortex would induce a single streak to form between its legs.

### 5.2 Slow rings ( $U_r/U_w < 0.35$ ) moving towards the wall at a shallow angle

These initial conditions result in a pair of long low speed streaks,  $x^+ = O(1,000)$ , a pocket, and hairpins which induce themselves and portions of the streaks to lift-up.

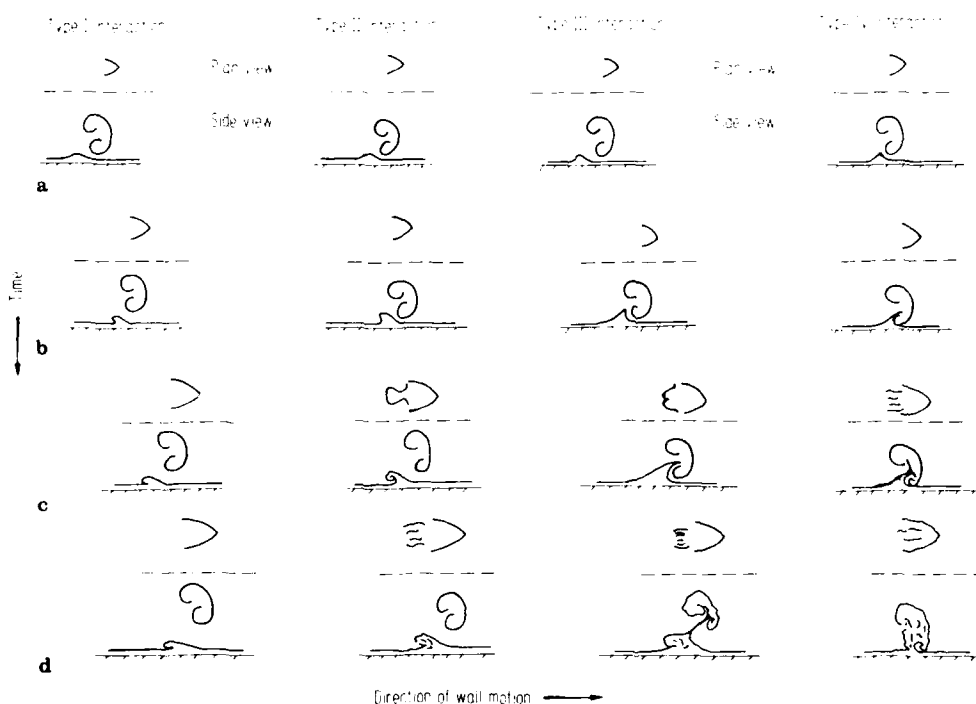
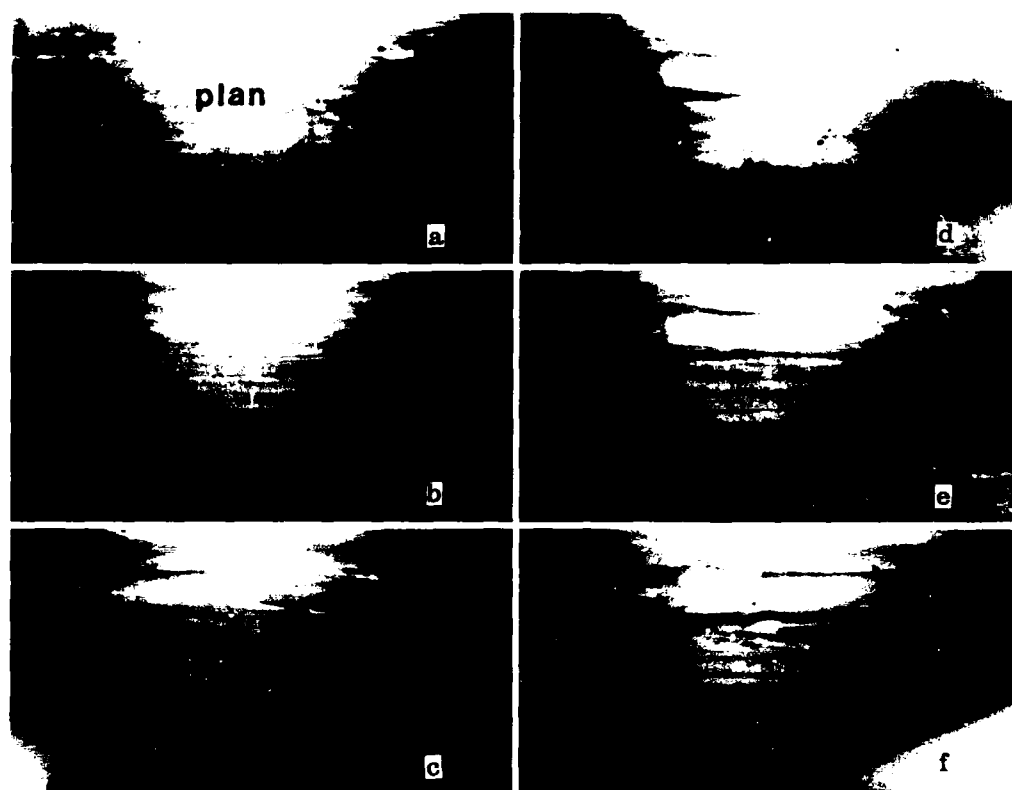


Fig. 4a-d. Sketches of the four types of local vortex ring/moving interactions (see text for explanation)



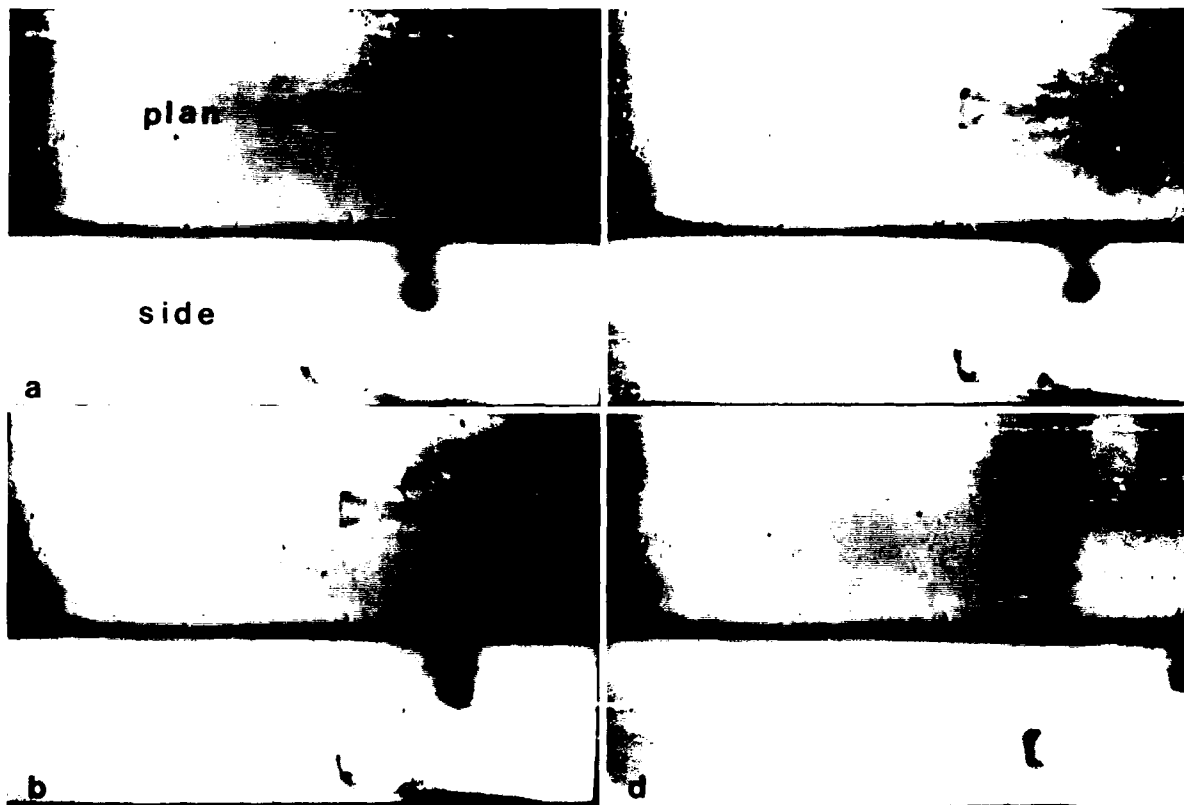
**Fig. 5a–f.** Six photos of a vortex ring/moving wall interaction for  $U_r/U_w < 0.35$  when the ring moves toward the wall at a  $3^\circ$  angle. Both plan and side views are shown, the ring and the wall are moving to the right, only the wallward side of the ring has dye in it. The interaction results in a pair of long streaks prior to the onset of a pocket and its associated hairpin lift-up, which then gets partially ingested into the ring

Figure 5 shows six photos of this happening prior to the onset of a Type III interaction. We can see the formation of the pair of low speed streaks, followed by the formation of the pocket, and the associated hairpin lift-up, then partial ingestion of the pocket hairpin. The ring later breaks up. The streaks that form under these conditions become wavy and slowly breakdown resulting in additional lift-up and transport. Hairpins have been observed to form over these streaks. The initial conditions are two-dimensional. The moving belt is started from rest, so that the layer approximates a Stokes' layer. These streaks have obviously not formed as the result of the pre-existence of streamwise vortices, but spanwise vorticity has been distorted to give a streamwise component, and it is clear from the Navier Stokes equations that new streamwise vorticity has also been generated at the wall.

### 5.3 Fast rings ( $U_r/U_w > 0.45$ ) moving away from the wall at a shallow angle (less than $3^\circ$ )

These initial conditions result in a hairpin vortex which is linked to the distributed streamwise vorticity that has

formed a pair of long, very stable, low speed streaks. A pocket is not observed. The evolution of the hairpin in this case has been observed to lead to the pinch-off of this hairpin, forming a vortex ring, and another hairpin. Figure 6 shows four photos of the evolution leading to the creation of a new vortex ring. The long stable streaks which form come closer and closer together, indicating that the streamwise vorticity which caused them, and which is of opposite sign, is being stretched and brought very close together. Diffusion is accelerated, and the vorticity is redistributed into a vortex ring and a hairpin loop. Figure 7 shows long, very stable streaks and a long stretched hairpin which does not pinch-off over the distance available due to size limitations of the experimental facility – more than 2500 wall layer units. There are two initial conditions that may cause this kind of long stretched streamwise vorticity to evolve into a hairpin: (1)  $\delta/D$  is very small; (2) the ring is far away from the wall. Further study concerning the effects of ring to wall distance is needed.



**Fig. 6a–d.** Four photos of a vortex/ring moving wall interaction for  $U_r/U_w > 0.45$  when the ring is moving away from the wall at a  $2.5^\circ$  angle: Both plan and side views are shown, the ring is at the upper right of the side view; ring and wall are moving to the right. A hairpin forms when the interaction starts; the long stable streamwise streaks which also form, come closer and closer together, indicating that the streamwise vorticity which caused them, and which is of opposite sign, is being stretched and coming closer together, this evolution leads to 'pinch-off' and the creation of a new vortex ring



**Fig. 7a and b.** Same conditions as Fig. 6, except that the wall layer is very thin, so  $\delta/D$  is small: We obtain long very stable streaks and a long stretched hairpin which does not pinch-off over the 2,500 wall layer distance of the facility; the time between each photo is approximately 50 wall units

#### 5.4 Slow rings ( $U_r/U_w < 0.45$ ) moving away from the wall at a shallow angle

These initial conditions result in a hairpin from which a pair of long, stable, low speed streaks emerge. A pocket is also not observed. The phenomena of hairpin 'pinch-off' for this case, appears to depend upon  $\delta/D$ . If  $\delta/D < 0.15$  we get pinch-off, but only a part of the fluid involved in the hairpin is observed to pinch-off and form the ring. If  $\delta/D$  is greater, and the ring moves away from the wall without ingesting any wall layer fluid (Type I or II), the lifted hairpin appears to do very little. Figure 8 shows four photos of the evolution for  $\delta/D > 0.15$ . In this case a pocket does not form, and it appears that the hairpin has been generated by the initial vortex ring/wall interaction, and that a pair of streamwise vortices – which could be called its legs – trail behind, creating the streak pair. Pinch-off does not occur. Figure 9 shows four photos of the interaction for  $\delta/D < 0.15$ . In this case pinch-off of a

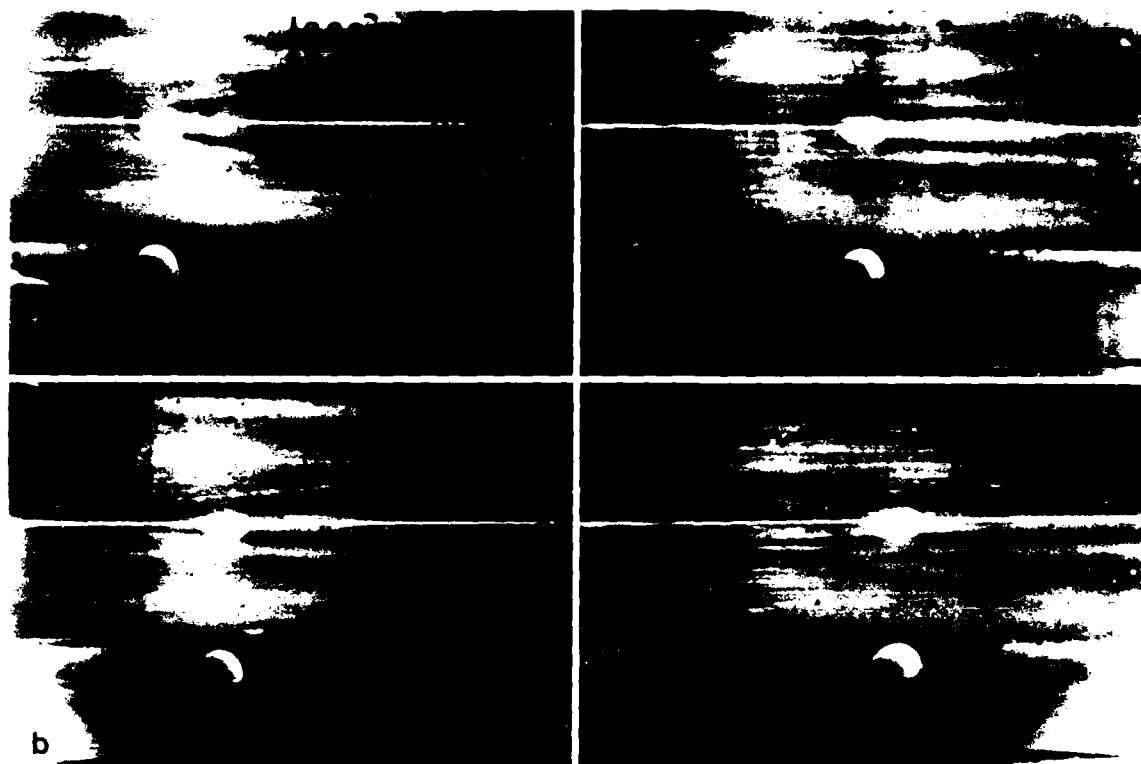


**Fig. 8a-d.** Four photos of a vortex/ring moving wall interaction for  $U_r/U_w < 0.45$  when the ring is moving away from the wall at a  $2.5^\circ$  angle and  $\delta/D > 0.15$ . Both plan and side views are shown; the ring has most of its dye in the upper part, ring and wall are moving to the right. Again a pair of long stable streaks is created, a pocket does not form, and a weak hairpin which forms does not pinch-off; there is evidence of a second pair of streaks forming

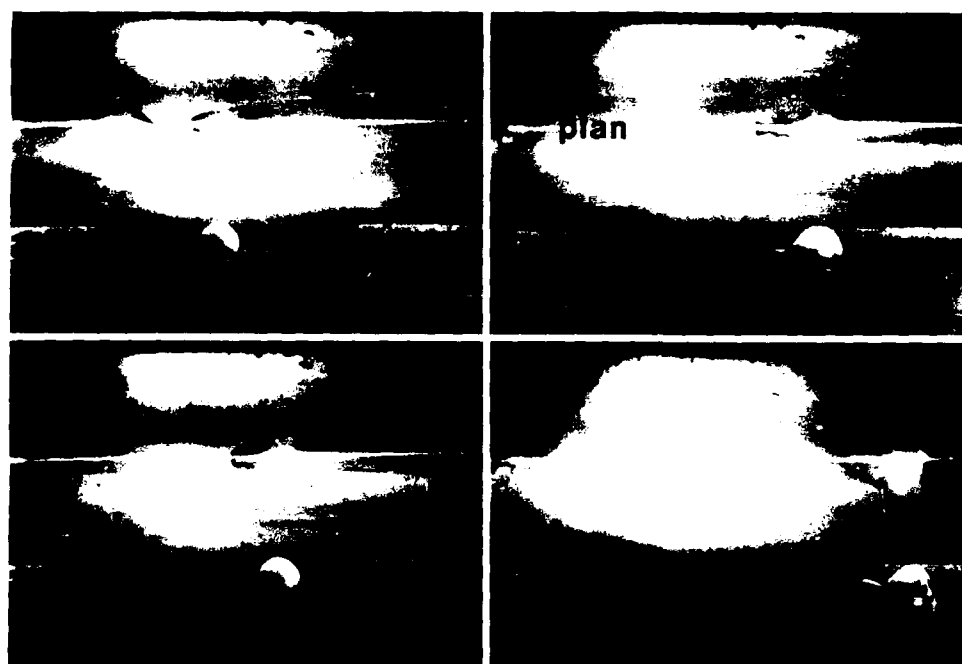


**Fig. 9a-d.** Same conditions as Fig. 8, except that  $\delta/D < 0.15$ ; in this case we again obtain a pair of long stable streaks and a hairpin. Pinch-off of a portion of the lifted hairpin does occur creating a new small vortex ring; We don't have the secondary streak pair forming

portion of the lifted hairpin does occur, creating a new small vortex ring.

### 5.5. Summary of interactions

We have found that for rings moving towards the wall at  $3^\circ$ , the formation was not a function of  $\delta/D$ , for  $D^+ > 250$ . The form taken was a function of  $U_r/U_w$ ; long streaks and pockets formed for  $U_r/U_w < 0.35$ , short streaks and pockets when  $0.35 < U_r/U_w < 0.45$ , and only pockets for higher speed ratios. For rings moving away from the wall at  $2.5^\circ$ , long streaks are generated over the entire speed ratio range studied, and  $\delta/D$  now plays an important role. When  $U_r/U_w < 0.55$ , if  $\delta/D$  is less than 0.15 we get long streaks and pinch-off of a small hairpin. For  $\delta/D > 0.15$ , we don't get pinch-off. In the range  $0.55 < U_r/U_w < 1$ , if  $\delta/D > 0.05$  we get long streaks and hairpin pinch-off, for smaller values of  $\delta/D$  we have a long stretched hairpin and pinch-off is not observed.

### 5.6. Scaling associated with the vortex ring moving wall interactions

From our perspective of a turbulence production model, the streak spacing, streak length and wavelength of the streak instability are quantities of interest.

The dependence of the streak spacing in wall units on the size of the vortex ring in wall units, for an incidence angle of  $3^\circ$  and  $U_r/U_w = 0.31$ , is shown in Fig. 10. The thickness of the wall layer (in wall units) is shown next to each data point. The streak spacing,  $Z^+$ , is within 10% of the ring diameter for wall layer thicknesses between 20 and 50 wall units. Results show that decreasing  $U_r/U_w$  will decrease the average streak spacing relative to the ring size for fixed incidence angles. Furthermore, increasing the incidence angle of the vortex ring will increase the average streak spacing for a given ring size and speed ratio. Figure 11 shows the dependence of the streak spacing on the speed ratio and angle.

Measurements show that streak lengths greater than  $x^+ \approx 500$  were obtained for many of the interactions in ranges where the streaks are stable (for rings with  $D^+ = 100$ , streaks as long as  $x^+ = 1,000$  were found).

Figure 12 shows the non-dimensionalized streamwise wavelength that sets in as a function of  $\delta^+$  for different  $U_r/U_w$ . The wavelength is the same order as the ring diameter. It decreases as the ring/wall speed ratio.

### 5.7. Stability considerations

Some additional data has been obtained, which confirms and extends the results of Liang (1984), showing that the boundary between stable ring wall interactions (Types I and II), and unstable interactions (Types III and IV)

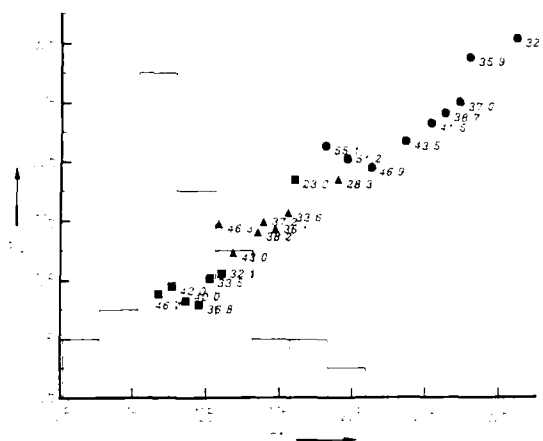


Fig. 10. The distribution of  $D^+$  obtained from the diameter of the Typical eddies of a turbulent boundary layer at  $R_\tau = 1,176$ , superimposed upon the streak spacing obtained for various size rings, for an incidence angle of  $3^\circ$  and  $U_r/U_w = 0.31$ ; the thickness of the wall layer (in wall units) is shown next to each data point

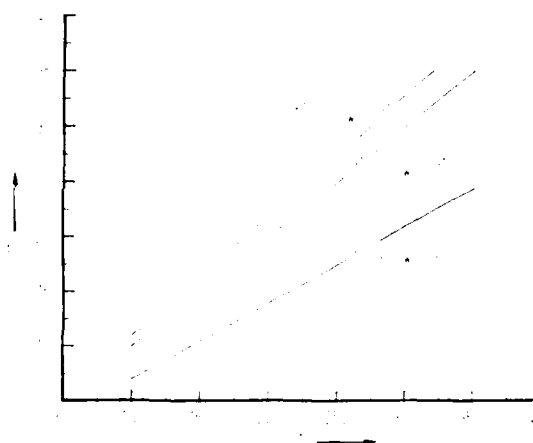


Fig. 11. The dependence of the streak spacing on the speed ratio and ring interaction angle

depends upon  $\delta/D$ . Figure 13 shows a stability map of the interactions for  $3^\circ$  rings. We can see that for low ring/wall speed ratios, the ring stability depends primarily upon the relative thickness of the wall layer and the size of the ring; for thicker wall layers or smaller rings, the interactions are more stable. Furthermore, the shallower the incidence angle, the more stable the interaction.

Figure 14 shows the dependence of the time to instability of the streaks which exhibited wavy instability on the wall layer thickness (both quantities non-dimensionalized by wall layer variables) for  $3^\circ$  incidence rings. We can see that for each convection velocity ratio, there is a value of  $\delta^+$  above which the time to instability becomes much longer. As the ring/wall speed ratio increases, the critical

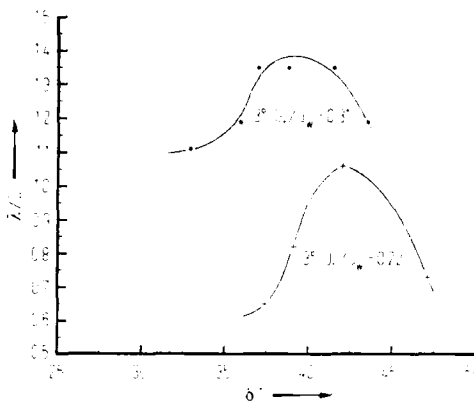


Fig. 12. The non-dimensionalized streamwise wavelength of streaks subjected to wavy instabilities

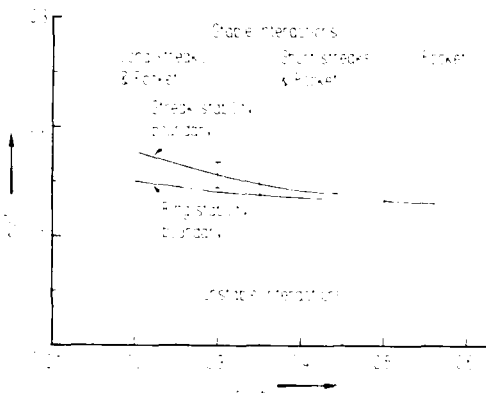


Fig. 13. Comparison of the 'stability boundaries' of a three degree ring moving towards the wall, and of the stability boundaries of the streaks those same rings create: the ring stability boundaries and the streak stability boundaries for different size rings collapse when plotted this way

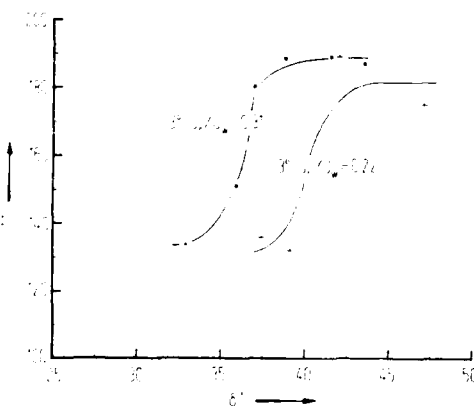


Fig. 14. The dependence of the time to instability of the streaks on the wall layer thickness (both quantities non-dimensionalized by wall layer variables) for 3° incidence rings

thickness of the wall layer needed to increase the time to instability decreases.

Both the rings and the streaks are more stable when the wall layer is thicker. Figure 13 shows a comparison of the stability boundaries of a three degree ring moving towards the wall, with the stability boundary of streaks formed by those same rings. The streak stability boundary has generally the same shape: stable rings will, in general, correspond to stable streaks, except for a small range of  $\delta/D$ . The ring stability curves and the streak stability boundary curves for different size rings collapse when plotted this way.

The streak stability boundary represents the boundary between conditions that will enable a pair of long streaks to form. For  $\delta/D$  below the boundary, we have a very unstable situation in which the fluid in the region around the eddy seems to rearrange itself into the beginnings of a streak, but the streak is not stable, and immediately breaks up. For  $\delta/D$  values above the boundaries, a pair of long streamwise streaks form. However, once formed, the streaks are susceptible to breakdown as noted above, where the time to instability is a function of angle, convection velocity, and the instantaneous wall layer thickness (for example, Fig. 14).

## 6 Implications for turbulent boundary layers

By performing a Galilean transformation on the simulation, we recover the essential aspects of the Typical eddy wall region interaction in a turbulent boundary layer flow. The wide range of interactions that can be simulated using the vortex ring/moving wall experiments are not all admitted by the turbulent boundary layer with equal frequency. Some are not admitted at all. The range of the parameters (angle, wall layer thickness, convection velocity) found in the boundary layer are limited, and in all cases they have skewed probability distributions (towards higher values) that are approximately lognormal. When these distributions are used to determine the events that are most probable, we begin to see what to expect.

The distribution of  $D^+$  obtained from the diameter of the Typical eddies of a turbulent boundary layer at  $R_\theta = 1.176$  is also shown in Fig. 10, superimposed upon the streak spacing obtained for various size rings. When the simulation outcomes are conditioned by the probabilities of scales found in this boundary layer, we see that the simulation gives a most likely streak spacing of approximately 100 wall units. This is an important quantitative test of the quality of the simulation, for although the average streak spacing is  $\lambda^+ \approx 100$ , all observations of streak pairs have also shown their spacing to be approximately this value.

### 6.1 Implications for drag modifications

As we have seen, small changes in the parameters of Typical eddy size, incidence angle, convection velocity, and wall layer thickness can alter the evolutions that result when a Typical eddy interacts with the wall. Changes in any of these variables which cause a crossover in the stability boundaries will result in a change in the drag at the wall.

Consider, for example, the angle of incidence. If we can change the strength of the large scale motions, say, by outer layer manipulators, we can easily change the angle of a Typical eddy that is moving towards – or away from – the wall, and may even be able to change the direction. This will affect the stability of both the local eddy wall interaction (interactions of Type I–IV), and the stability of the streaky structure which is created, as well as the formation of new Typical eddies via the pinch-off process. Thus, we can affect not only the local drag, but alter the drag downstream by directly interfering with the cyclic production process.

Modifications to the wall that result in small changes in the effective wall region thickness, for example, NASA riblets, will also have an effect on the drag. If increases in wall region thickness above the critical thickness can be made (for example, Fig. 13), streaks are more likely to remain stable. Furthermore, the local interactions (Types I–IV) will also tend to be of Type I and II. Thus, the drag can also be reduced.

### 7 Conclusions

New findings in the turbulent boundary layer have suggested that long, low speed streaks are formed in pairs as the result of the interactions of microscale very coherent vortex ring-like eddies (Typical eddies) propagating over the wall.

The vortex ring/moving wall simulation of the turbulence production process was shown to incorporate all of the evolutions, interactions, and structural features. It dramatically demonstrates that streamwise vortices are not required to produce streamwise streaks. When the streak spacings obtained in the simulation are conditioned by the probability of occurrence of Typical eddy scales found in the boundary layer, we see that the simulation provides the correct streak spacing (approximately 100 wall units). Other possible outcomes of the simulation need to be weighed by the measured probabilities of occurrence of the angles, convection velocities, and length scales of the Typical eddies in the turbulent boundary layer to enable us to obtain a picture of the most probable forms of the interactions, and to gain insight into the causes of the interactions which occur with lower probability, that may contribute significantly to the transport. It appears that turbulent boundary layer control leading to drag reduction can be realized by fostering the conditions suggested by

the simulations which will increase the probability of having stable interactions.

### Acknowledgements

This research was sponsored by the Air Force Office of Scientific Research under Contract No. F49620-85-C-0002. We would like to thank Dr. J. McMichael for his encouragement and advice as contract monitor.

### References

- Acarlar, M. S.; Smith C. R. 1984: An experimental study of hair-pin-type vortices as a potential flow structure of turbulent boundary layers. Rept. FM-5, Dept. of M.E./Mech., Lehigh Univ.
- Falco, R. E. 1974: Some comments on turbulent boundary layer structure inferred from the movements of a passive contaminant. AIAA Pap. 74-99
- Falco, R. E. 1977: Coherent motions in the outer region of turbulent boundary layers. *Phys. Fluids* 20, S124–S132 (Suppl. II)
- Falco, R. E. 1980a: The production of turbulence near a wall. AIAA Pap. No. 80-1356
- Falco, R. E. 1980b: Structural aspects of turbulence in boundary layer flows. In: *Turbulence in liquids* (ed. Patterson, G. K.; Zakin, J. L., pp. 1–15, Dept of Chemical Engineering, Univ. of Missouri-Rolla
- Falco, R. E. 1980c: Combined simultaneous flow visualization/hot-wire anemometry for the study of turbulent flows. *J. Fluids Eng.* 102, 174–183
- Falco, R. E. 1982: A synthesis and model of wall region turbulence structure. In: *The structure of turbulence, heat and mass transfer* (ed. Zoric, Z.), pp. 124–135. Washington: Hemisphere
- Falco, R. E. 1983: New results, a review and synthesis of the mechanism of turbulence production in boundary layers and its modification. AIAA Pap. No. 83-0377
- Head, M. R.; Bandyopadhyay, P. 1981: New aspects of turbulent boundary layer structure. *J. Fluid Mech.* 107, 297–337
- Kim, J. 1986: Investigation of turbulent shear flows by numerical simulation. Tenth Congress of Applied Mechanics, Austin TX, June 16–20
- Liang, S. 1984: Experimental investigation of vortex ring/moving wall interactions. MS thesis, Dept. Mech. Eng. Michigan State Univ.
- Liang, S.; Falco, R. E.; Bartholomew, R. W. 1983: Vortex ring/moving wall interactions: experiments and numerical modeling. *Bull. Am. Phys. Soc. Ser. II*, 28, 1397
- Moin, P.; Leonard, A.; Kim, J. 1986: Evolution of a curved vortex filament into a vortex ring. *Phys. Fluids* 29, 955–963
- Oldaker, D. K.; Tiederman, W. G. 1977: Spatial structure of the viscous sublayer in drag reducing channel flow. *Phys. Fluids* 20, 133–144
- Praturi, A. K.; Brodkey, R. S. 1978: A stereoscopic visual study of coherent structures in turbulent shear flow. *J. Fluid Mech.* 89, 251–278
- Runstadler, P. W.; Kline, S. J.; Reynolds, W. C. 1963: An experimental investigation of the flow structure of the turbulent boundary layer. Dept. of Mech. Eng. Rep. MD-8, Stanford Univ.
- Smith, C. R. 1982: Application of high speed videography for study of complex, three-dimensional water flows. *SPIE* 348, *High Speed Photography* (San Diego), pp. 345–352
- Smith C. R.; Metzler, S. P. 1983: The characteristics of low-speed streaks in the near-wall region of a turbulent boundary layer. *J. Fluid Mech.* 129, 27

Received September 8, 1987



# Rayleigh-Benard convection: experimental study of time-dependent instabilities\*

B. Martinet and R. J. Adrian

Dept. of Theoretical and Applied Mechanics, University of Illinois, Urbana, IL 61801, USA

**Abstract.** The transition from steady thermal convection to turbulent thermal convection in a horizontal layer of water (Prandtl number = 5.8) contained by a square cavity of large aspect ratio (48.5) has been studied using laser Doppler velocimetry. Power spectra of the horizontal velocity fluctuations were measured in the Rayleigh number range from 30,000 and 99,000, wherein periodic, quasi-periodic, and broad-band time-dependent instabilities coexist. At Rayleigh numbers greater than 32,000 a narrow-band spectrum emerges. The frequency of this motion scales with  $\alpha d^2$  modified by a Prandtl number factor for intermediate values of the Prandtl number. Between  $10 Ra_c$  and  $30 Ra_c$  the frequency undergoes three abrupt jumps while increasing along an  $Ra^{2/3}$  power law. A different frequency mode that occurs above  $30 Ra_c$  appears to be associated with fully turbulent convection.

## List of symbols

$c$	heat capacity
$d$	depth of fluid layer
$f$	frequency
$g$	gravitational acceleration
$H$	heat flux
$k$	thermal conductivity
$Nu$	Nusselt number = $Hd/k\Delta T$
$Pr$	Prandtl number = $\nu/\alpha$
$Ra$	Rayleigh number
$Ra_c$	critical Rayleigh number = 1708
$\Delta T$	temperature difference across the fluid layer
$\beta$	thermal coefficient of expansion
$l$	aspect ratio = width/depth
$\alpha$	thermometric conductivity = $k/\rho c$
$\nu$	kinematic viscosity
$\rho$	density

## 1 Introduction

Horizontal fluid layers heated from below become unstable to infinitesimal perturbations at a critical Rayleigh number  $Ra_c = 1708$ . They subsequently undergo a sequence of instabilities as the Rayleigh number is increased, and at Rayleigh

number around  $10^5$  they become generally chaotic, with smooth, broad-band spectra having no discernible peaks. At sufficiently large Rayleigh numbers, perhaps as large as  $10^7$  or  $10^8$ , the buoyancy-driven motions become fully turbulent.

The succession of instabilities has been investigated extensively using linear and non-linear stability analysis and flow visualization. Steady instabilities that have been identified include the basic infinitesimal amplitude roll cells (Chandrasekhar 1961, Busse 1978) finite amplitude roll cells, and hexagonal Benard cells (Busse 1967), the zig-zag instability of roll cells (Busse and Whitehead 1971), the cross-roll instability (Busse 1971), and the skewed varicose and knot instabilities (Busse and Clever 1979). Time-dependent instabilities include the fundamental three-dimensional oscillatory motion of roll cells (Willis and Deardorff 1970, Busse 1972), time-dependent bimodal convection (Busse and Whitehead 1974), the time-dependent knot or collective instability (Busse and Whitehead 1974, Clever and Busse 1979), and the transient skewed varicose instability (Clever and Busse 1979). At high Rayleigh numbers a "spoke" convection pattern has also been identified (Clever and Busse 1979), and at moderate Prandtl number Bolton et al. (1986) have identified oscillatory blob instabilities similar to those seen by Krishnamurti (1970). Many of these mechanisms are reviewed by Busse (1978).

The existence of one or more of these instabilities in a given convection system depends in a complicated, and sometimes sensitive, manner upon the Rayleigh number, the Prandtl number, the initial conditions of the experiment (including hysteresis effects), and the boundary conditions, including geometry of the necessarily finite convection cavity and the thermal properties of the cavity walls (Riahi 1984, Busse and Riahi 1980). The parametric map of all these effects is far from being fully developed.

Time-dependent instabilities have been studied experimentally for various Prandtl numbers and aspect ratios by Chen and Whitehead (1968), Willis and Deardorff (1970), Krishnamurti (1970, 1973), Busse and Whitehead (1974), Gollub, Hulbert, Dolny and Swinney (1977), Ahlers and Behringer (1979), Gollub and Benson (1980), Gollub,

\* A version of this paper was presented at the Tenth Symposium of Turbulence, University of Missouri-Rolla, September 22–24, 1986

# MEASUREMENT OF TWO-DIMENSIONAL FLUID DYNAMIC QUANTITIES USING A PHOTOCROMIC GRID TRACING TECHNIQUE

R. E. Falco and C. C. Chu

Turbulence Structure Laboratory, Department of Mechanical Engineering, Michigan State University

## ABSTRACT

A non-intrusive photochemical phenomena called photochromism is used to obtain important fluid quantities such as velocity, and vorticity over a two-dimensional domain of a fluid flow. Using a uv laser, and a novel beam splitting and steering technique, a grid of lines is impressed in the prepared fluid. Two successive pictures are needed to calculate the fluid dynamic quantities. Measurements in a Stokes' layer are compared against exact solutions, and measurement of the circulation of a vortex ring is presented. The technique will be useful in turbulent and unsteady flows.

## 1. INTRODUCTION

There is an increasing need to obtain flow field information over a region of flow simultaneously. Examples include the study of mixing in internal combustion engines, and the understanding of the importance of coherent motions in many turbulent and unsteady flows. Furthermore, there is a need to obtain more detailed information about these and many simpler flows, including vorticity and strain-rate measurements. Existing probe techniques are at best able to provide single point estimates of these quantities in flows with steady mean velocities.

Hummel and his co-workers first exploited the phenomena of photochromism<sup>1,2</sup>. Using a single line of uv radiation for excitation, he and his co-workers were able to measure one component of velocity in flows with predominately one direction of motion. With the advent of high power uv lasers and new chemicals it is increasingly possible to apply the technique to more complicated flows. We have generalized the technique to enable it to uniquely tag specific points in the flow on a specified grid. As a result we have a non-intrusive photo-optical technique which can be used to obtain two velocity components and the spatial gradients of these components, at a large number of points in a flow field.

## 2. USE OF PHOTOCROMISM TO MEASURE FLUID DYNAMIC QUANTITIES

The phenomena of photochromism has been defined by Brown<sup>3</sup> as "a reversible change of a single chemical species between two states having distinguishably different absorption spectra, such change being induced in at least one direction by the action of electromagnetic radiation." The chemical used in this study was Kodak 1,3-Trimethyl-8-nitrospiro[2-H-1-benzopyran-2,2'-indoline]. We excited it at 351nm using pulses of 20ns produced by a Tachisto Excimer laser running on XeF (approximately 100mj output). Dissolved in the working fluid, which was kerosene, we found that the chemical, thus excited, reflected blue light for the order of tens of seconds. Thus, the fluid was tagged long enough for it to move appreciably. In practice, for the velocities of our experiments, we needed to follow the lines only a fraction of a second to obtain the information required.

## 2.1 Use of a grid to tag fluid particles

To enable us to measure two components of the velocity in a flow using the visualization, we must tag and follow specific fluid particles. The simplest way to do this is have two lines intersect. That intersection defines a point in the flow which, because it is colored, we can follow. To measure a spatial gradient, we must simultaneously mark two points in the flow. To enable us to measure a spatial gradient in a prescribed direction, we need several points and must use interpolation. Thus, creation of a grid of intersecting marked fluid lines would enable both velocities and gradients to be measured.

## 2.2 The beam divider

We sought a method of dividing a beam of laser light into 'n' beams where 'n' would be 5-25, using a static device. In doing so, we sought to lose as little light as possible. Thus, we designed a divider that appears as an oversized blazed reflection grating; the steps size 'a' is approximately 2mm. The incident laser energy was directed at a shallow angle to the plane of the grating. Because the facets are so much larger than a wavelength of light, we expected to primarily see specular reflection. The separation of the specularly reflected portions of the beam were determined by the difference of the angle of incidence and the blaze angle, and the grating step width and spacing as shown in Fig. 1. A photo of the actual beam divider is shown in Fig. 2. It was fabricated by individually fixing Aluminum coated mirrors (with the coating optimized for shallow incidence angles) to a machined base. Apart from diffraction effects, no incidence laser energy would be lost.

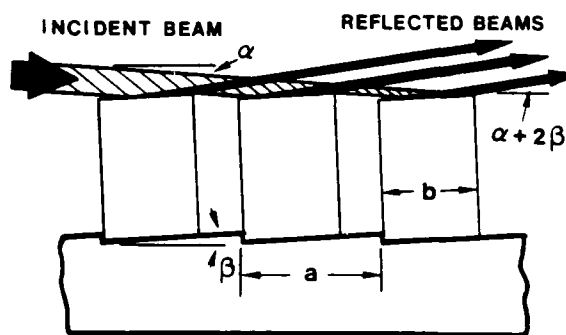


Fig. 1. The specular reflection from the beam divider.

As expected, however, diffraction effects were exhibited. A photo of the output of the beam divider using a Helium Neon laser is shown in Fig. 3. We see the specularly reflected beams, and the superimposed diffraction pattern. The diffraction bands are spaced as expected from the grating equation<sup>4</sup>. The appearance of the first and higher order bands are a source of 'noise' in the present grid making scheme. When experiments were performed with the Excimer laser at

351 nm, the diffraction pattern was, for reasons we do not understand, not observed. If it was present, results showed that it was too weak to excite the photochromic chemical (see Fig. 5a and 5b).



Fig. 2. The beam divider



Fig. 3. A photo of the output of the beam divider.

Fig. 4 shows a sketch of the optical set-up for making the grid shown in Fig. 5a. Note that the lines in Fig. 5a remain uniform and show little divergence. The mesh size is the order of 1mm. The two photos in Fig. 5 are 0.4 seconds apart, taken by a still camera with a motor drive. From the distortion of the grid in Fig. 5b with respect to that in Fig. 5a, (one laser pulse, two photos  $\Delta t$  apart) we can calculate all the kinematic quantities of the flow in the plane of the film. (Note, that in practice we would not use a second image which has distorted as much as Fig. 5b, but we present it to illustrate the ideas involved.)

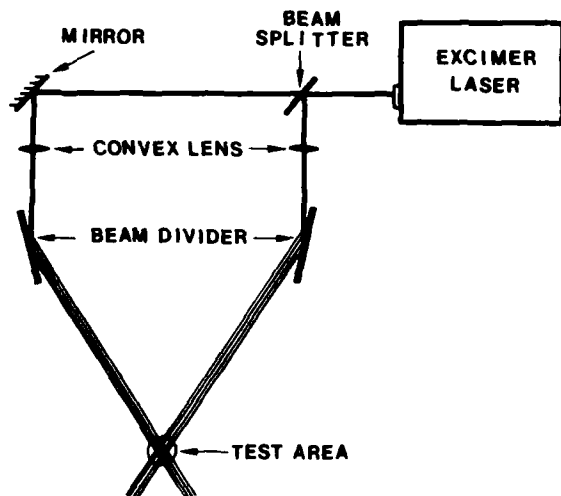
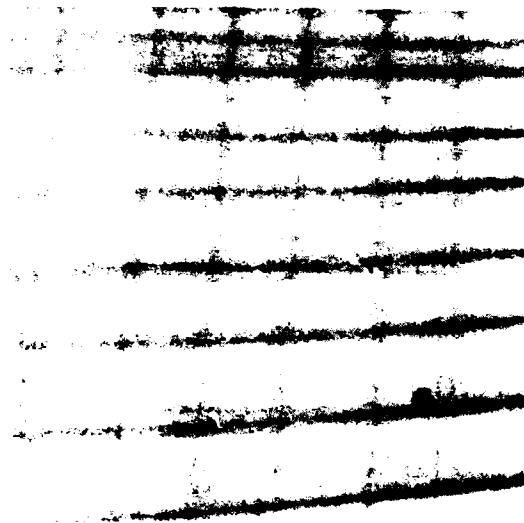
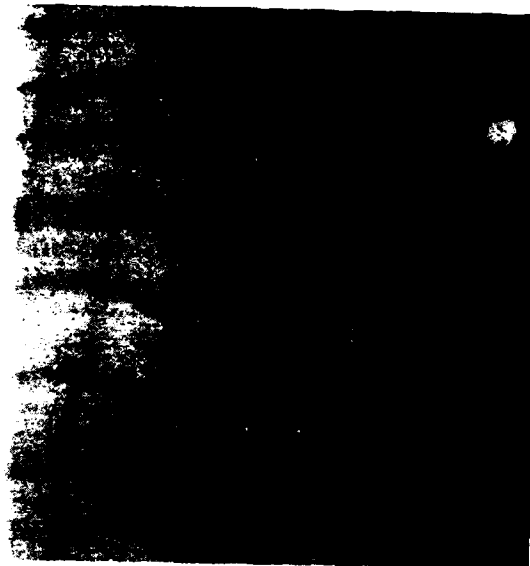


Fig. 4. The optical setup used to produce a grid of laser lines.



1 mm (a)



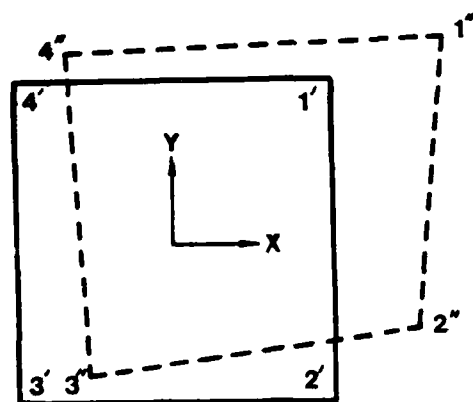
(b)

Fig. 5. An example of the grid. a) shortly after the laser pulse. b) .4sec later.

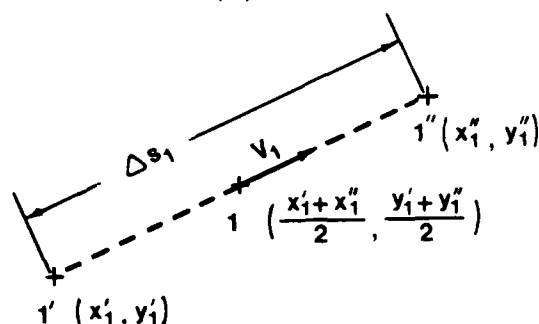
### 2.3 Algorithms to obtain fluid dynamic quantities

For convenience, we pick up one 'grid box' in Fig. 5a which, if the mesh size is small enough, can be thought of as a text book fluid 'particle' in flow at time  $t = 0$ . This fluid particle is shown using solid lines in Fig. 6a. As this particle moves with the flow, it may undergo several motions such as translation, rotation and deformation. The dashed lines in Fig. 6b show the same fluid particle after a short time interval,  $\Delta t$ . Because we know the history of this specific fluid particle, we can compute the velocity of each corner by taking the time derivative of displacement  $ds$  associated with each point, that is,  $ds/\Delta t$ . The deduction procedures are shown in Fig. 6b.

Note that  $V$  is designated as the velocity at point 1 which is then positioned at the midpoint between point  $1'$  and point  $1''$ . Fig. 7 shows the velocity vectors deduced from Fig. 6. Actually, a fluid particle moving in a general three-dimensional flow field may have motions about all three coordinate axes, however, we limit the discussion to the projection of this motion onto the plane of the photos which is parallel to the initial plane of the grid.



(a)



(b)

Fig. 6. Procedure for conversion of the displacement of a grid box to velocities.

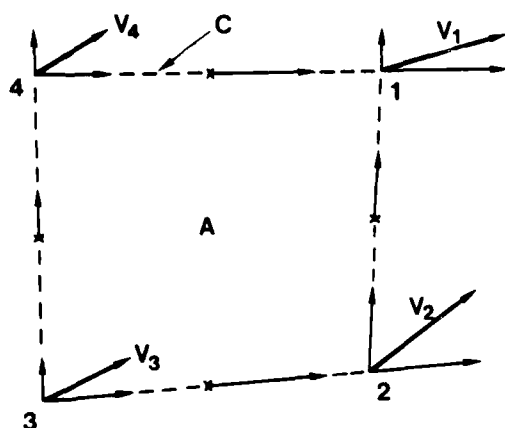


Fig. 7. Decomposition of the velocities used to calculate the circulation around a grid box.

To obtain velocity gradients, vorticity, and strain rates from the velocities, we must difference across the distance of a grid box. Thus, for a given flow the grid must be small enough to resolve the smallest scales of motion.

An alternative method can be used if we are only interested in the vorticity. Using the definition of the circulation  $\Gamma$ ,

$$\Gamma = \oint_C \mathbf{V} \cdot d\mathbf{s} \quad (1)$$

and Gauss' theorem to relate the surface integral to an area integral,

$$\Gamma = \int_A \omega \cdot \mathbf{n} dA$$

we can obtain the vorticity component normal to the film plane,  $\omega_z$ , from a grid box of arbitrary shape, with circumference  $C$  and area  $A$ .

The velocity component  $\mathbf{V} \cdot d\mathbf{s}$  in Eq. (1) is estimated by forming the average of the corner velocity components (see Fig. 7). Dividing  $\Gamma$  by the area of the fluid particle results in the average vorticity at the centroid of this fluid particle. This technique has the advantages of avoiding a second differencing of the experimental data.

Thus, by following the distortions of a single grid box we can obtain the velocities, circulation, vorticity and even the Reynolds stresses and strain rates if desired, over that small area. By doing this for the other grid mesh points, we can obtain the important fluid dynamic quantities at many locations over a two-dimensional field in a fluid flow simultaneously.

#### 2.4 Error analysis

Consider the grid box in Fig. 6. We will assume that the grid mesh is spaced  $\epsilon$  and that a worst case line movement between images is  $1/2$  the mesh width. After time  $\Delta t$  standard analysis<sup>9</sup> shows that the error in estimating the vorticity  $\omega_z$  is

$$\delta \omega_z = (1/\Delta t)(\delta \epsilon / \epsilon)$$

to first order in  $\epsilon$ .

As an example of the designed accuracy of our experiments, if we produce  $100\mu\text{m}$  lines on a grid mesh of  $1\text{mm}$ , and our error in reading the center of the lines is  $10\%$ , we obtain  $\delta \epsilon / \epsilon = .01$ . For  $\Delta t = .01\text{sec}$ , the error in the measurement of vorticity is  $1/\text{sec}$ . This is better than has been possible with hot-wire probes, and is comparable with the most sophisticated single point laser doppler measurements.

### 3. EXPERIMENTAL RESULTS

Two experiments were performed to demonstrate the technique. Both used deodorized kerosene with  $10\text{ ppm}$  of the photochromic chemical dissolved in it. The data were recorded on Kodak Tmax 400 ASA film through a Photo-Sonics  $35\text{mm}$  high speed movie camera, framing between  $150$  and  $200$  frames per second. The films were analyzed on a NEC film analyzer which is accurate to  $.05\text{mm}$ .

### 3.1 Stokes' layer flow

We can test the accuracy of the technique in a flow for which an exact solution of the Navier-Stokes equations is obtainable. The flow is that of an impulsively started infinite plate in an initially still infinite ambient. The problem involves the two-dimensional diffusion of vorticity generated at the plate into the ambient. The thickness of the boundary layer,  $\delta$ , is a function of the kinematic viscosity,  $\nu$ , and the time after the start of the plate's motion. We have approximated this motion using a belt in a tank which can be rapidly started. Fig. 8 shows the experimental setup. The width of the belt is 17.8 cm, and the distance between the rollers is 152.4 cm, with the test position 90 cm downstream of the lead roller. All experimental data was obtained before the leading edge effects reached the test position. Furthermore, the aspect ratio is sufficient to prevent the disturbances generated in the corners from reaching the center of the belt at the test section in the test time interval. Therefore, the wall layer flow measured was two-dimensional. The speed of the belt was adjustable from 2.5 to 22.9 cm/sec. It reaches a constant speed within a second. This short acceleration reasonably approximates an impulsive start. A grid mesh size of .156 was used, with the laser lines intersecting as in Fig. 8.

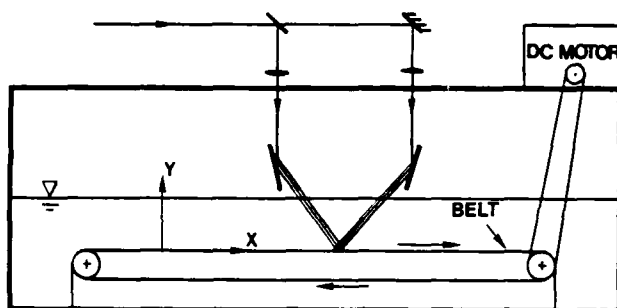


Fig. 8. Setup used to create and measure the Stokes' layer flow.

Results of the velocity gradient obtained from double differentiation in the Stokes layer are shown in Fig. 9, where they are compared with the exact solution. Everything is non-dimensionalized by the similarity variables of the exact solution. Because the flow is two-dimensional, incompressible, and doesn't change with the streamwise coordinate,  $x$ , the continuity equation reduces to  $\partial v / \partial y = 0$ , and a check on this is also shown in Fig. 9 ( $v$  is the velocity component normal to the wall, and  $y$  is the coordinate normal to the wall). We see that both the error in the estimates of the continuity equation, and in the velocity gradient distribution are of similar magnitude. The absolute value of the error is  $\pm 2/\text{sec}$ , consistent with the design error analysis. The deviation of the experimental profile in the near wall region is a consequence of the grid mesh being too large to adequately resolve the large value of the gradient  $\partial u / \partial y$ . On the whole the results are very encouraging.

### 3.2 Vortex ring flow

The real value of the technique is its ability to measure flows that are not measurable, analytically solvable or numerically calculable. The vortex ring is a common place example. It represents a class of flow fields that are of particular importance in turbulent and unsteady flows.

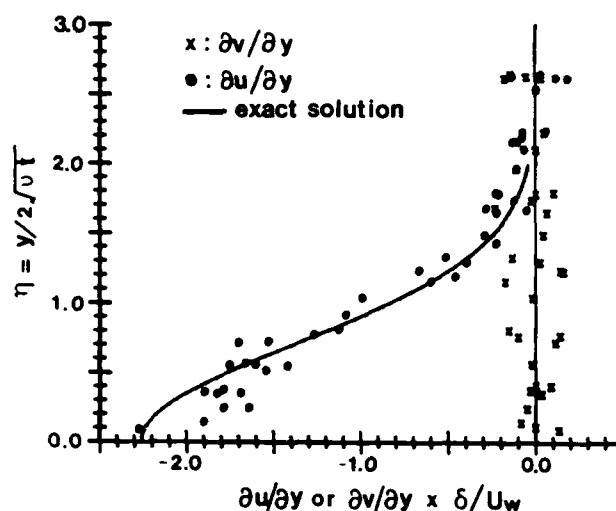


Fig. 9. Experimental measurements of the velocity gradient in a Stokes' layer compared with the theoretical solution. A check of the continuity equation  $\partial v / \partial y = 0$  is also shown.

The experimental setup used to generate the vortex ring is shown in Fig. 10. A small amount of fluid from a constant head reservoir was emitted from a 1.9 cm orifice to create the rings. A solenoid valve whose opening time could be adjusted controlled the outflow. The kerosene in the reservoir was dyed with chlorophyll to partially mark the ring. The convection velocity of the rings was measured to be 3.8 cm/sec at the test section which is located 7.6 cm downstream of the orifice. The Reynolds number of the ring is approximately 700, based on the ring's core diameter and its convection velocity. The flow is axisymmetric, so that we only needed to align our grid through an axis of symmetry and measure the flow in half of the ring to measure its circulation.

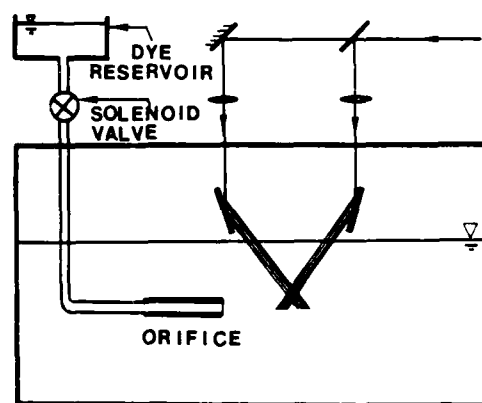


Fig. 10. Setup used to create and measure the circulation of a vortex ring.

The instantaneous circulation distribution of the ring is shown in Fig. 11. Although no solution exists for the experimentally created ring, we show a comparison with Hill's exact solution for a ring in which the vorticity occupies a sphere. The core of our ring is smaller than that of the hypothetical Hill's ring, the overall shape is an oblate spheroid, and it is unlikely that the vorticity distribution is similar, but, as the data shows, the circulation of the ring (Reynolds number = 700) is not very different.

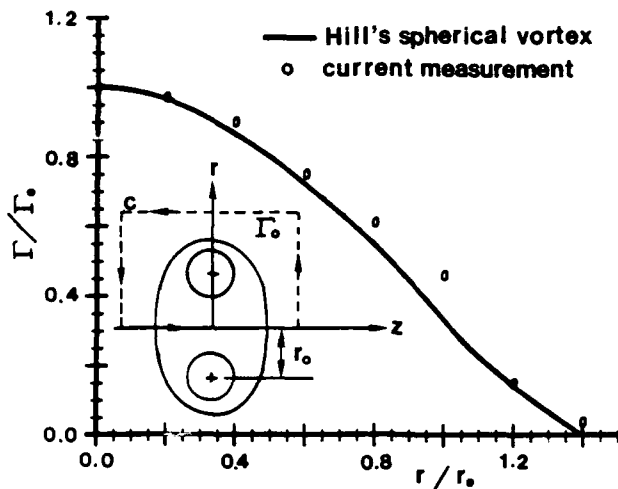


Fig. 11. The circulation distribution of a laminar vortex ring (Reynolds number = 700), compared with Hill's solution for a spherical vortex.

#### 4. DISCUSSION

The demonstrated accuracy of the technique is more than adequate for many fluid dynamic problems. Since, in principle, the calibration depends only on a time and a length scale, there is further room for improvement. In practice, determining the intersection points of the grid lines is limited by the grain size of the film used, and the distortion of the developing process. Improvements in the grain limitation can be made by using a large format still camera with a shuttering mechanism that will enable a double exposure of the grid to be made on a plate. Furthermore, image processing techniques can be used to increase the accuracy and repeatability of the results. We are currently pursuing these avenues.

The technique is not restricted to slowly varying flows as are so many flow visualization techniques. Furthermore it is not restricted to Newtonian fluids. We feel that the whole field approach can supplement LDA measurements where velocity fields are required, as well as going beyond to make Reynolds stress, vorticity, and strain rate measurements where needed.

Since the photochromic grid following technique requires only a single pulse of uv light to create the grid in a suitably mixed solution, the technique can be used in many labs which possess single pulse or low pulse rate lasers.

Current limitations include the need to work in organic liquids, required to dissolve the chemicals, and available penetration of the laser beam into the fluid. This problem, addressed in Ref. 2 is a function of both the laser power and the chemical concentration. It can be alleviated somewhat by scanning the laser beam across the 'steps' in the beam divider, thereby putting the full energy of the laser in every line. Since the excitation takes place in picoseconds, during a 20 nanosecond pulse width, the scanning (through minutes of a degree) can be accomplished with off the self equipment, and each line in the fluid will be proportionally more intense, or the chemical concentration reduced to enable laser penetration further into the fluid.

#### 5. CONCLUSIONS

A new technique for obtaining velocity, and velocity gradient data over a two-dimensional domain of a fluid flow is presented. Calibration depends only upon a time and a length scale. Comparison of measurements with the exact solution in a Stokes' flow indicates that its accuracy can be predicted by classical analysis, and is comparable or better than that achievable with the best single point probe techniques. The circulation of a vortex ring has been measured.

#### 6. ACKNOWLEDGMENTS

We greatly acknowledge support of the Air Force Office of Scientific Research under Grant No. AFOSR-87-0047. The contract monitor was Dr. Jim McMichael. We are also pleased to acknowledge the assistance of Mr. Sean Hilbert, especially for his role in the fabrication of the beam divider.

#### 7. REFERENCES

1. Popovich, A.T. and Hummel, R.L., A.I.Ch.E.J., Vol.14, pp. 21-25 (1967).
2. Seeley, L.E., Hummel, R.L. and Smith, J.W., J. Fluid Mech., Vol. 68, pp. 591-608 (1975).
3. Brown, G.H., ed., Photochromism, Wiley-Interscience, New York (1971).
4. Hecht, E. and Zajac, A. Optics, Addison-Wesley, pg 357 (1974).
5. Taylor, J.R. An Introduction to Error Analysis Univ. Sci. Books, Calif. (1982)
6. Lang, B.L. Laser Doppler Velocity and Vorticity Measurements in Turbulent Shear Layers, PhD Thesis GALCIT, Cal. Tech. (1985).
7. Hill, M.J.M. Phil. Trans. Roy. Soc. A Vol. 185 (1894).